Improving a Super Dual Auroral Radar Network Reflector Through Directivity Characterisation

by

Christopher Patrick Gray

Thesis presented in partial fulfilment of the requirements for the degree of Master of Engineering (Electrical and Electronic) in the Faculty of Engineering at Stellenbosch University

Supervisor: Dr. P.G. Wiid
Co-supervisor: Dr. M. Kosch

December 2019

Declaration

I have read and understand the Stellenbosch University Policy on Plagiarism and the definitions of plagiarism and self-plagiarism contained in the Policy [Plagiarism: The use of the ideas or material of others without acknowledgement, or the re-use of one's own previously evaluated or published material without acknowledgement or indication thereof (self-plagiarism or text-recycling)].

I also understand that direct translations are plagiarism, unless accompanied by an appropriate acknowledgement of the source. I also know that verbatim copy that has not been explicitly indicated as such, is plagiarism.

I know that plagiarism is a punishable offence and may be referred to the University's Central Disciplinary Committee (CDC) who has the authority to expel me for such an offence.

I know that plagiarism is harmful for the academic environment and that it has a negative impact on any profession.

Accordingly all quotations and contributions from any source whatsoever (including the internet) have been cited fully (acknowledged); further, all verbatim copies have been expressly indicated as such (e.g. through quotation marks) and the sources are cited fully.

I declare that, except where a source has been cited, the work contained in this assignment is my own work and that I have not previously (in its entirety or in part) submitted it for grading in this module/assignment or another module/assignment.

Signature	Date
Christopher Patrick Gray	

Abstract

Improving a Super Dual Auroral Radar Network Reflector Through Directivity Characterisation

C P. Gray

Department of Electrical and Electronic Engineering,
University of Stellenbosch,
Private Bag X1, Matieland 7602, South Africa.

Thesis: MEng (E&E)

December 2019

This thesis considers characterising the directivity of the Super Dual Auroral Radar Network (SuperDARN) radar, located at the South African National Antarctic Expedition Station (SANAE IV) base in Antarctica, to improve the currently installed 90° half corner reflector. A 1:100 scale model of limited array elements was designed, manufactured and measured in the anechoic chamber of the Electrical and Electronic Engineering Faculty at Stellenbosch University. These results were then compared to the same measurement set-up run in simulation with Altair Hyperworks FEKO EM solver software, determining that FEKO can provide sufficiently accurate results and that it could be used to characterise the full-scale SuperDARN radar. Through numerous simulation runs, the full-scale model of the currently installed SuperDARN radar with its 90° half corner wire reflector was successfully characterised. Various 90° half corner wire reflectors were then simulated with the aim to improve on the installed 90° half corner wire reflector. It was determined that, while the installed 90° half corner wire reflector does perform within its required operations, a 90° full corner wire reflector would suit the SuperDARN much better. A 90° full corner wire reflector would improve the front to back directivity ratio of the SuperDARN by 6.2 dB and a proposed 90° full corner wire reflector layout design is provided with a front to back ratio of 10.7 dB.

Uittreksel

Verbetering van 'n Super Duale Aurora Radar Netwerk Weerkaatser deur Direktiwiteit Karakterisering

("Improving a Super Dual Auroral Radar Network Reflector Through Directivity Characterisation")

C P. Gray

Departement Elektriese en Elektroniese Ingenieurswese,
Universiteit van Stellenbosch,
Privaatsak X1, Matieland 7602, Suid Afrika.

Tesis: MIng (E&E)

Desember 2019

Hierdie tesis handel oor die direktiwiteitskarakterisering van die Super Duale Aurora Radar Netwerk se antenna reeks, geleë aan die Suid-Afrikaanse Nasionale Antarktika Ekspedisie basis (SANAE IV) in Antarktika, met die doel om die huidige geïnstalleerde halwe 90 (degree) hoek-weerkaatser te verbeter. 'N Skaalmodel van 1:100 met beperkte skikkingselemente is ontwerp, vervaardig en gemeet in die anekoomkamer van die Fakulteit Elektriese en Elektroniese Ingenieurswese aan die Universiteit Stellenbosch. Hierdie resultate is daarna vergelyk met dieselfde meetopstelling in simulasie met Altair Hyperworks FEKO EM-oplossingsagteware, wat bepaal dat FEKO voldoende akkurate resultate kan lewer en dat dit gebruik kan word om die volskaalse SuperDARN-radar te karakteriseer. Deur middel van talle simulasie-lopies, is die volskaalse model van die tans geïnstalleerde SuperDARN-radar met sy 90° halwe draadreflektor suksesvol gekenmerk. Verskeie 90° halwe draadreflektore is daarna gesimuleer met die doel om die geïnstalleerde 90° halwe draadreflektor te verbeter. Daar is bepaal dat hoewel die geïnstalleerde 90 ° halwe draadreflektor wel binne sy vereiste operasies presteer, 'n 90° volledige draadreflektor die SuperDARN baie beter sou pas. 'N Volledige hoekdraadreflektor van 90° sal die voor- en

agterrigtingverhouding van die SuperDARN met 6,2 dB verbeter, en 'n voorgestelde ontwerp van 90° volledige draadreflektoruitleg word voorsien van 'n voorkant tot rugverhouding van 10,7 dB.

Acknowledgements

First and foremost I would like to express my gratitude to my mother and father. Without their continued support though-out not only this project but my entire University career, I would not have been able to acquire my undergraduate degree and pursue a Master's thesis. I will forever be in your debt for the opportunities you have given and provided me throughout my life.

Thank you to everyone at the University of Stellenbosch for their much needed and much appreciated help during this project. Dr. Gideon Wiid, my supervisor, your invaluable time, dedication and patience guided me to complete this project. To Wessel Croukamp and Anneke Bester, your vast range of knowledge and industry procedures ensured the building and measurements of my scale model were done with precision and efficiency, saving me valuable time thoughout my project. To Dr. Danie Ludick, for all the help you provided in getting my larger simulation models running in CHPC. to which, I would like to acknowledge the Centre for High Performance Computing (CHPC), South Africa, for providing computational resources to this research project.

I would also like to thank the staff at SANSA for, firstly, providing an exciting project to work on and, secondly, their willingness to provide any information I requested during this project. To Dr. Michael Kosch my co-supervisor, thank you for providing me with the opportunity to work on a global project like the SuperDARN and to have a glimpse into some of the work done at SANSA. To Jonathan Ward, I enjoyed our work doing RFI measurements and data processing for a solar spectrometer antenna at the SALT telescope, and those 10:00 am quality coffee breaks. I would also like to thank you both for the many educational visits, seminars, and talks in Hermanus I was able to attend.

Finally, I would like to thank my fellow colleagues, of E212, which I work with at Stellenbosch University. Jackline Koech, it was great to have a fellow learner in the same postgraduate program as I was. We were always able to help each other out with our respective work and saved each other many hours of Google searching and flipping through heavy textbooks. To Stanley Kuja and Temwani Phiri, you were both always willing to give some of your time to help with the use of the many software tools we used at the University.

Contents

List of Figures

List of Tables

Nomenclature

Constants

$c = 3 \text{ x } 10^{8} \text{ m/s}$

$\epsilon_0 = 8.854 \text{ x } 10^{-12} \text{ F/m}$

$\mu_0 = 4\pi \text{ x } 10^{-7} \text{ H/m}$

Variables

λ	Wavelength	[m]
D	Largest Dimension of Antenna	[m]
S_{11}	Reflection Coefficient	[dB]
E^-	Reflected Wave	[V/m]
E^+	Incident Wave	[V/m]
Γ_A	Antenna Reflection Coefficient	[dB]
Z_L	Antenna Load Impedance	[Ω]
R_L	Antenna Load Resistance	[Ω]
X_L	Antenna Load Inductance	[Ω]
Z_A	Antenna Input Impedance	[Ω]
R_A	Antenna Input Resistance	[Ω]
X_A	Antenna Input Inductance	[Ω]

D	Directivity	[dB]
D_{max}	Maximum Directivity	[dB]
U	Radiation Intensity	[W/unit solid angle]
U_{max}	Maximum Radiation Intensity	[W/unit solid angle]
U_0	Radiation Intensity of Isotropic Source	[W/unit solid angle]
P_{rad}	Total Radiated Power	[W]
θ	Elevation Angle	[rad]
ϕ	Azimuth Angle	[rad]
s	Distance of Antenna Feed to Reflector	[m]
E	Total Radiated Field	[dBμV/m]
E_0	Radiated Field of an Isolated Element	[dBμV/m]
r	Vector Distance	[m]
t	Antenna Omnidirectional Pattern	[dB]
k	Wave Number	[rad/m]
ψ	Relative Phase Angle	[rad]
$\hat{a}_n$	Relative Coordinate Vector	[m]
α	Angle of Reflector	[rad]
Z_{mn}	Self Impedance (for m=n)	[Ω]
Z_{mn}	Mutual Impedance (for m$\neq$n)	[Ω]
$Z_{x,y}$	Impedance Between xth and yth Antenna Element	[Ω]
I_n	Current at the Terminals of nth Antenna Element	[A]
Γ_S	Active Reflection Coefficient	[dB]

S_{mn}	Coupling Coefficient	[dB]
ν_n	Excitation Coefficient of Element n	[dB]
ν_m	Excitation Coefficient of Element m	[dB]
φ	Phase Shift	[rad]
P_r	Power Received	[W]
P_t	Power Transmitted	[W]
A	Radar Cross Section or Echo Area	[m^2]
G_t	Gain of Transmitting Antenna	[Dimensionless]
G_r	Gain of Receiving Antenna	[Dimensionless]
R_1	Observation Distance from Target to Transmitting Antenna	[m]
R_2	Observation Distance from Target to Receiving Antenna	[m]
f_D	Doppler Frequency Shift	[Hz]
v	Velocity of Moving Target Relative to Stationary Radar	[m/s]
κ	Incident Angle	[rad]
f_t	Transmitted Frequency	[Hz]
c	Speed of Light	[m/s]
λ_t	Radar Transmitted Wavelength	[m]
λ_{irr}	Wavelength of Irregularities	[m]
ξ	Scattering Angle	[rad]
I_n	Current in Wire n	[A]
ρ_n	Radius of Wire n	[m]
$\varpi_{m,i}$	Prediction Error	[Dimensionless]

$PL_{meas,i}$	Measured Value	[Dimensionless]
$PL_{m,i}$	Predicted or Simulated Value	[Dimensionless]
m	Model	[Dimensionless]
N	Number of Sample Frequencies	[Dimensionless]
a	Radius of Sphere	[m]
ka	Relative Size	[Dimensionless]
rl	Radian Length	[m]
ϵ_r	Relative Permitivity	[Dimensionless]
σ	Conductivity	[S/m]
ϵ	Permitivity	[F/m]

Acronyms

SuperDARN	Super Dual Auroral Radar Network
HF	High Frequency
GPS	Global Positioning System
SANSA	South African National Space Agency
SANAE	South African National Antarctic Expedition Station
TTFD	Twin Terminated Folded Dipole
EM	Electromagnetic
AF	Array Factor
PEC	Perfect Electric Conductor
LPDA	Log Periodic Dipole Array
Radar	Radio Detection and Ranging

T2FD	Tilted Folded Dipole Folded
ARC	Active Reflection Coefficient
CEM	Computational Electromagnetics
EMC	Electromagnetic Compatibility
MoM	Method of Moments
RL-GO	Ray Launching Geometrical Optics
ESA	Electrically Small Antenna
TM	Transmission Line
RAM	Random Access Memory
GB	Gigabyte
AUT	Antenna Under Test
RMSE	Root-Mean-Square-Error
ISO	Isometric
CHPC	Centre for High Performance Computing

Chapter 1

Introduction

1.1 SuperDARN Antenna Array

The Super Dual Auroral Radar Network (SuperDARN) is a world-wide joint effort of engineers and scientists who monitor and perform research on earth's near-space plasma environment. As of 01 January 2018 this group uses 36 high frequency (HF) radars [1], which use backscatter from magnetic field-aligned plasma irregularities to measure the doppler velocity of the ionosphere in order to study space weather manifested in the earth's magnetic field (magnetosphere) and ionosphere. The movements of these irregularities are tied to the magnetic reconnection of the earth's magnetic field with the solar wind of the interplanetary medium.

Space weather impacts many technological systems including Global Positioning System (GPS), spacecraft orbits, electrical power distribution, surveillance radar, HF communications and transpolar aviation. In South Africa, SuperDARN data is used by engineers and scientists at, and affiliated with, the South African National Space Agency's (SANSA) Space Science Directorate. SANSA also maintains and operates its own SuperDARN radar from the South African National Antarctic Expedition Station (SANAE IV) in Antarctica.

The SuperDARN radar uses a 16-element twin terminated folded dipole (TTFD) phased array to transmit and receive $300\mu s/100\mu s$ pulses at up to 2.4 kW per antenna over a frequency range between 8 MHz and 20 MHz. One of the challenges of such a physically large array is that it is very difficult to characterize the beam-shape and pointing direction using traditional, far-field techniques. The approach is expensive, logistically demanding and in most cases results in inaccurate and sparse data [2, 3]. Therefore a simulation approach is to be used to characterise the SuperDARN radar antenna array. However, this in turn has its own challenges and drawbacks.

1.2 Project Objectives

This section considers the various objectives this project will achieve to correctly characterise the directivity of the full-scale SuperDARN radar antenna array with the aim of improving the front-to-back ratio of the radar.

First, a scale model of the SuperDARN radar elements needs to be designed in an EM software solver and simulated to determine whether the simulation results of the scale model are comparable to those of the physically constructed scale model. Next, the scale model needs to be manufactured to measure the antenna characteristics in Stellenbosch University Electrical and Electronics's anechoic chamber. Afterwards, the measured results can be compared to that of the simulated results as a proof of concept that the simulation results from the EM software solver are an accurate representation of the real-world antenna characteristics. Once confidence has been achieved in the EM solver software, a simulation of the full-scale SuperDARN radar antenna array in Altair Hyperworks FEKO allows various set-ups to be run to characterise the current make-up of the array. This includes the currently installed half-corner reflector as well as considering the influence of simulating ground conditions of the Antarctic base. Finally, improvements will be suggested on the current SuperDARN radar set-up and to recommend practical upgrades on the system.

1.3 Project Overview

Chapter 2 contains the literature review which describes all the definitions, concepts and practices used to go from simulating and measuring a scale model, to the simulation of the full-scale SuperDARN radar antenna array. It first looks at common terminologies used with respect to general antenna parameters and then moves on to explain the concept of a corner reflector antenna with a specific focus on the 90° corner reflector antenna. The SuperDARN radar is then looked at by first describing the operations of a general radar system and then moves on to the specifics of the SuperDARN radar's operations and make-up in terms of the TTFD construction and the array's phasing. Through previous work done on scale modelling, a scale model concept is discussed and it is seen that the 1250:50 impedance transformer will need to be replaced with a sleeve balun to have the scale model mimic the operations of the full-scale model. An EM solver software was required to design and evaluate both the scale model and the full-scale model; for this project Altair Hyperworks FEKO was used. In the earlier stages of this project, it was discussed to use a multicopter with an electrically small antenna (ESA) for on-site characterisation of the SuperDARN radar beam and although this idea was replaced with simulation characterisation, the concept of an ESA was discussed and some initial prototypes are provided.

In chapter 3 the scale model is discussed further with a 1:100 scale model being designed. It describes how the antenna dimensions, operating frequency, and characteristics are altered to achieve an accurate scale model. The addition of the sleeve or bazooka balun is discussed in detail and which design parameters need to be met to have it operating at maximum efficiency. The simulation set-up of two scale models, built in FEKO, are considered in great detail and are then compared to the same models measured in the anechoic chamber of the Electrical and Electronic Engineering Faculty at Stellenbosch University. After explaining the discrepancies between the simulated versus measured results, it was determined that the FEKO software would be able to provide sufficiently accurate results of the full-scale model.

After confidence in the FEKO software has been established chapter 4 moves on to look at the full-scale SuperDARN radar simulated in FEKO. The current installed radar set-up with its 90° half corner wire reflector is first evaluated over an infinite perfect electric conductor (PEC) ground and then compared to the model over an infinite granite ground layered with a 1 m thick ice layer at -1°C. From here four more 90° half corner wire reflector layouts are simulated and evaluated. Finally moving on to four 90° full corner wire reflectors with the best design being chosen. A realistic ground-plane model of the SuperDARN radar with the 90° half corner wire reflector currently installed at SANAE IV base and the proposed 90° full corner wire reflector were also run using CHPC's computing resources and various discrepancies between the ideal ground-plane model and realistic ground-plane model are seen and discussed.

Chapter 5 ends the thesis with a detailed discussion on the results, recommendations on moving forward with the project and a conclusion.

Chapter 2

Literature Study

2.1 Introduction

This chapter will consider at all relevant definitions, concepts, parameters and practices for the project scope. It includes the following: the radiation parameters and definitions required antenna designs used in the SuperDARN radar array and their principles; design methods used to improve the performance of the scaled model; and simulation software methods used to characterise antennas.

2.2 Radiation Parameters and Definitions

The SuperDARN radar array in Antarctica operates as both a transmitting and receiving antenna. As such the array will be considered in the transmitting and receiving modes.

2.2.1 Electromagnetic Field Regions

The electromagnetic (EM) field regions surrounding an antenna are divided between the near-field and far-field regions, with the near-field region being further sub-divided into the reactive and radiative near-field regions. Which are shown in figure 2.1.

The near-field (reactive) region is more of a generation zone of radiation. This reactive region is defined by the spherical equation:

$$Near - Field\ Reactive\ Region \leq 0.62\sqrt{\frac{D^3}{\lambda}} \tag{2.1}$$

D = Largest Dimension of Antenna (m)
λ = Wavelength(m)

The near-field (radiating) region, or Fresnel region, of an antenna, is the region where the EM fields begin to transition more towards radiating fields or in other words where the EM waves begin to become more planar waves in nature. Though not entirely planar as the angular field distribution is dependant on the distance the wave has travelled from the antenna. This spherical region surrounding the antenna that is described by the equation:

$$Near - Field\ Radiating\ Region \geq 0.62\sqrt{\frac{D^3}{\lambda}} \text{ and } \leq \frac{2D^2}{\lambda} \tag{2.2}$$

The far-field, or Fraunhofer region, encompasses the entire region beyond the radiating near-field region. In this region, the angular field distribution is no longer dependent on the distance the EM wave has travelled from the antenna, for this reason, it is assumed that any EM waves radiated from an antenna, travelling in this region are planar waves. Meaning that the electric and magnetic fields are perpendicular to each other as well as both of them being perpendicular to the direction of propagation. The far-field region is defined by the equation:

$$Far - Field\ Region > \frac{2D^2}{\lambda} \tag{2.3}$$

However, in practice this region should be considered at a distance of 5λ from the point of antenna radiation so as to ensure the EM waves are truly planar [4].

For this project the far-field region of the SuperDARN radar was of most interest as the azimuth and elevation angles in this region are to be determined. One parameter that can have a great influence on an antenna's far-field characteristics is the reflection coefficient (S_{11}) of an antenna set-up which will be discussed in the following section.

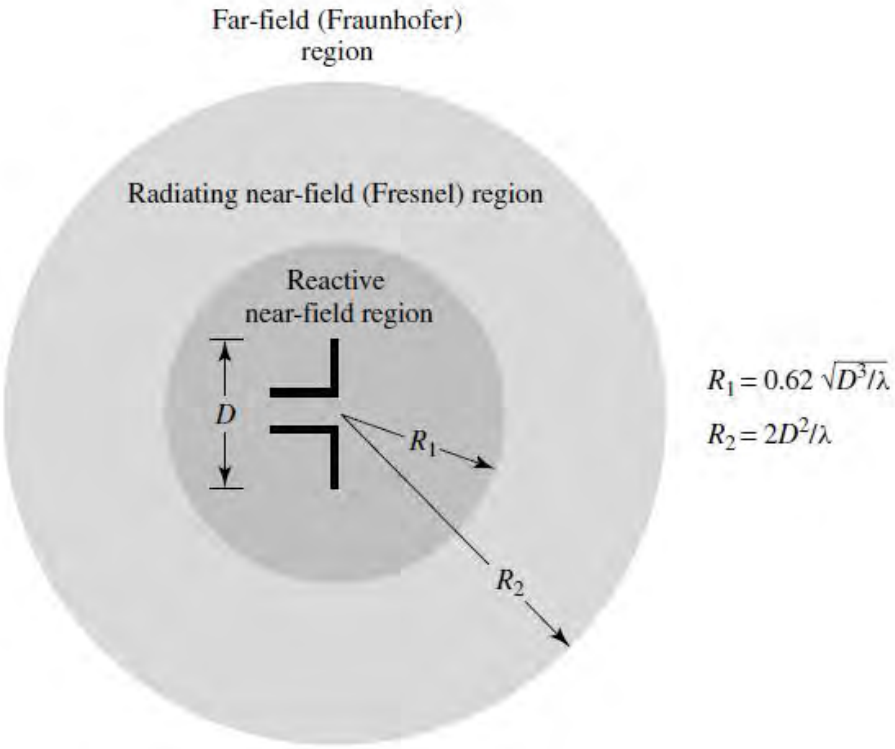

Figure 2.1: Near-field and far-field regions of an antenna [4]. The figure above shows the break-down of the various sections of the field regions.

2.2.2 Reflection Coefficient

The reflection coefficient (S_{11}) which will be used in the project, is an antenna parameter which describes how efficiently an antenna operates due to the impedance discontinuity in the transmission medium. It is the ratio of how much of the input EM wave is transmitted (incident wave) to how much of the input EM wave is reflected back into the system (reflected wave) and can be calculated using the following equation,

$$S_{11} = log_{10}\left(\frac{E^-}{E^+}\right) \tag{2.4}$$

S_{11} = Reflection Coefficient (dB)
E^- = Reflected Wave (V/m)
E^+ = Incident Wave (V/m)

Another form of this equation can be written as antenna reflection characteristics in terms of antenna load to antenna input impedance with the equation (2.5) below. Equation (2.5) is used when an antenna is loaded with a

known load and the parameters of the antenna are also known.

$$\Gamma_A = log_{10}\left(\frac{Z_L - Z_A}{Z_L + Z_A}\right) \tag{2.5}$$

with

$$Z_L = R_L + jX_L$$

and

$$Z_A = R_A + jX_A$$

Γ_A = Antenna Reflection Coefficient (dB)
Z_L = Antenna Load Impedance (Ω)
R_L = Antenna Load Resistance (Ω)
X_L = Antenna Load Inductance (Ω)
Z_A = Antenna Input Impedance (Ω)
R_A = Antenna Input Resistance (Ω)
X_A = Antenna Input Inductance (Ω)

Due to the fact that the reflection coefficient of a scale model, to be discussed in a later section, was measured with a network analyser, the first equation (2.4) will be used in this project [4].

S_{11} has a great impact on the efficiency of an antenna and therefore an impact on the realised gain of said antenna. Though the S_{11} is a key parameter to consider when determining the optimal design of an antenna, this project will not use the S_{11} to design an optimal antenna but rather as a characteristic to compare measured results to simulated results in chapter 3. The directivity of the SuperDARN radar antenna array is the main antenna characteristic this project considers in later chapters but the theory is discussed in the next section.

2.2.3 Directivity

Since this project focuses on an HF antenna array, directivity will be considered rather than realised gain. This is due to the inherent complications of calculating realised gain for each antenna element using their respective reflection coefficient and then super-imposing all the results to acquire the total realised gain of the entire array.

Directivity can be described mathematically as the ratio of radiation intensity in a given direction (U) to the radiation intensity averaged over all directions (U_0) as seen by the two equations (2.6) and (2.7) below.

$$D = \frac{U}{U_0} = \frac{4\pi U}{P_{rad}} \tag{2.6}$$

with

$$D_{max} = D_0 = \frac{U_{max}}{U_0} = \frac{4\pi U_{max}}{P_{rad}} \tag{2.7}$$

D = Directivity (dB)
D_{max} = Maximum Directivity (dB)
U = Radiation Intensity (W/unit solid angle)
U_{max} = Maximum Radiation Intensity (W/unit solid angle)
U_0 = Radiation Intensity of Isotropic Source (W/unit solid angle)
P_{rad} = Total Radiated Power (W)

Put simply it is an antenna parameter which measures or describes how directional the radiation pattern of a given antenna is [4].

Two more antenna characteristics of the SuperDARN radar antenna array which this project will consider to calculate are the azimuth and elevation angles of said array's far-field directivity pattern.

2.2.4 Azimuth and Elevation Angles

Aside from directivity, the azimuth (ϕ) and elevation (θ) angles of the SuperDARN radar array are the two most important parameters that need to be determined through this project.

θ = Elevation Angle (rad)
ϕ = Azimuth Angle (rad)

From figure 2.2, the azimuth angle is defined as the vertical angle of the maximum point of EM field intensity from the origin of the far-field coordinate system. While the elevation angle is the horizontal angle of the same point [4].

One way to improve directivity, is to add a corner reflector to an antenna set-up. This is exactly what the SuperDARN radar antenna array at the SANAE IV base does and this concept of a corner reflector will be considered in more detail in the following section.

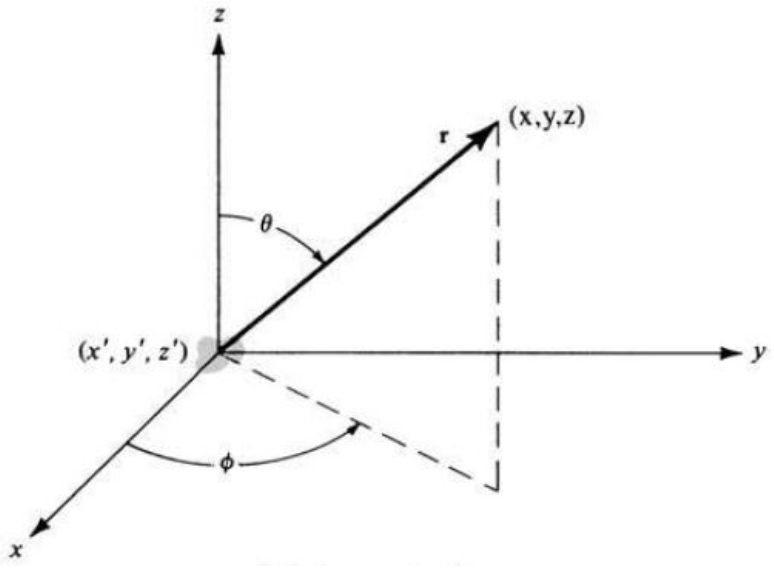

Figure 2.2: Elevation and azimuth angles [4]. This figure shows the axis from which the respective elevation and azimuth angles are taken from.

2.3 Corner Reflector

This project looks at improving the front-to-back ratio of the SuperDARN radar as it has been shown that if the backwards radiation has considerable power it will complicate data analysis as backscatter signals are received from unwanted paths [5]. The only practically achievable change to the currently installed antenna array, is to improve on the half-corner reflector design and consider a full 90° corner reflector design. So the section is added to provide the background theory to better understand how these reflectors work and how they should be applied. A dipole antenna has a torus or doughnut shaped omnidirectional radiation field pattern, one way to improve the directivity of such an antenna is to add a corner reflector to the system. The corner reflector improves directivity in two ways, the first is to impede or hinder radiation in the reverse direction while the second is to guide radiation in the forward direction [4].

When a corner reflector is added to the system it does improve the directivity of the antenna. However, a trade-off for increased directivity is the increase in the number of side lobes. The directivity and number of side lobes are further increased as the angle of the corner reflector is decreased [4] so a middle ground needs to be found between the two. An excess of side lobes is an unwanted characteristic for the SuperDARN radar antenna array as the array focuses the beam to one central point in free space and side lobes would hinder the array's operation. Side lobes mean that unwanted signals can enter the radar from unknown directions. This confuses the result either in terms of

direction or doppler shift. Due to this fact as well as the infrastructure that is already in place at the SANAE IV base, this project will focus mainly on a 90° corner reflector, though other common corner reflectors include 30°, 45°, 60° and parabolic reflectors [4]. To characterise the radiation pattern of a corner reflector system, image theory must be used [4] and is considered in the next subsection.

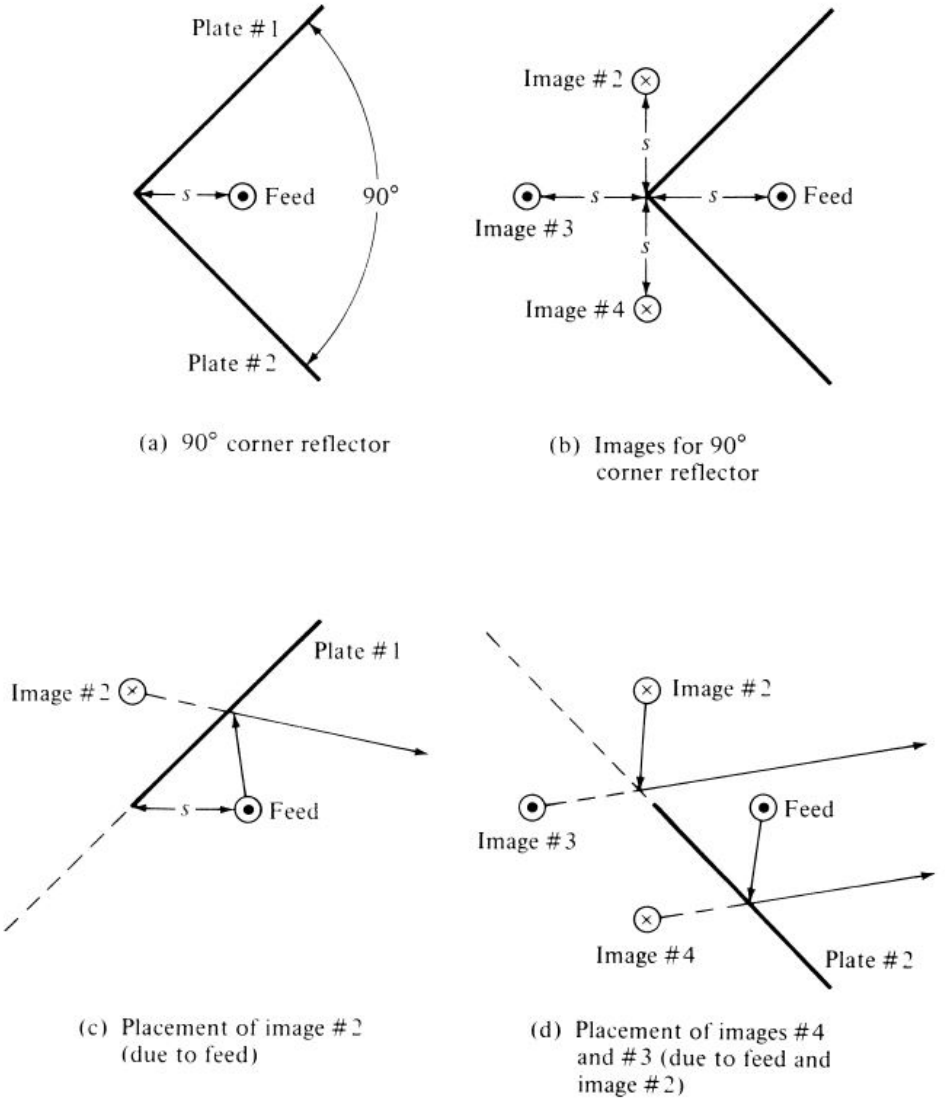

Figure 2.3: 90° corner reflector [4]. These figures show the image placement due to source and corner reflector positioning.

In figure 2.3 the 90° corner reflector can be seen with all of its images, 2.3(b), and the total radiated field intensity can be determined by combining the field from the feed with the field from the images, giving the equation:

$$\mathbf{E}(r,\theta,\phi) = \mathbf{E_1}(r_1,\theta,\phi) + \mathbf{E_2}(r_2,\theta,\phi) + \mathbf{E_3}(r_3,\theta,\phi) + \mathbf{E_4}(r_4,\theta,\phi) \tag{2.8}$$

With the normalised scalar field as:

$$E(r,\theta,\phi) = t(\theta,\phi)\frac{e^{-jkr_1}}{r_1} - t(\theta,\phi)\frac{e^{-jkr_2}}{r_2} + t(\theta,\phi)\frac{e^{-jkr_3}}{r_3} - t(\theta,\phi)\frac{e^{-jkr_4}}{r_4}$$

$$E(r,\theta,\phi) = [e^{+jkscos\psi_1} - e^{+jkscos\psi_2} + e^{+jkscos\psi_3} - e^{+jkscos\psi_4}]t(\theta,\phi)\frac{e^{-jkr}}{r} \tag{2.9}$$

where

$$cos\psi_1 = \hat{\mathbf{a}}_x \cdot \hat{\mathbf{a}}_r = sin\theta cos\phi \tag{2.10a}$$
$$cos\psi_2 = \hat{\mathbf{a}}_y \cdot \hat{\mathbf{a}}_r = sin\theta sin\phi \tag{2.10b}$$
$$cos\psi_3 = -\hat{\mathbf{a}}_x \cdot \hat{\mathbf{a}}_r = -sin\theta cos\phi \tag{2.10c}$$
$$cos\psi_4 = -\hat{\mathbf{a}}_y \cdot \hat{\mathbf{a}}_r = -sin\theta sin\phi \tag{2.10d}$$

with $\hat{\mathbf{a}}_r = \hat{\mathbf{a}}_x \mathrm{sin}\theta\mathrm{cos}\phi + \hat{\mathbf{a}}_y \mathrm{sin}\theta\mathrm{sin}\phi + \hat{\mathbf{a}}_z \mathrm{cos}\theta$, equation (2.9) can be re-arranged using equations (2.10a) - (2.10d) to

$$E(r,\theta,\phi) = 2[cos(ks\ sin\theta cos\phi) - cos(ks\ sin\theta sin\phi)]t(\theta,\phi)\frac{e^{-jkr}}{r} \tag{2.11}$$

for $\alpha = \pi/2 = 90°$

$$0 \leq \theta \leq \pi, \qquad \begin{matrix} 0 \leq \phi \leq \dfrac{\alpha}{2} \\ 2\pi - \dfrac{\alpha}{2} \leq \phi \leq 2\pi \end{matrix} \tag{2.12}$$

If the radiating field of a single isolated element is set to

$$E_0 = t(\theta,\phi)\frac{e^{-jkr}}{r} \tag{2.13}$$

Equation (2.11) can be written as

$$\frac{E}{E_o} = AF(\theta,\phi) = 2[cos(ks\ sin\theta cos\phi) - cos(ks\ sin\theta sin\phi)] \tag{2.14}$$

s = Distance of Antenna Feed to Reflector (m)
E = Total Radiated Field (dBμV/m)
E_0 = Radiated Field of an Isolated Element (dBμV/m)

r_n = Relative Vector Distance (m)
t = Antenna Omnidirectional Pattern (dB)
$k = \frac{2\pi}{\lambda}$ = Wave Number (rad/m)
ψ_n = Relative Phase Angle (rad)
$\hat{\mathbf{a}}_n$ = Relative Coordinate Vector (m)
α = Angle of Reflector (rad)
AF = Array Factor

Equation (2.14) allows the total radiated field to be evaluated as a ratio to the radiated field of an isolated element as well as representing the array factor of the whole corner reflector set-up [4].

The installed set-up of the SuperDARN radar at SANAE IV base makes use of a half corner reflector, which means, when looking at figure 2.3(a) only plate number 1 is included in the set-up and plate number 2 is removed entirely. Later sections of this project will consider the performance of this half corner reflector compared to the performance of a full corner reflector, i.e., both plate number 1 and number 2 are included in the set-up. It will also consider how a full corner reflector improves the front-to-back ratio, which is merely the ratio of directivity in the forward direction to the directivity in the reverse direction when compared to a half corner reflector. Hence the need to consider the corner reflector in more detail and to consider different layouts and configurations.

2.3.1 Image Theory

Corner reflector antennas work based off of a certain EM principle called image theory, with the image placement due to source and corner reflector positioning as shown in figure 2.3 and will be considered in this section. Image theory states that for any given charge configuration set-up above an infinite perfect electric conductor (PEC) can be replaced with the charge configuration itself, a virtual charge configuration otherwise called an image reflected about the plane of the PEC and replacing the PEC with an equipotential surface along the plane of the PEC [4].

Figure 2.4(a) shows a simple set-up of a linear element, placed in free space, some distance h above an infinite PEC ground-plane. As can be seen, an image of this linear element is reflected about the plane of the PEC at a distance of h and placed inside the PEC region. Two arbitrary points P_1 and P_2 are located at some distance from the actual source in free space. To determine the radiated field intensity (E) at these points, the direct wave and reflected wave must be considered. Though the energy is radiated in all directions from the actual source, the direct wave seen by P_1 and P_2 travels along a straight line on the shortest path between the actual source and either P_1 or P_2. Another wave from the source radiates to point R_1 at an angle θ_1^i for P_1 or point R_2

at an angle θ_2^i for P_2 and is reflected towards the corresponding point P. The reflected wave travels along the shortest path with $\theta^i_{1\ or\ 2} = \theta^r_{1\ or\ 2}$ as has been determined by the law of reflection. If the line of the reflected wave is extended back through the equipotential surface as seen in 2.4(b), it can be said that the reflected wave originates from the image and boundary conditions can be used to determine the polarisation of the image. Since this technique uses both

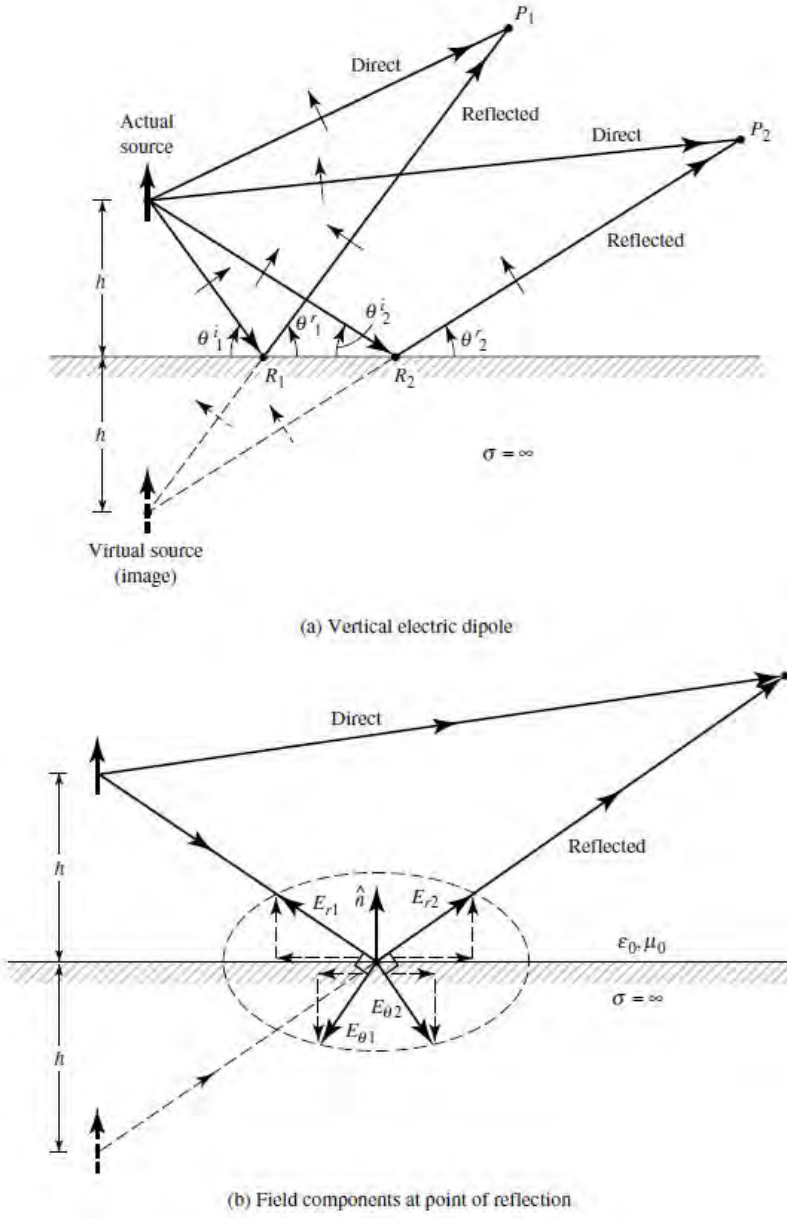

Figure 2.4: Image theory [4]. The figure above show the virtual source, direct and reflected waves due to the actual source placement, as well as the electric field components at the point of reflection due to the actual source.

real and imaginary charge configurations it can be assumed that they do not couple to one another [4].

This section has considered the theory behind corner reflectors. The following section will examine how this theory has been implemented to the SuperDARN radar to hinder backwards radiation to ensure the correct EM signals are captured by the radar for data analysis.

2.4 Phased Array

A phased array is an array of antennas in which each phase of each signal that feeds each antenna are set in such a way that the EM radiation pattern of the entire array points towards a desired direction and the signals propagating toward undesired directions are suppressed [6].

The following section will discuss some of the topics which influence the efficiency and performance of phased arrays, specifically the SuperDARN radar which is a linear phased array.

2.4.1 Mutual Coupling

Mutual coupling between antenna elements in an array is the energy absorbed by one antenna's receiver when one or more antennas are in nearby operation to that antenna [7]. This mutual coupling is an undesirable effect since the energy that should be radiated out from one antenna is absorbed by another antenna or the energy that should have been captured by the desired receiver is absorbed by an undesired antenna in the array. Due to this, mutual coupling reduces the efficiency and overall performance of the array in both the transmitting and receiving modes [8].

This reduction in efficiency and performance of the array is due to the affect mutual coupling has on the individual antenna parameters making up the array, which are discussed in the following sections.

2.4.1.1 Antenna Impedance

The impedance of an antenna at its terminal is one of the most significant factors which affect the radiation pattern of said antenna. Due to the presence of mutual coupling the antenna impedance of a phased array is notably dissimilar to that of an isolated element, with the impedance matrix of an array

of N-elements given by [8]:

$$Z = \begin{bmatrix} Z_{11} + Z_L & Z_{12} & \cdots & Z_{1N} \\ Z_{21} & Z_{22} + Z_L & \cdots & Z_{2N} \\ \vdots & \vdots & \ddots & \vdots \\ Z_{N1} & Z_{N2} & \cdots & Z_{NN} + Z_L \end{bmatrix}$$

with,

Z_{mn} = Self Impedance (for m=n) (Ω)
Z_{mn} = Mutual Impedance (for m$\neq$n) (Ω)

Using this impedance matrix, the impedance at the antenna terminal can be expressed as [8]:

$$Z_x = \sum_{y=1}^{N} Z_{x,y} \frac{I_y}{I_x} \tag{2.15}$$

with,

$Z_{x,y}$ = Impedance Between xth and yth Antenna Element(Ω)
I_n = Current at the Terminals of nth Antenna Element (A)

Mutual coupling between antenna elements also affects the reflection coefficient of each antenna element which is considered in the following section.

2.4.1.2 Active Reflection Coefficient

For a linear array, if all the antenna elements of the array are excited simultaneously, the active reflection coefficient (ARC) is the linear superposition of elements' reflection coefficient (S_{11}) and the mutual coupling from adjacent elements [9].

The ARC for antenna element m in an array of N elements can be expressed using the following equations [10]:

$$\Gamma_S = \sum_{n=1}^{N} S_{mn} \frac{\nu_n}{\nu_m} \tag{2.16}$$

with,

Γ_S = Active Reflection Coefficient (dB)
S_{mn} = Coupling Coefficient (dB)
ν_n = Excitation Coefficient of Element n (dB)
ν_m = Excitation Coefficient of Element m (dB)

The sections above have considered how mutual coupling between antenna elements of an array affect the individual antenna impedance and ARC parameters, causing a change in the overall performance and efficiency of the array. The next section will look at how a phased array steers its beam through the array's field of view, for the case of the SuperDARN the field of view is $\phi = 52.4°$ [18].

2.4.2 Beam Steering

A device called a phase shifter is used in part of the feeding electronics for the antennas of a phased array. This phase shifter is controlled electronically to produce a phase shift (φ) which is required to steer the beam of the phased array through its field of view [10].

The phase shift is determined using the equation [11];

$$\varphi = \frac{2\pi d}{\lambda} sin(\phi) \tag{2.17}$$

with,

d = Distance Between Antennas (m)

By applying equation 2.17 the phase shifters of the SuperDARN radar are able to control the individual phase shift of each antenna to achieve the desired beam direction or beam steering of the radar [11].

Section 2.4 has considered parameters which influence the efficiency and performance of a phased array. These parameters will not be investigated in the characterisation of the SuperDARN radar for two reasons; firstly for this project directivity, elevation angle and azimuth angle characterisations are the key focus points. Secondly, the SuperDARN radar is already an existing radar in operation so mutual coupling is not something that can be investigated and improved upon. This project will focus on improving the half corner reflector that was installed with the possibility of upgrading it to a full corner reflector.

2.5 SuperDARN

The SuperDARN radar uses a 16-element Twin Terminated Folded Dipole (TTFD) phased array to transmit and receive $300\mu s/100\mu s$ pulses at up to 2.4 kW per antenna over a frequency range between 8 MHz and 20 MHz [2, 3, 12]. However the SANAE IV base, seen in figures 2.5, 2.6 and 2.7, operate their SuperDARN radar at 600 W per antenna. Figure 2.8 show the front and side views of the TTFD antenna element that make up a single antenna in the array. It is important to note that the dimensions in figure 2.8 are not to scale.

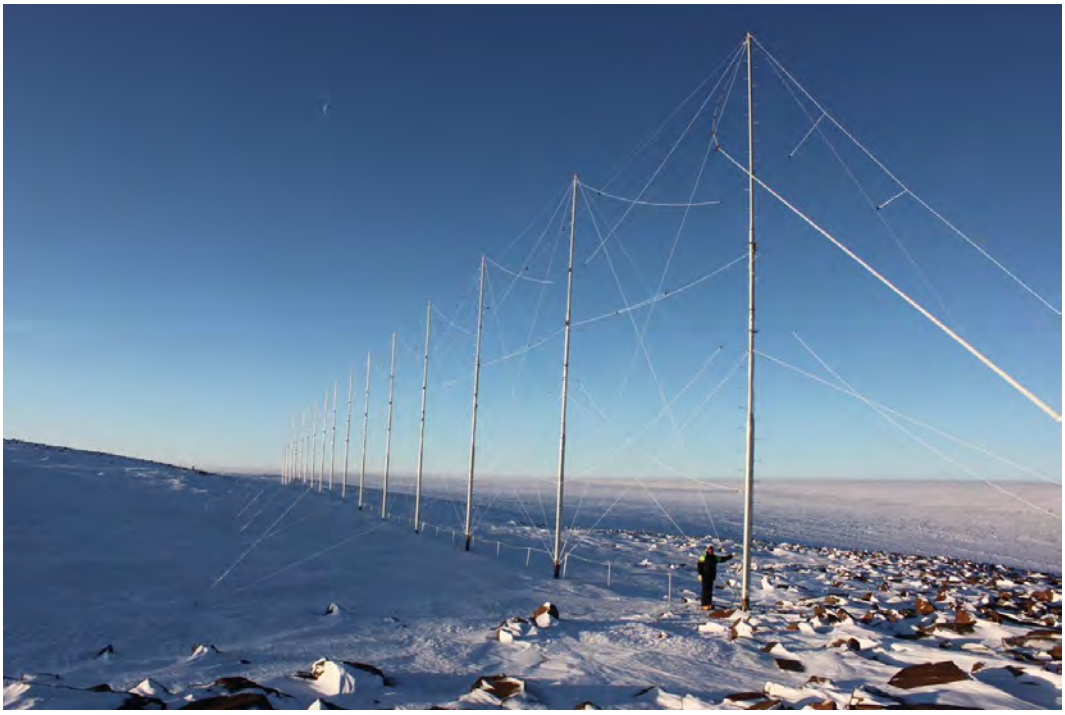

Figure 2.5: Photograph of the SuperDARN radar with the new TTFD antenna elements located at the SANAE IV base in Antarctica [12].

In figure 2.5 the polyester ropes used to suspend the reflector wires forming a 90° half corner reflector can be seen. The SuperDARN radar is situated on top of a granite surface [13] covered with a layer of ice and at the bottom of a cliff face the ice shelf can be seen which is shown in figures 2.6 and 2.7.

Figure 2.6: Aerial view of the SANAE IV base with the base in the top middle of the figure and the SuperDARN radar in the bottom left of the figure [14]. The figure above shows an overview of the SANAE IV base and its location, with the SuperDARN radar's close position to the ice shelf.

Figure 2.7: Aerial view of the SANAE IV base, emphasising the ice shelf [15]. The image above shows an overview of the SANAE IV base and its location, emphasising the height of the base above the ice shelf.

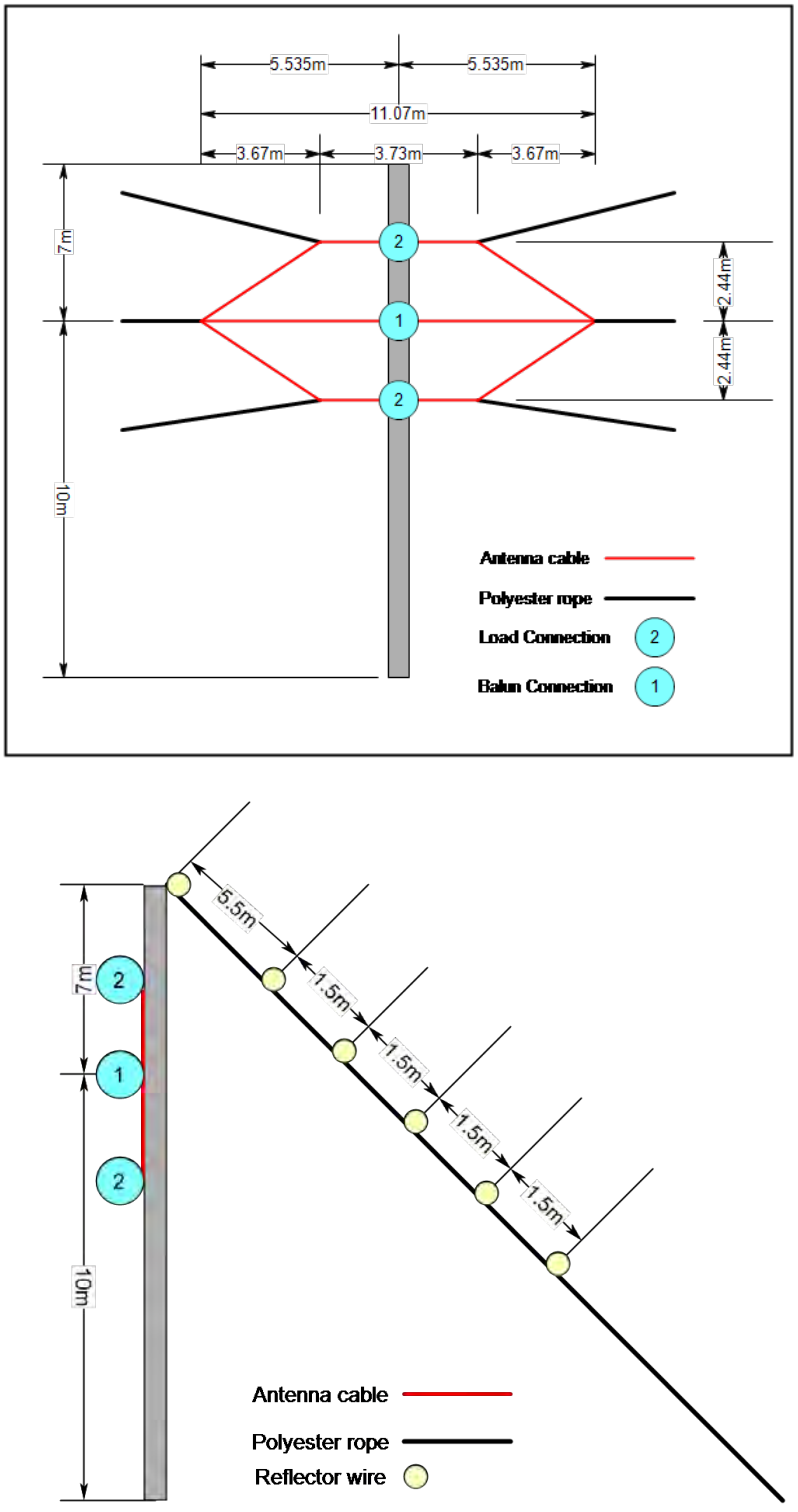

Figure 2.8: (Top) Antenna front view and (bottom) antenna side view. The figures above show the dimensions of the antenna cables which make up the installed construction of the SuperDARN radar antenna element, dimensions not to scale.

2.5.1 Radar

Radar stands for radio detection and ranging. The SuperDARN radar operates as a pulsed radar meaning the radar sends out short bursts (or pulses) of EM signals at a time rather than continuously transmitting an EM signal, which is shown in figure 2.9. The SuperDARN radar operates like any other radar system, as a device to determine the range, echo power and doppler shift and spectral width (velocity) of an object. In the case of the SuperDARN radar these objects are the plasma irregularities along the earth's magnetic field lines in the ionosphere around 200 - 300 km altitude, as seen in figure 2.10. Measuring the time delay from transmitted EM signal to received echo of said transmitted EM signal determines the range of the plasma irregularities, while the echo power is simply the measured power at the received time of the echo. The Doppler shift from transmitted signal to received echo is the change in frequency measured at the time of the received echo [16].

The radar range equation is defined below as the ratio of received power to transmitted power [4].

$$\frac{P_r}{P_t} = A\frac{G_{0t}G_{0r}}{4\pi}\left(\frac{\lambda}{4\pi R_1 R_2}\right)^2 \tag{2.18}$$

P_r = Power Received (W)
P_t = Power Transmitted (W)
A = Radar Cross Section or Echo Area (m^2)
G_t = Gain of Transmitting Antenna (Dimensionless)
G_r = Gain of Receiving Antenna (Dimensionless)
R_1 = Observation Distance from Target to Transmitting Antenna (m)
R_2 = Observation Distance from Target to Receiving Antenna (m)

The doppler shift can be calculated using the equation 2.19 below [4].

$$f_D = 2vcos(\kappa)\frac{f_t}{c} \tag{2.19}$$

f_D = Doppler Frequency Shift (Hz)
v = Velocity of Moving Target Relative to Stationary Radar (m/s)
κ = Incident Angle (rad)
f_t = Transmitted Frequency (Hz)
c = Speed of Light (m/s)

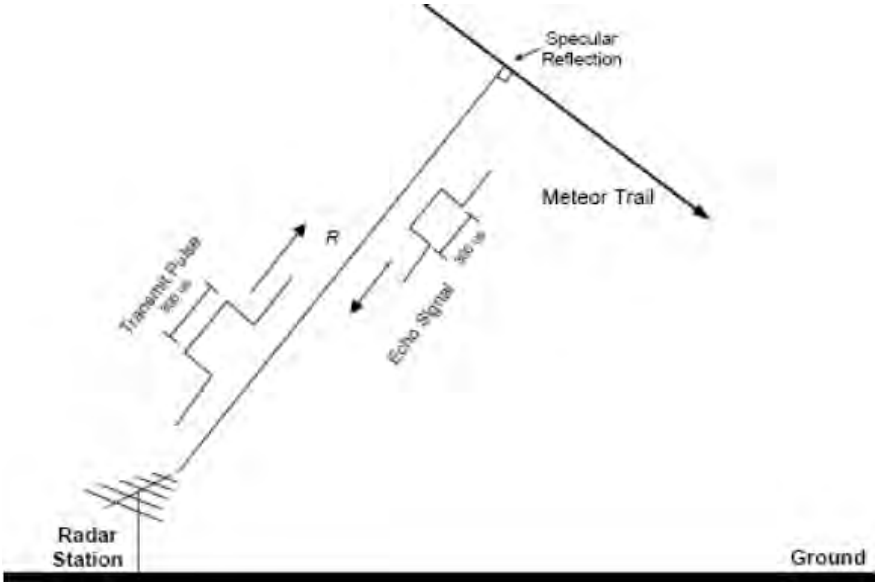

Figure 2.9: Operations of a SuperDARN pulsed radar[16]. The figure above is a visual representation of the pulsing signal the SuperDARN radar uses, with the transmitted pulse path and the echoed signal returning along the same path.

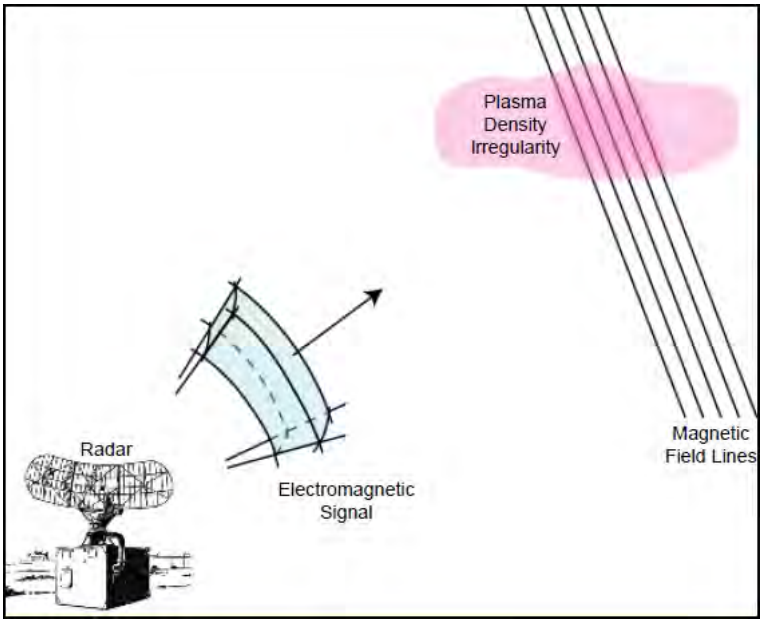

Figure 2.10: Figure showing how the SuperDARN radar's EM signals are transmitted to detect targets [16]. The figure above is a visual representation of the SuperDARN radar's operations and targeting. with the targets (plasma density irregularities) along the earth's magnetic field lines.

It is the spacing of the field-aligned irregularities that are important because the radar uses bragg scattering. Ray orthogonality to magnetic field is critical to receiving back scatter. To achieve this, the SuperDARN radar rely on HF refraction. Hence HF gives both long ranges and refraction. The bragg scattering equation (2.20) which is used can be found below.

$$\lambda_t = 2\lambda_{irr} sin\left(\frac{\xi}{2}\right) \tag{2.20}$$

λ_t = Radar Transmitted Wavelength (m)
λ_{irr} = Wavelength of Irregularities (m)
ξ = Scattering Angle (rad)

The scattering angle (ξ) in equation 2.20 is relative to the incident radio wave in the plane orthogonal to the magnetic field [17].

Originally the SuperDARN radar array at the SANAE IV base was made up of a large Log Periodic Dipole Array (LPDA) but due to the high winds in the area causing damage to the LPDA, they were replaced with the TTFD in 2013-2014 which will be discussed in a following sections [12].

2.5.2 Phasing of SuperDARN Radar

In general, the SuperDARN radar is able to be swept through its field of view by forming a total of 16 beams centred at intervals of 3.3° shown by figure 2.11. The SuperDARN radar located at the SANAE IV base, however, operates with one beam pointing directly outwards from the radar and no beam steering is applied to the radar, at a fixed frequency of 12.75 MHz producing a narrow beam width of 4° [18]. Due to this, the simulations of the full-scale SuperDARN radar discussed in chapter 4 will use the first column of phase values in Appendix C.

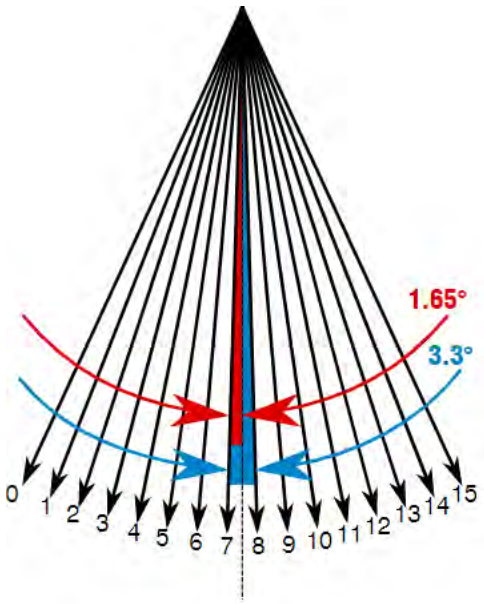

Figure 2.11: Beam directions of the SuperDARN radar. This figure shows how the 16 beams are formed giving an azimuthal sweep of (16x3.3°) = 52.8° [18].

2.5.3 Twin Terminated Folded Dipole

The TTFD antenna element design was used to replace the large LPDA which had previously been installed at the SANAE IV site. For the TTFD to be a viable alternative to the LPDA, the TTFD had to have a similar gain; provide better or equal directivity; have an average beam width of 3° - 5° and be easy to construct thus reducing overall construction costs. The TTFD was designed using the fundamental principles of the standard folded dipole, with similar design criteria to that of the tilted folded dipole folded (T2FD) and the three wire folded dipole. Figure 2.12 clearly shows the single feed wire (wire 1) used to excite the balun, which is a 1250:50 impedance transformer [23], of the TTFD which then feeds the two outer wires (wires 2 and 3) of the antenna. The required antenna operations can be achieved by altering the dimensions, shown in figure 2.12, which make up the construction of the TTFD [19, 20].

R = Terminating Resistance (Ω)
L_1 = Total Length of the Antenna (m)
L_2 = Length of Outer Horizontal Radiating Wire (m)
L_3 = Distance Between Two Central Feed-points (m)
a = Top Wire Spacing (m)
b = Bottom Wire Spacing (m)
c = Antenna Width (m)
S = Node of Three Wires

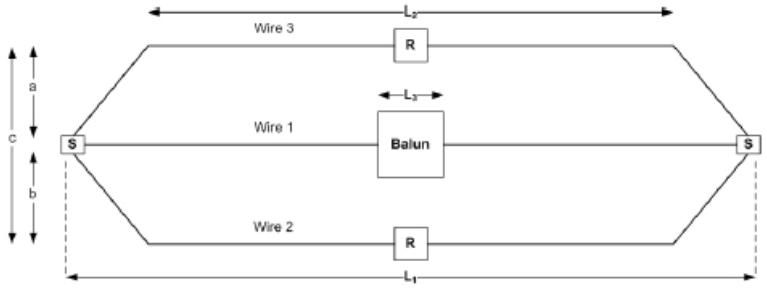

Figure 2.12: TTFD antenna concept [19]. This figure shows the dimensions which make-up the TTFD antenna design.

For the currently installed SuperDARN radar the dimensions of the elements are shown in table 2.1 and the resistors have a value of R = 0 Ω.

Table 2.1: Currently installed SuperDARN radar's TTFD dimensions.

Dimension	Value
L_1	11.07 m
L_2	3.73 m
L_3	0.127 m
a	2.44 m
b	2.44 m
c	4.88 m

To determine the antenna impedance, the currents in the TTFD can first be evaluated and expressed using the following equations [19]:

$$\frac{I_2}{I_1} = \frac{log_{10}\frac{c}{\rho_1} log_{10}\frac{b}{c} - log_{10}\frac{a}{\rho_1} log_{10}\frac{\rho_3}{c}}{log_{10}\frac{\rho_2}{a} log_{10}\frac{\rho_3}{c} - log_{10}\frac{b}{a} log_{10}\frac{b}{c}} \tag{2.21}$$

and

$$\frac{I_3}{I_1} = \frac{log_{10}\frac{a}{\rho_1} log_{10}\frac{b}{a} - log_{10}\frac{c}{\rho_1} log_{10}\frac{\rho_2}{a}}{log_{10}\frac{\rho_3}{c} log_{10}\frac{\rho_2}{a} - log_{10}\frac{b}{c} log_{10}\frac{b}{a}} \tag{2.22}$$

I_n = Current in Wire n (A)
ρ_n = Radius of Wire n (m)

Once the currents have been evaluated, the three currents can be summed together to determine the total antenna current and the feed-point impedance can be related to the centre point impedance via the following equation [19]:

$$Z_{feed-point} = Z_{centre-point} \frac{I^2_{Total}}{I^2_{Portion}} \tag{2.23}$$

$Z_{feed-point}$ = Feed-point Impedance (Ω)
$Z_{centre-point}$ = Centre-point Impedance (Ω)
I_{Total} = Total Antenna Current (A)
$I_{Portion}$ = Relative Potion of the Total Current in Feed Wire (A)

In this section the TTFD antenna which make up the SuperDARN radar array elements were considered. Due to the fact that the SuperDARN radar array elements currently installed at the SANAE IV base have been designed and implemented, this project will not consider optimising these elements. Instead it will consider the 90° half corner reflector which was installed with the idea that a 90° full corner reflector could be installed at a later date if needed.

To determine whether the Altair Hyperworks FEKO EM software solver can be used with confidence to characterise the full-scale SuperDARN radar, a scale model of the radar was first built and measured to compared to the simulated results. The next section will consider the theory behind building the scale model.

2.6 Scale Modelling

Due to the SuperDARN radar's proximity to the ice shelf, see figures 2.5, 2.6 and 2.7 where the SANAE IV base is located, on-site measurements for characterising of the SuperDARN radar would prove to be a difficult task. For this reason, it was decided that a simulation of the radar would be best for early analysis of its operations. To prove this theory, however, a scale model would need to be built and measured in an anechoic chamber with its results compared to those of the same model built in EM solver [21], to be discussed later. Frequency scales proportionally to scaling size [22] and a scaling factor of 100 was chosen to get the desired operating frequency within the measurement limits of the anechoic chamber.

The SuperDARN radar uses a 1250:50 impedance transformer in the balun [23], this impedance transformer cannot be accurately built for a scale model. For this reason, a sleeve or bazooka balun was designed to replace this impedance transformer of the full-scale radar.

2.6.1 Sleeve or Bazooka Balun

To test whether or not it is possible to acquire an accurate characterisation of the SuperDARN radar antenna array through simulations, a scaled model of the array was to be built and measured in the anechoic chamber of the Electrical and Electronic Engineering Faculty at Stellenbosch University and compare the results to that of the results of the simulated scale model. The design and purpose of the scaled model will be discussed in a later chapter.

However, some of the systems of the full-scale SuperDARN radar antenna array cannot be accurately scaled-down, built and measured, namely the 1250:50 impedance transformer found in the balun of the antenna elements of the radar. For this reason, a sleeve balun was used to replace this impedance transformer in the scale model due to the ease of manufacturing of such a balun and its performance at the designed frequency. The sleeve balun as seen

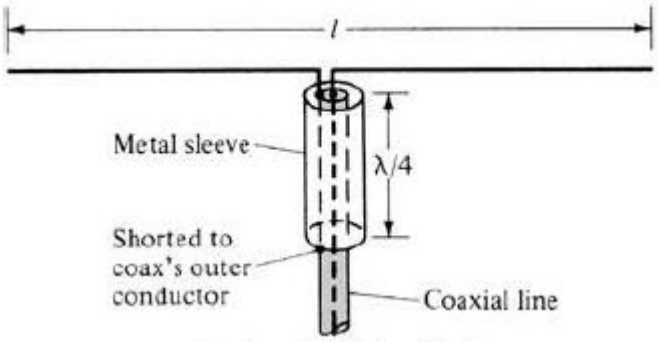

Figure 2.13: Sleeve or bazooka balun[4]. Here the placement of the sleeve balun can be seen, with the furthest point from the radiation shorted to the outer conductor of the coaxial cable and the closest point open.

in figure 2.13 above is made up of a metal tube (in the case of this project copper was used), one-quarter wavelength long, short-circuited to the outer conductor of the coaxial cable at its end furthest from the point of radiation. The open-circuit of the sleeve balun located at the tube end closest to the point of radiation creates an extremely high input impedance, in theory an infinite impedance, which restricts or chokes any current on the outer conductor of the coaxial cable balancing the system. This balancing of the system is due to this high impedance at the open-circuit end of the sleeve balun choking any return currents and forcing them to flow through the inner parts of the coaxial cable [4].

The design of the sleeve balun used in this project follows the fundamentals laid out in [24], though the exact dimensions will be discussed in a later chapter.

2.6.2 Evaluating The Scale Model

The scale model was to be measured in the anechoic chamber of the Electrical and Electronic Engineering Faculty at Stellenbosch University. These measured results then had to be compared to the simulated results of the same scale model built in EM software to have confidence in the simulated results of the full-scale SuperDARN radar antenna array. To determine whether the simulated results are within an acceptable tolerance of the measured results,

this project make use of the root-mean-square-error (RMSE) as this method directly compares the simulated results to the measured results [25].

First the prediction error must be determined using the equation below [25], it is important to note that the prediction error is in linear units;

$$\varpi_{m,i} = PL_{meas,i} - PL_{m,i} \ , \qquad i = 1, 2, ..., N \tag{2.24}$$

$\varpi_{m,i}$ = Prediction Error
$PL_{meas,i}$ = Measured Value
$PL_{m,i}$ = Predicted or Simulated Value
m = Model
N = Number of Sample Frequencies

Then to quantify the model's performance the RMSE equation is applied [25];

$$RMSE = \sqrt{\frac{1}{N}\sum_{i=1}^{N} \varpi_{m,i}^2}, \qquad (dB) \tag{2.25}$$

The equations 2.24 and 2.25 will be used in chapter 3 where the scale models are evaluated. This project will make use of the Altair Hyperworks FEKO EM software package for simulations and to determine the predicted values of the scale models which will be discussed in the next section.

2.7 Electromagnetic Software

This section discusses the simulation tools that were used in the project to characterise the 1:100 scale model and full-scale model of the SuperDARN radar antenna array.

2.7.1 FEKO

Altair Hyperworks FEKO is a comprehensive computational electromagnetics (CEM) simulation software which is extensively used in various defence, telecommunications, aerospace and automobile industries which require solutions to various EM problems. FEKO can solve a variety of EM problems using both frequency and time domain EM solvers. The complexity of the solver methods used in the FEKO software allows for accurate analysis of antenna, microstrip circuits, RF components, biomedical systems and electromagnetic compatibility (EMC) analysis amongst other EM problems [26].

2.7.2 Solver

The FEKO EM software has many different solver options, this project makes use of the method of moments (MoM) and ray launching geometrical optics (RL-GO) solvers.

2.7.2.1 Method of Moments

The MoM solver uses moderate amounts of computing resources, is a numerical technique that solves electromagnetic problems at their boundary using integral equation techniques of Maxwell's equations and, when used in the FEKO EM software, is used as a frequency-domain solver[26, 27].

2.7.2.2 Ray Launching - Geometrical Optics

The RL-GO solver uses ray methods based on optical propagation, reflection and refraction theory to model objects using these ray-based methods. This solver is used for problems that are electrically huge dielectric and metallic and uses a moderate to low amount of computing resources [26].

2.7.3 Source

This section will deal with the different port excitations used during the various simulation set-ups in this project. First considering waveguide ports used in the scale single element model, then the edge ports used in the scale three element model and finally the wire ports used in the full-scale model [26].

2.7.3.1 Waveguide Port

A waveguide port is used when a model contains a waveguide structure and the structure is used to apply an excitation signal to the model. FEKO supports three types of waveguide cross-sections; rectangular waveguide, circular waveguide, and coaxial waveguide. This project will make use of the coaxial waveguide as a coaxial cable is used to excite the antenna element in the scale single element model [26].

2.7.3.2 Edge Port

An edge port is used when a model contains an edge which is between two sets of faces. Once the edge port is added to the model the parts which contain the faces must be defined as one part for the port to be valid [26].

2.7.3.3 Wire Port

A wire port is a port placed on a wire geometry which connects two parts together or even just a model made completely from wire geometry [26].

2.8 Conclusion

The various EM principles and antenna characteristics to be used in this project were first discussed. The operation and make-up of the SuperDARN radar antenna, the specific HF antenna to be characterised in this project, were then discussed. One area of concern was raised, namely the half corner reflector currently installed to the radar located at the SANAE IV base and whether or not a full corner reflector would be better suited for the SuperDARN radar's current operations. The chapter then considered how to go about answering this question, firstly a scale model was to be built and measured in the anechoic chamber of the Electrical and Electronic Engineering Faculty at Stellenbosch University. Then the results of this scale model are to be compared to the results of the same model built in an EM software package, in the case of this project FEKO was the chosen software. The process of comparing the measured results to the simulated results of the scale model verifies that the EM software package calculates similar results to that of the real-world model and the results will be accurate in terms of the full-scale simulation model of the radar in operation at the SANAE IV base in Antarctica.

Chapter 3

Measurement and Simulation of Scale Model

3.1 Introduction

This chapter will discuss the design and results of the 1:100 scale model built during this project. The scale model was built and antenna characteristics measured to determine if the simulation results acquired, through the use of the FEKO EM solver software, are sufficiently accurate. By using a scale model to compare simulation versus measured results through the RMSE analysis method, the findings can then be used to state whether or not the simulation results of the installed set-up of the full-scale SuperDARN radar model are accurate and any changes made to the full-scale model in simulation are a true real-world representation of the change's effects on the entire system. The RMSE of the scale models must lie within 8 - 9 dB [28] to provide confidence in the FEKO software.

3.2 Design

The full-scale SuperDARN radar operates between 8 - 20 MHz. To achieve an operating frequency that can be measured in Stellenbosch University Electrical and Electronics's anechoic chamber a 1:100 scale model was designed and built. The table 3.1 below shows the changes in antenna operations.

Table 3.1: Changes in antenna characteristics from full-scale to 1:100 scale model.

Model	**Operating Frequencies**	**Wavelengths**	**One-Quarter Wavelengths**
Full-Scale	8 - 20 MHz	37.5 - 15 m	9.375 - 3.75 m
1:100 Scale Model	0.8 - 2 GHz	375 - 150 mm	93.75 - 37.5 mm

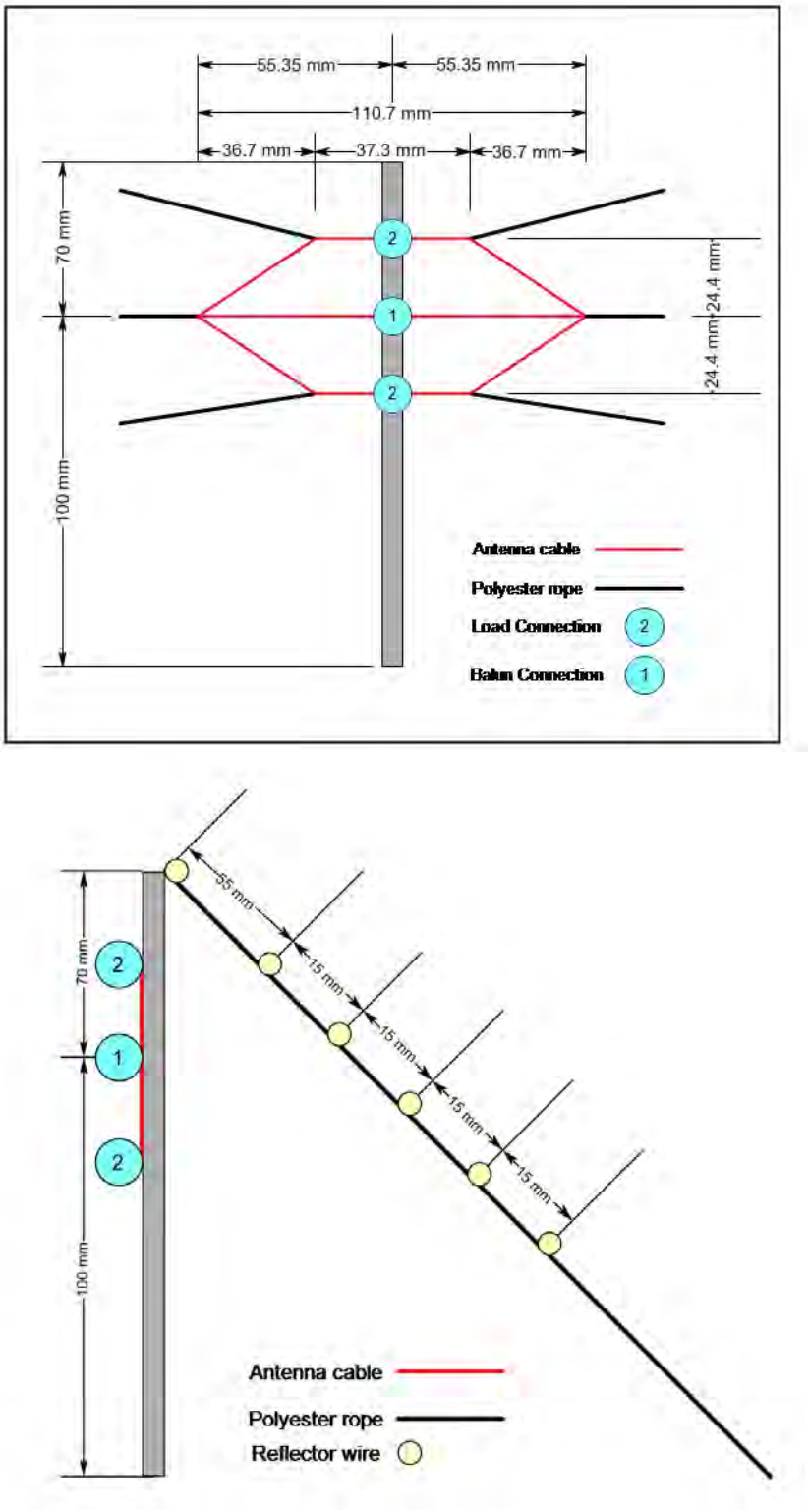

Figure 3.1: (Top) 1:100 Scale antenna front view and (bottom) 1:100 scale antenna side view. This figure shows the change in dimensions from figure 2.8 of the full-scale dimensions to the scale model dimensions.

Figure 3.1 shows the change in physical dimension values for the 1:100 scale model. Since the SuperDARN radar at the SANAE IV base operates primarily at 12.75 MHz the scale model will be built to operate and evaluated as such, using the fundamentals laid out in [24]. The paper gives required dimensions to achieve the maximum possible choking effect, with known sleeve length and coaxial cable diameter or radius.

The scale model used semi-rigid coaxial cable with an outer diameter of ∅3.58 mm and a required sleeve length of 0.25λ equal to 58.82 mm which sets the sleeve balun diameter to ∅5.37 mm.

Due to the manufacturing limitations of Stellenbosch University's Electrical and Electronic workshop and high cost of tight tolerance constraints, all dimensions of the scale model were set to the closest 0.5 mm value. Setting the dimensions of the sleeve balun length to 59 mm and the sleeve balun diameter to 6 mm, shown in figure 3.2. The Engineering drawings can be found in Appendix A.

As can been seen in figure 3.3 the concentricity of the sleeve balun proved difficult to accurately achieve along with the dimensions of the lengths of the TTFD antenna element. Due to this, the simulation model was modified to more accurately represent the real-world model and its flaws.

Figures 3.4 and 3.5 show the real-world models that were tested in Stellenbosch University Electrical and Electronics's anechoic chamber with the single element model in figure 3.4 and the three element model in figure 3.5.

Figures 3.2, 3.4 and 3.5 show the completed real world model. The groundplane is made from a ∅600 mm diameter tin plated mild steel plate, the antenna elements and reflector wires and made from ∅1 mm brass rods, the reflector wires are held in place by a 3 mm perspex sheet angled at 45°, the sleeve balun is made from brass and the antenna element and sleeve balun are held in place by a 50Ω semi-rigid coaxial cable. All Engineering drawings of the individual parts and the complete assembly can be found in Appendix A.

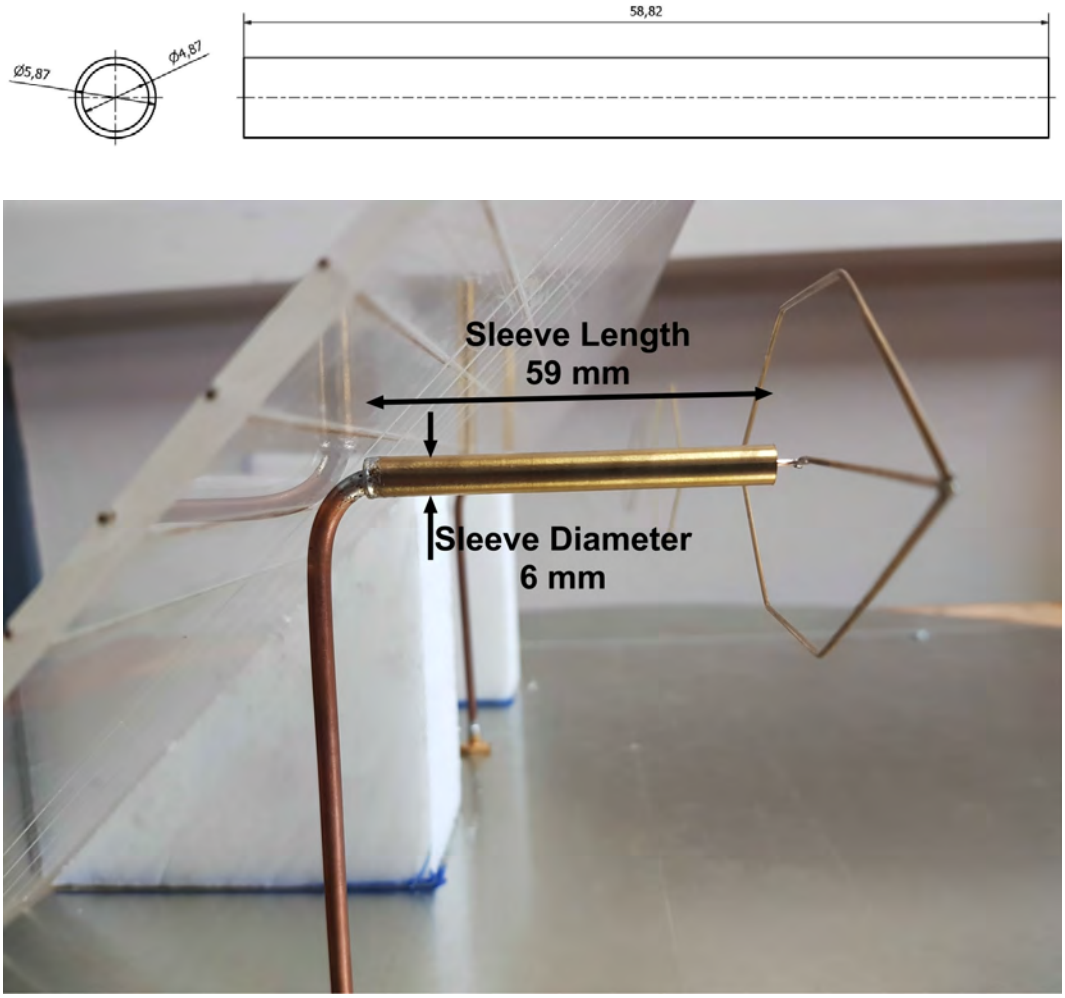

Figure 3.2: Sleeve balun design, (top) engineering drawing and (bottom) real-world scale model. The top figure of the sleeve balun shows the engineering drawing used for the manufacturing of the sleeve balun while the bottom figure shows the real-world completed part.

The sleeve balun deign is shown in figure 3.2, with it's length, inner diameter and outer diameter dimensions given for manufacturing the part. All dimensional tolerances in the engineering drawing of figure 3.2 were set to 0.5 mm.

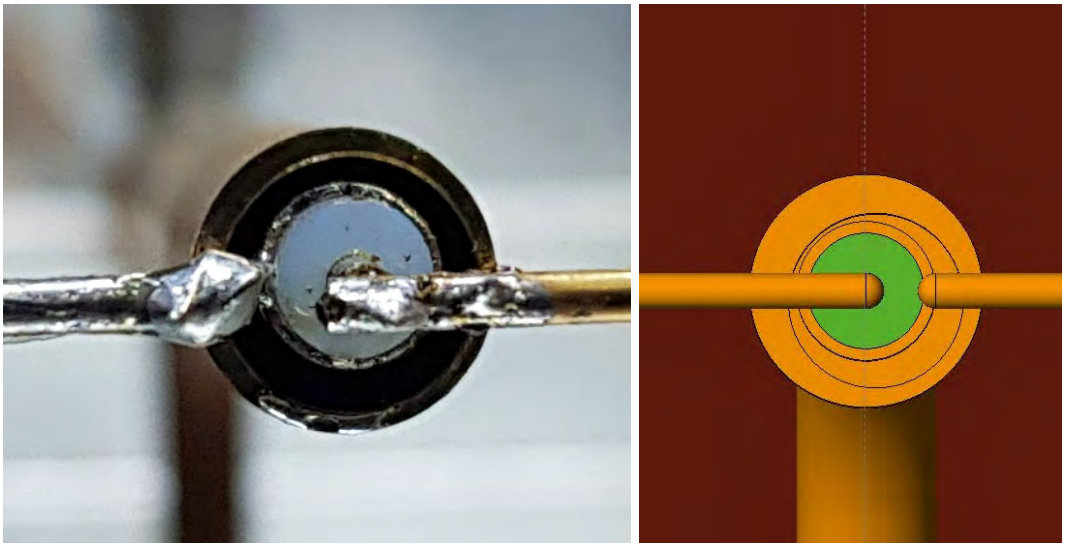

Figure 3.3: (Left) Concentricity misalignment real-world model and (right) concentricity misalignment simulation model. The left figure shows the real-world concentricity misalignment and the right figure shows the concentricity misalignment replicated in the simulation software.

One of the machining errors, namely, the concentricity misalignment is shown in figure 3.3, with the error being incorporated into the simulation model.

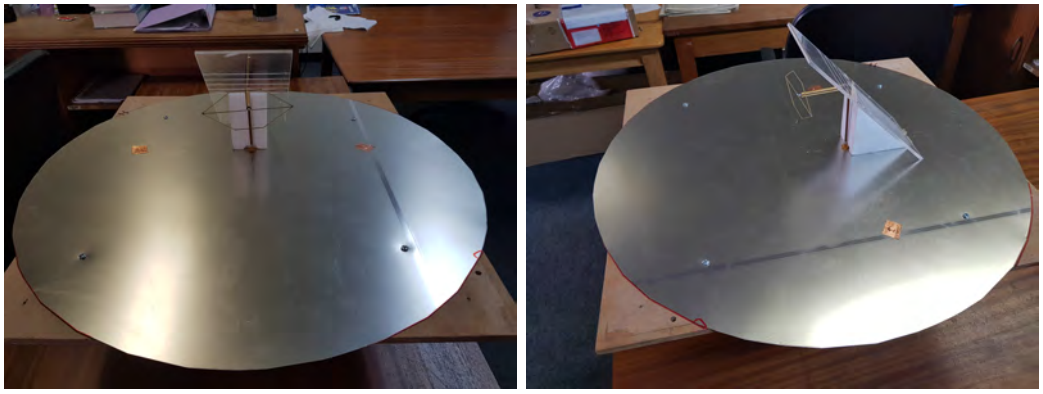

Figure 3.4: (Left) 1:100 Scale single element front view and (right) side view. Completed real-world models of the single element scale model used to measure its antenna characteristics and compare to the simulation results of the same model.

The single element scale model is shown in figure 3.4 with the 90° half corner reflector held in place by a perspex sheet over the tin base.

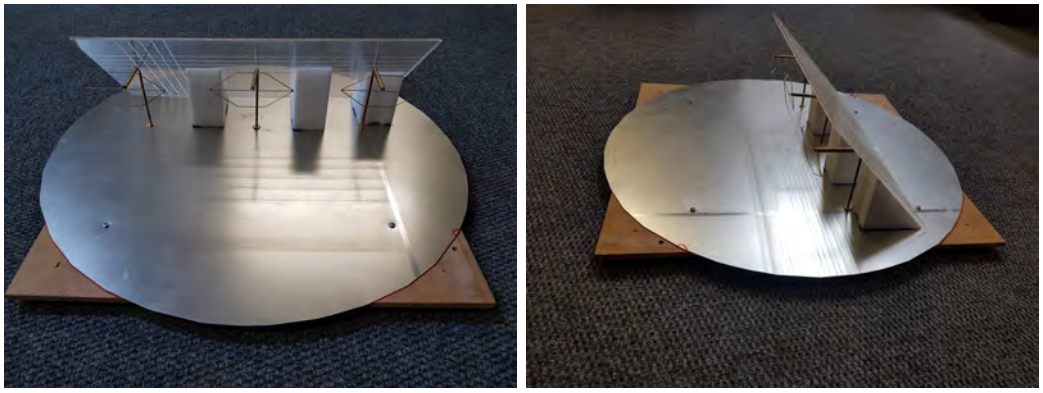

Figure 3.5: (Left) 1:100 scale three element front view and (right) side view. Completed real-world models of the three element scale model used to measure its antenna characteristics and compare to the simulation results of the same model.

Once the scale single element model was measured, the model was altered to have three elements shown in figure 3.5. The elements are space 172 mm apart, antenna elements and sleeve baluns held in place by the semi-rigid coaxial cable and over a tin base.

3.3 Simulation

This section discusses the simulation work done on the 1:100 scale model. Both the single and three element scale model simulations were run in the FEKO EM solver software and their respective results compared to that of the real-world antenna characteristics measured in Stellenbosch University Electrical and Electronics's anechoic chamber.

Originally the scale models were designed in the FEKO software as ideal or perfect models with no manufacturing errors and accurate dimensions, it will be referred to as 'simulated ideal', but after the models were built and simulated it was deemed easier to run the simulations to include these manufacturing errors and imperfect dimensions, it will be referred to as 'simulated machined', rather than trying to quantify their influences on the antenna characteristics of the scale model. The metallic stand on which the models were mounted during the measurements was also included in the FEKO simulation model to further accurately represent the real-world measurement procedure.

The purpose of the scale single element model was to determine whether the element could be correctly characterised through measurement and simulation. While the scale three element model was used to determine whether an array could be correctly characterised. The number of elements in the scale model array (three) was determined by the maximum dimension of an antenna that

can be measured in the anechoic chamber which was 600 mm. With a spacing of 172 mm between the elements, this allowed for three elements to be placed in the base of ∅600 mm, with enough spacing on the outside of the outer elements to still has a semi-infinite ground-plane.

Three scale single element models are shown in figure 3.6, these models are used to outline the reasons for simulating the scale models with a tin base plate as the ground-plane, including the metallic mount used during measurements and including machining errors.

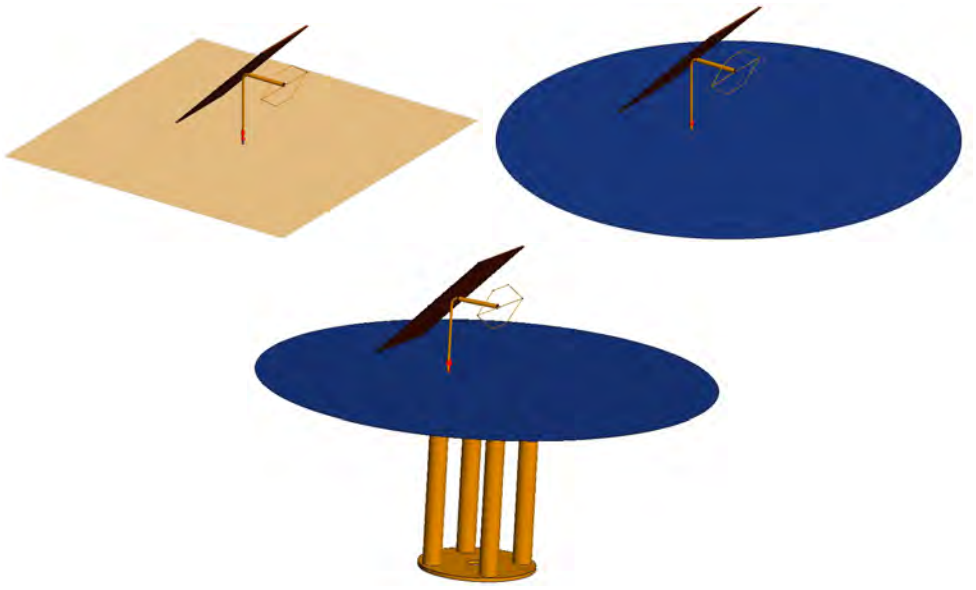

Figure 3.6: Scale single element model with; (top left) infinite PEC ground plane, (top right) circular tin base plate and (bottom) circular tin base plate, metallic mount and machining errors. The three models above were simulated to show the change in directivity caused through each iteration of alterations to the model.

These models were then simulated to show the affects each change had on the directivity of the model, with the plots shown in figure 3.7. The infinite PEC ground plane model is shown by the blue plot, the circular tin base plate model is shown by the red plot and the circular tin base plate, metallic mount and machining errors model is shown by the black plot.

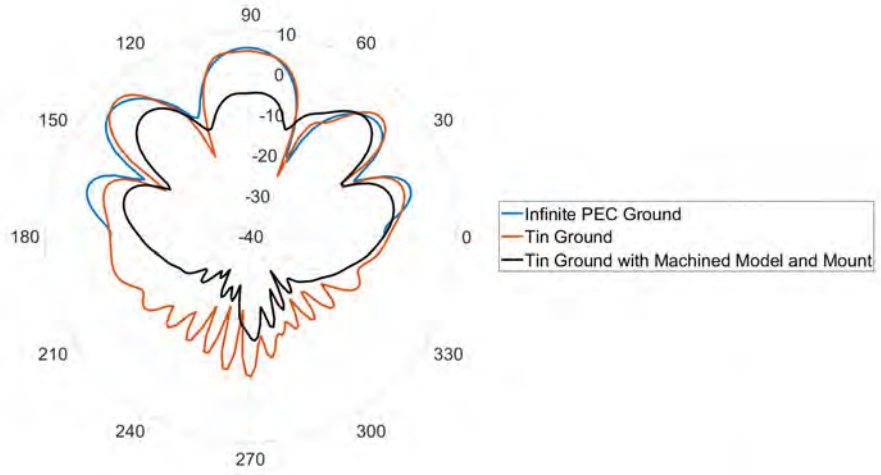

Figure 3.7: Directivity comparison plot, at 3.25 GHz, between the three models shown in figure 3.6. The plots are taken at a plane cut of $\phi = 0°$, with directivity plotted in dB on the radial axis and θ shown on the angular axis.

Considering the infinite PEC ground plane model, plotted in blue, and the circular tin base plate model, plotted in red, the need to define a realistic plane becomes clear. The FEKO simulation software does not calculate the radiation pattern below an infinite ground-plane which would lead to a large discrepancies when the simulated results are compared to the measured results through the RMSE analysis method. It can also be seen that while the general shape of the directivity patterns between these two plots are similar, the directivity levels do differ which would further exacerbate the RMSE analysis method.

When the circular tin base plate model, plotted in red, and the circular tin base plate, metallic mount and machining errors model, plotted in black, are considered the change in the directivity pattern varies significantly. Due to the weight of the scale model a metallic mount was needed to be able to mount the model to the anechoic chamber during measurements. As previously shown in [29] a metallic mount does influence the overall results during measurements which are further influenced by the machining errors of in the model.

Figure 3.8 shows the comparison in directivity pattern of the ideal model, plotted in red, versus the real-world measured model, plotted in blue. The ideal model is the same as the circular tin base plate model above with no machining errors and no metallic stand.

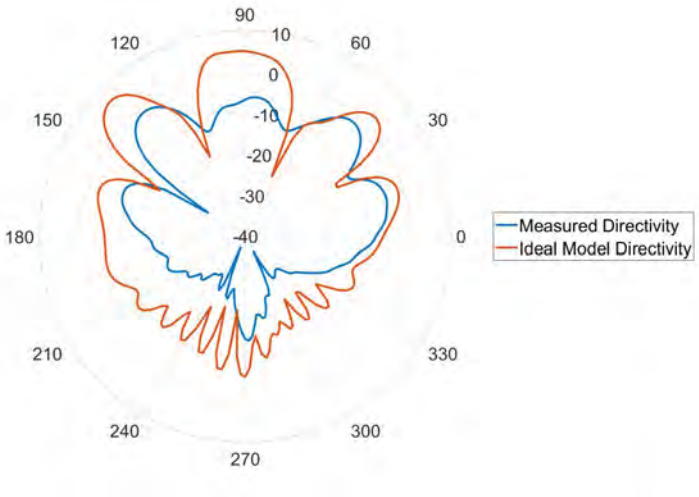

Figure 3.8: Directivity comparison plot, at 3.25 GHz, of the scale single element model between the measured results and the simulated results of an ideal model. The plots are taken at a plane cut of $\phi = 0°$, with directivity plotted in dB on the radial axis and θ shown on the angular axis.

When considering figure 3.8 the affects that machining errors and metallic stand have on the directivity carry over to the real-world measured model. For this reason the metallic stand and the machining errors are included in the simulation of the scale models to reduce the RMSE difference between the simulation and measured results.

3.3.1 Scale Single Element Model Simulation

The set-up of the simulation of the scale single element model are outlined in this section with table 3.2 showing the summary of unknowns of the model and figures 3.9 and 3.10 showing the simulation model in the FEKO EM software.

Table 3.2: 1:100 Scale single element model simulation set-up.

Discretised Model	**Solver Settings**
Source	Waveguide port
Solver	MoM
RAM used	5.94 GB
Number of metallic triangles	22 399
Number of dielectric triangles	91
Number of metallic unknowns	36 743
Number of dielectric unknowns	122
Number of unknown basis functions for MoM	36 987

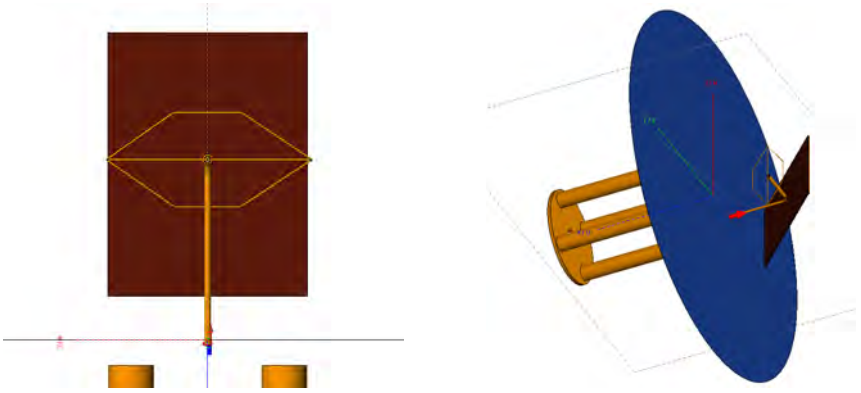

Figure 3.9: 1:100 Scale single element model simulation with stand. Scale single element model that was simulated in the FEKO software along with the metallic stand that was used to mount the model in the anechoic chamber during measurements.

From the figure 3.9 the antenna element can be seen in front of the maroon perspex sheet which holds the 6 reflector wires in place. The image on the right is an ISO view of the simulation model clearly showing the metallic stand underneath the model and the blue tin base, with waveguide port used to excite the coaxial cable holding the element and sleeve balun in place.

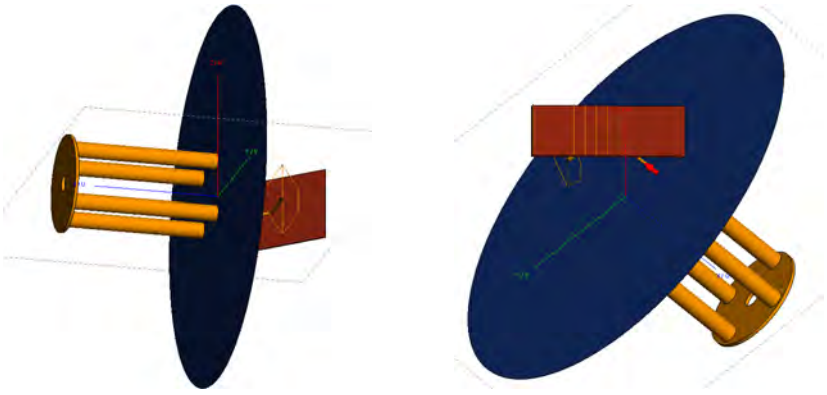

Figure 3.10: Additional images of the 1:100 scale single element model simulation with stand. These images aim to provide a clearer view of the scale single element model that was simulated in the FEKO software.

Considering figure 3.10 the metallic stand and the placement of the reflector wires are shown more clearly with their respective positions in relation to the blue tin base plate.

3.3.2 Scale Single Element Model Results Comparison

The results between the measured versus simulated scale single element model are discussed in this section. With figures 3.11 and 3.12 showing the antenna

under test (AUT) in the anechoic chamber during measurements.

Figure 3.11: Photographs of the 1:100 scale single element model under test in the anechoic chamber. The pictures show the AUT with the connection to the measurement apparatus in the left photograph and the antenna probe with the AUT measurement set-up from the back in the photograph on the right.

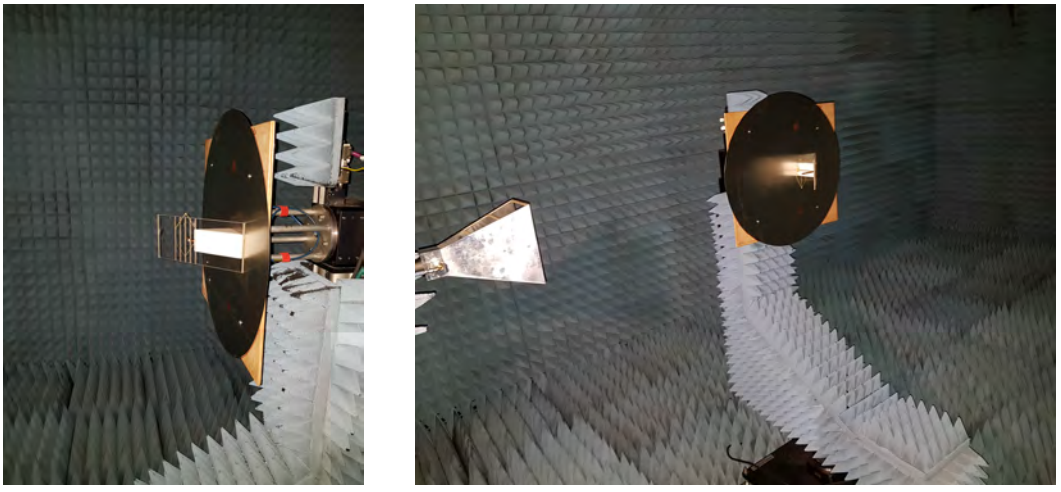

Figure 3.12: 1:100 Scale single element model under test in the anechoic chamber. The photograph on the left clearly shows the reflector wires on the AUT, while the photograph on the right is of the measurement set-up of the probe antenna and AUT from the front.

Figures 3.11 and 3.12 shown the scale single element model test set-up in the anechoic chamber from the back and from the front respectively. The model can be seen mounted to the mounting point of the anechoic chamber and connected to the measurement apparatus via the blue coaxial cable.

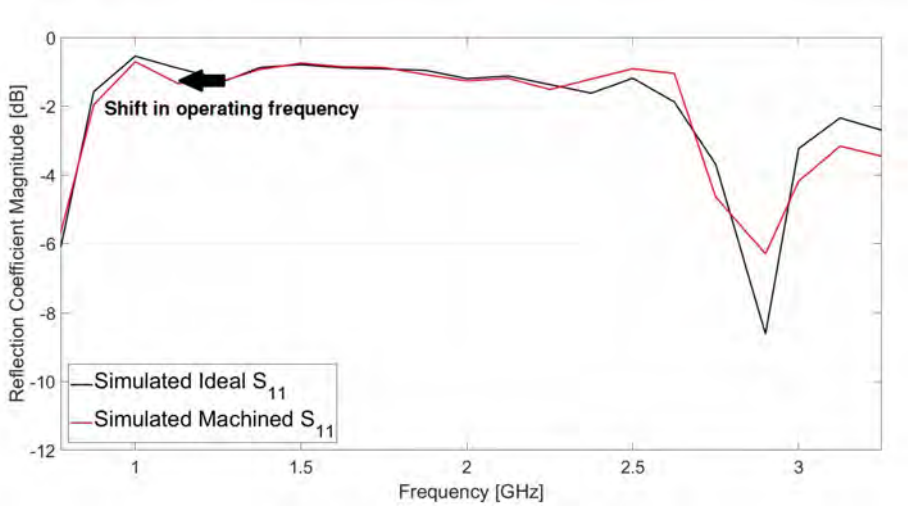

Figure 3.13: 1:100 Scale single element simulated ideal S_{11} (black) versus simulated machined S_{11} (red). This figure shows the shift in operating frequency from 1.275 GHz down to 1.129 GHz when the manufacturing errors are included in the simulation model. 21 Frequency points were simulated and plotted here, to match the 21 frequency points which the real-world model was measured at.

Shown in figure 3.13 is the comparison of the S_{11} between the simulations of the ideal model (black) versus the machined model (red). The manufacturing errors shift the operating frequency down from 1.275 GHz to 1.129 GHz. This coincides with the measured S_{11} shown in figure 3.14 as the blue line, where the measured operating frequency has also shifted down to 1.129 GHz in the real-world model.

Figure 3.14 shows the plot of the measured S_{11} in blue versus the simulated S_{11} in red which include all machining error and incorrect dimensions which were present on the real-world model over a frequency range of 0.776 GHz - 3.25 GHz.

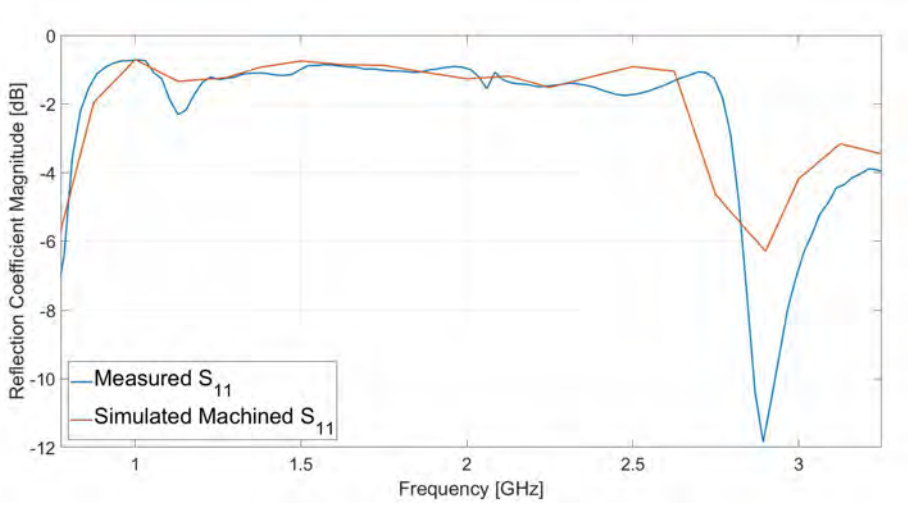

Figure 3.14: 1:100 Scale single element measured S_{11} (blue) versus simulated machined S_{11} (red). This figure shows that the shift in operating frequency from 1.275 GHz down to 1.129 GHz is also seen when the real-world model was measured and further confirms this shift in the simulation of the machined model. 21 Frequency points were measured and plotted here against the 21 frequency points which were simulated.

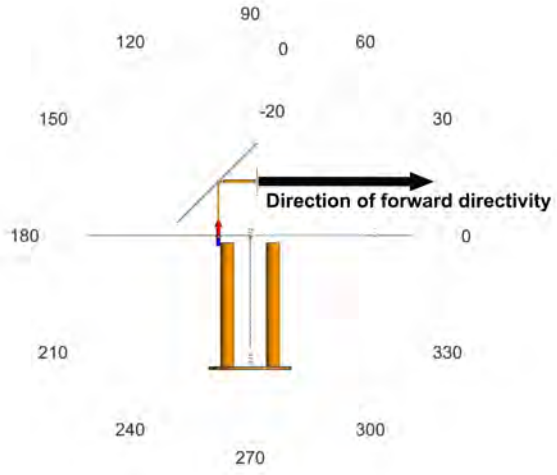

Figure 3.15: Antenna orientation in respect to the polar plot of the results. The figure above shows how the scale model is orientated when looking at the results on the polar plot.

The orientation of the scale model in respect to the polar plots to follow is shown in figure 3.15, with the front of the antenna point towards the 0° direction. With θ being on the angular axis of the polar plot, directivity on the radial axis in dB and the plane cut taken at the $\phi = 0°$.

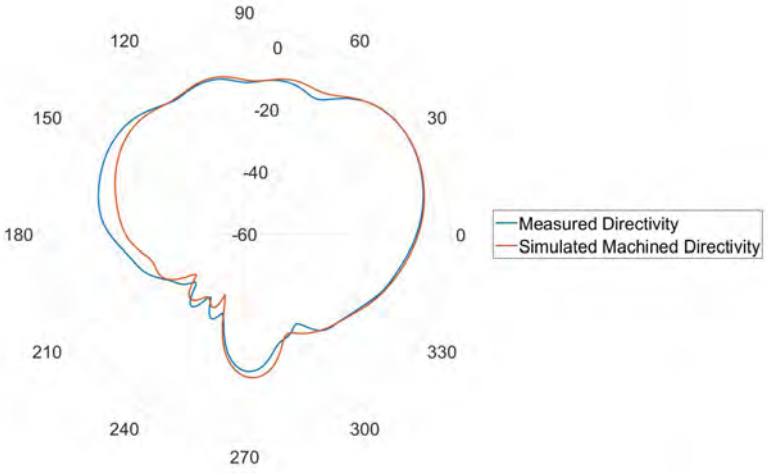

Figure 3.16: 1:100 Scale single element measured far-field directivity (blue) versus simulated machined far-field directivity (red) at 1.625 GHz. The θ angles are on the angular axis of the polar plot and directivity on the radial axis in dB.

The comparison between the far-field directivity of the measured (blue) versus the simulated machined (red) results is shown in figure 3.16 at 1.625 GHz, with the antenna pointing to the right of the polar graph in the direction of 0°. The biggest difference in the results can be seen between θ = 150° - 270° where the reflector and mounting bracket are located.

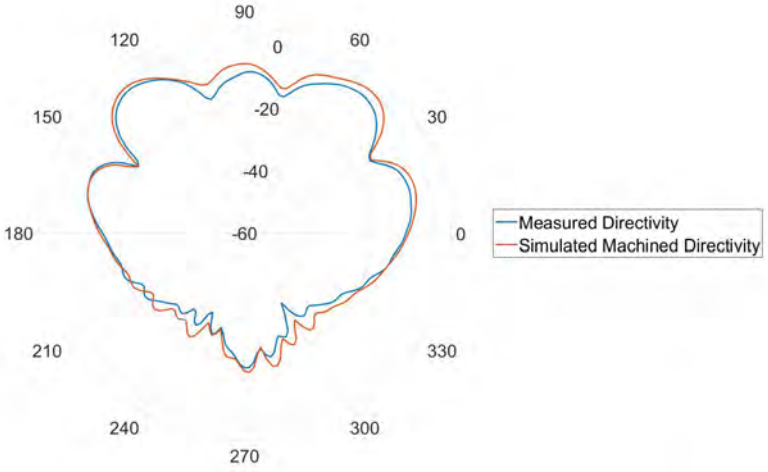

Figure 3.17: 1:100 Scale single element measured far-field directivity (blue) versus simulated machined far-field directivity (red) at 3.125 GHz. The directivity is on the radial axis in dB and θ angles on the angular axis of the polar plot.

Figure 3.17 shows the comparison of the far-field directivity between the mea-

sured (blue) versus the simulated machined (red) results at 3.125 GHz, with the antenna pointing to the right of the polar graph in the direction of 0°. Here the greatest difference is seen around $\theta = 90°$ directly above the top wire of the reflector.

The comparison at 3.250 GHz between the far-field directivity of the measured (blue) versus the simulated machined (red) results, with the antenna pointing to the right of the polar graph in the direction of 0° are is shown in figure 3.18. The largest difference is around $\theta = 270°$ where the model is mounted to the anechoic chamber via the metallic stand.

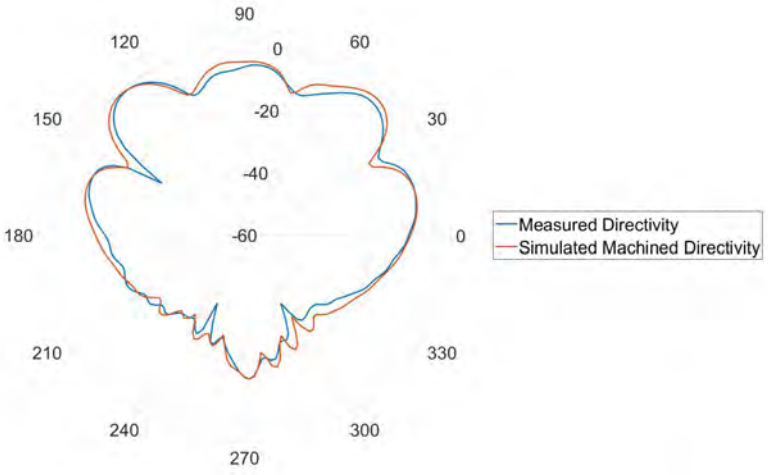

Figure 3.18: 1:100 Scale single element measured far-field directivity (blue) versus simulated machined far-field directivity (red) at 3.250 GHz. The θ angles are on the angular axis of the polar plot and directivity on the radial axis in dB.

Considering figures 3.16 - 3.18 the comparison between the far-field directivity of the measured (blue) versus the simulated machined (red) results are similar. Figure 3.14 shows the expected S_{11} achieved through the simulation of the machined model has some differences to the results of the S_{11} that were measured from the real-world model. This in conjunction with the machining errors that cannot be perfectly matched in the simulation model, ensuring the antenna element is perpendicular to the ground-plane at all times during the measurement and chamber factors. By converting the results to linear values the RMSE analysis method [25] can be used to quantify the comparison between the simulated versus measured results, the comparisons can then be converted back into dB values. When comparing the results, the FEKO simulations have an average difference of 1.06 dB from the measured results of the forward beam total directivity level and an average of 2.1 dB in difference for the reverse beam and below the ground-plane total directivity level. Provid-

ing an overall difference in total directivity level of 1.4 dB for the scale single element model.

3.3.3 Scale Three Element Model Simulation

This section discusses the simulation of the 1:100 scale three element model and its set-up. Both the simulation and measurement procedures were run in the same way, namely, in the first set-up, the antenna element 1 was excited with a source while antenna elements 2 and 3 were loaded with a 50Ω load. In the second set-up antenna element 2 was excited with a source while antenna elements 1 and 3 were loaded with a 50Ω load. The final set-up excited antenna element 3 with a source while antenna elements 1 and 2 were loaded with a 50Ω load. With figures 3.19 and 3.20 clearly showing the FEKO simulation model. The purpose of alternating the source and load connections between the three elements was to have a scale measurement which resembled the SuperDARN radar's set-up and to be able to measure directivity with one port.

Table 3.3: 1:100 Scale three element model simulation set-up.

Discretised Model	**Solver Settings**
Source	Edge port
Solver	MoM
RAM used	20.992 GB
Number of metallic triangles	43 241
Number of dielectric triangles	0
Number of metallic unknowns	64 617
Number of dielectric unknowns	0
Number of unknown basis functions for MoM	64 617

Figure 3.19 shows the element configuration in the simulation model of the three element scale model with the reflector wires held in place by the maroon perspex sheet over all three elements. Each element is excited using a edge port placed at the end of the coaxial cable.

The metallic stand in relation to the blue tin base is shown in figure 3.20, which was used to mount the model to the anechoic chamber during measurements.

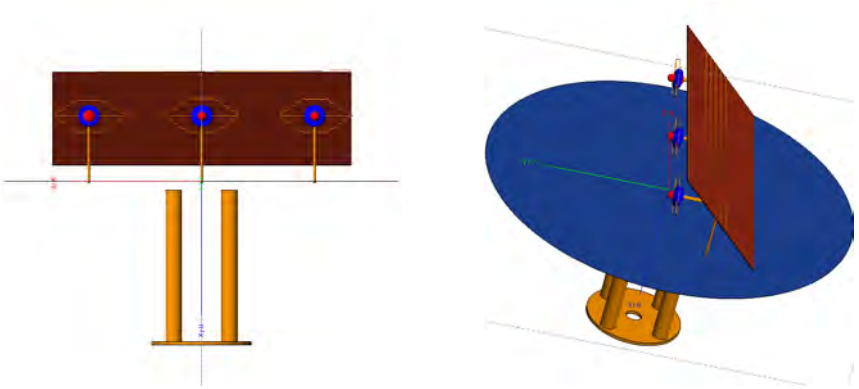

Figure 3.19: 1:100 Scale three element model simulation with stand. The left image distinctly shows the three elements with their edge port excitation sources, with the maroon perpex sheet that holds the reflector wires in place behind the elements. The ISO image on the right provides a clearer view of the 6 reflector wire placements.

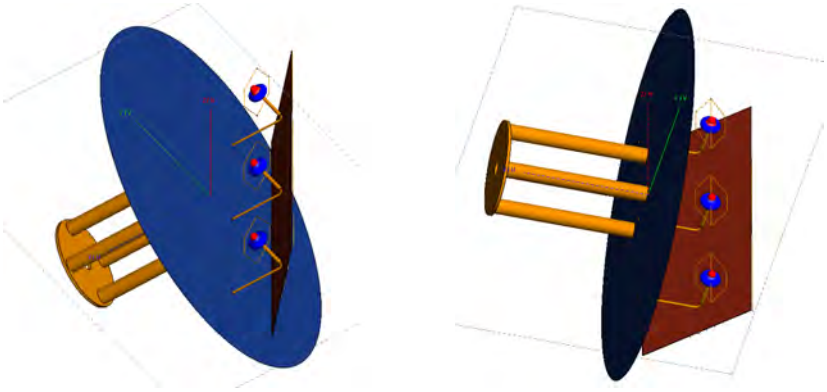

Figure 3.20: Additional figure of the 1:100 scale three element model simulation. These images clearly show the location of the edge ports at the ends of the coaxial cables, along with the blue tin base and metallic stand.

3.3.4 Scale Three Element Model Results Comparison

Figures 3.21 and 3.22 clearly shows the AUT in the anechoic chamber. With figure 3.23 showing the S_{11} of the measured real-world model of each element with the solid blue, black and red plots in comparison to their respective simulated machined S_{11} values the dashed blue, black and red plots. Again some discrepancies between the S_{11} from the simulation of the machined model and what was achieved when the measurements were taken. The results of the comparison data are shown in figures 3.25 - 3.33, with the machining errors causing an average difference of 1.56 dB between the simulated and measured results of the forward beam total directivity level and an average difference of 2.6 dB for the reverse beam and below the ground-plane total directivity level. Therefore, it can be said that the Altair Hyperworks FEKO EM software solver

has an average difference of 2.09 dB for the overall total directivity level for the scale three element model. These comparisons were determined using the RMSE method by first converting the results to determine the comparisons and then converting them back into dB values [25].

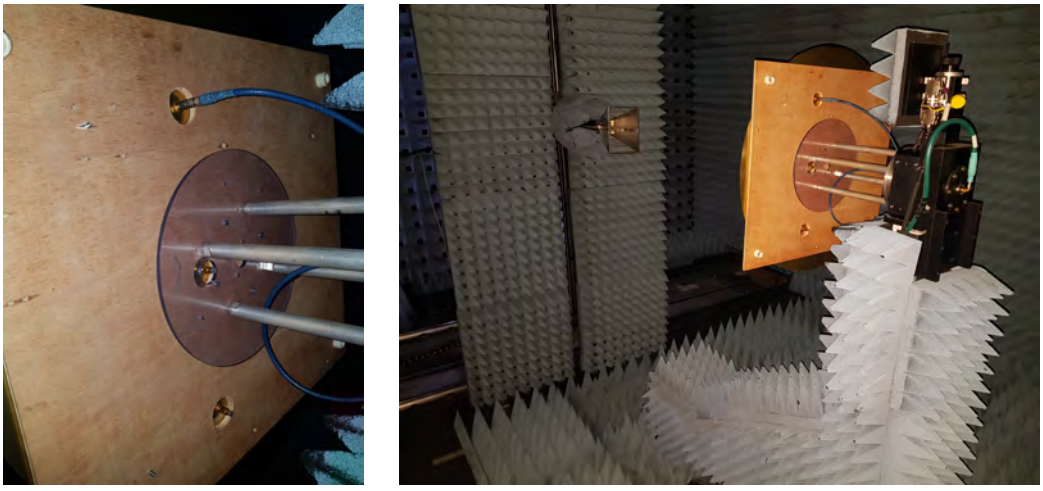

Figure 3.21: 1:100 Scale three element model under test in Stellenbosch University Electrical and Electronics's anechoic chamber. The photographs show the scale single element model under test, the connection to the measurement apparatus for set-up 1 and the antenna probe.

The photographs in figure 3.21 show the connections of the source, in this case at the top, and the loads underneath the model are shown and the measurement set-up with the probe antenna and the AUT from the back.

Figure 3.22 shows the measurement set-up of the three scale element model in the anechoic chamber from the front.

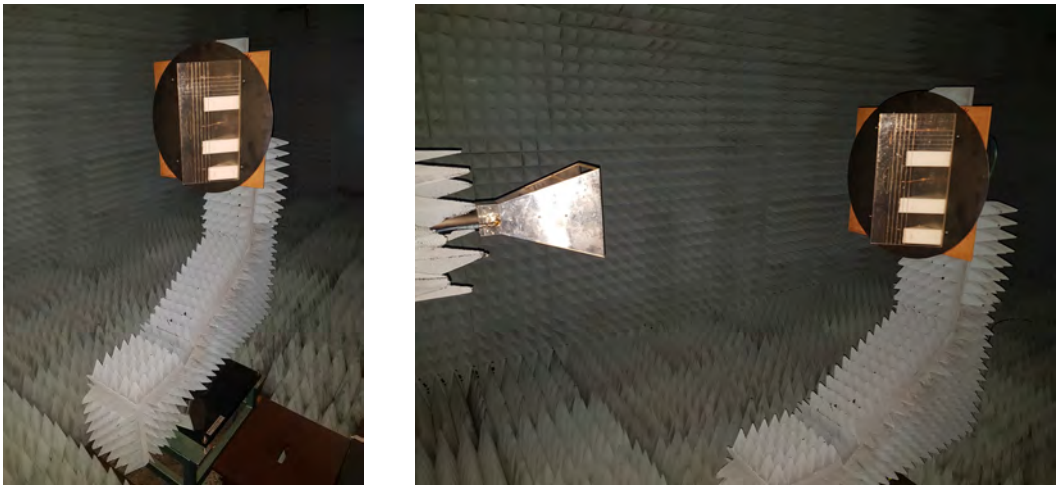

Figure 3.22: Photographs of the 1:100 scale three element model under test in Stellenbosch University Electrical and Electronics's anechoic chamber. The photograph on the left more clearly shows the reflector wires on the AUT, while the photograph on the right shows the measurement set-up from the front.

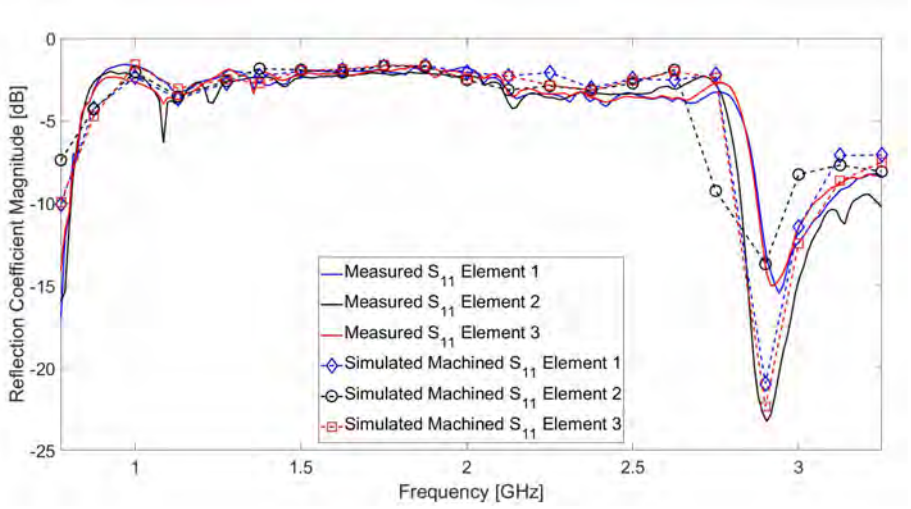

Figure 3.23: 1:100 Scale three element model measured S_{11} element 1 (solid blue), measured S_{11} element 2 (solid black), measured S_{11} element 3 (solid red) versus simulated machined S_{11} element 1 (dashed blue), simulated machined S_{11} element 2 (dashed black) and simulated machined S_{11} element 3 (dashed red).

Each measured S_{11} results is shown in comparison to its respective simulated S_{11} in figure 3.23 over a frequency range of 0.776 GHz - 3.25 GHz with 21 frequency points plotted.
Figure 3.24 shows how the three element model is orientated with respects to the polar plot, the front of the antenna point towards the 0° direction. With θ being on the angular axis of the polar plot, directivity on the radial axis in

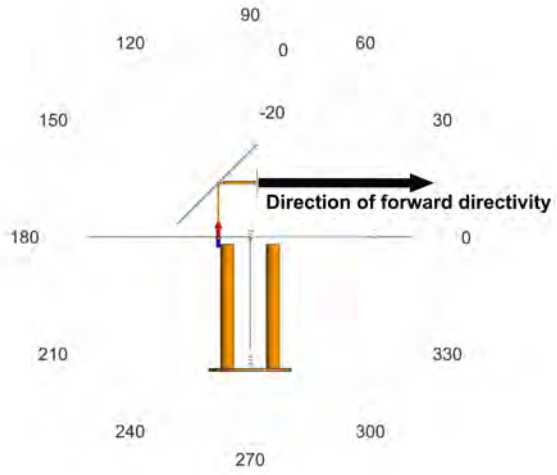

Figure 3.24: Antenna orientation in respect to the polar plot of the results for the scale three element model. The orientation of the scale model in respect to the polar plot axis is shown in this figure.

dB and the plane cut taken at the $\phi = 0°$

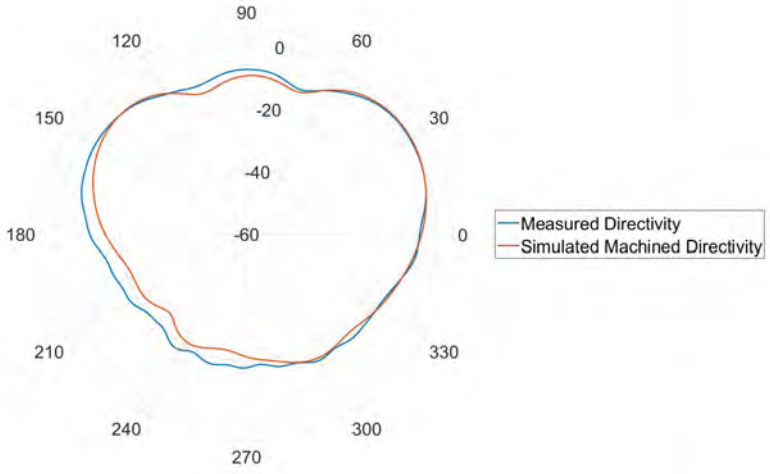

Figure 3.25: 1:100 Scale three element measured far-field directivity (blue) versus simulated machined far-field directivity (red) at 1.625 GHz, with set-up 1. Directivity, in dB, is on the radial axis while θ is on the angular axis of the polar plot.

The comparison between the far-field directivity of set-up 1's measured (blue) versus the simulated machined (red) results is shown in figure 3.25 at 1.625 GHz, with the antenna pointing to the right of the polar graph in the direction of 0°. Here the largest differences are between θ = 90° - 270° where the reflector and metallic stand are located.

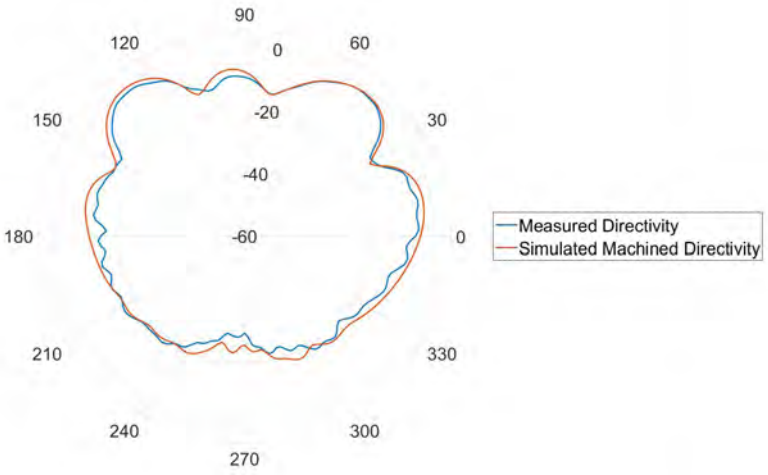

Figure 3.26: 1:100 Scale three element measured far-field directivity (blue) versus simulated machined far-field directivity (red) at 3.125 GHz, with set-up 1. θ is on the angular axis and directivity on the radial axis, in dB, of the polar plot.

Figure 3.26 shows the comparison between the far-field directivity of set-up 1's measured (blue) versus the simulated machined (red) results at 3.125 GHz, with the antenna pointing to the right of the polar graph in the direction of 0°. The greatest difference in results is around θ = 180° - 300° where the model is mounted to the anechoic chamber.

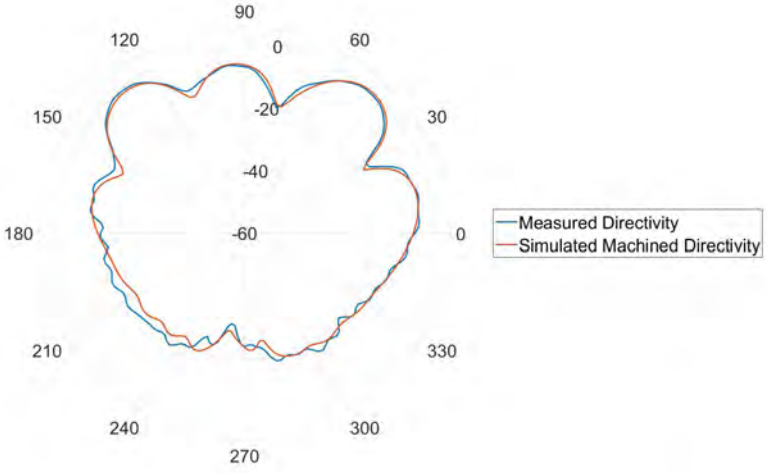

Figure 3.27: 1:100 Scale three element measured far-field directivity (blue) versus simulated machined far-field directivity (red) at 3.250 GHz, with set-up 1. Directivity, in dB, is on the radial axis while θ is on the angular axis of the polar plot.

The comparison at 3.250 GHz between the far-field directivity of set-up 1's measured (blue) versus the simulated machined (red) results, with the antenna pointing to the right of the polar graph in the direction of 0° are is shown in figure 3.27. The largest difference is around θ = 200° - 240° where the model is mounted to the anechoic chamber via the metallic stand.

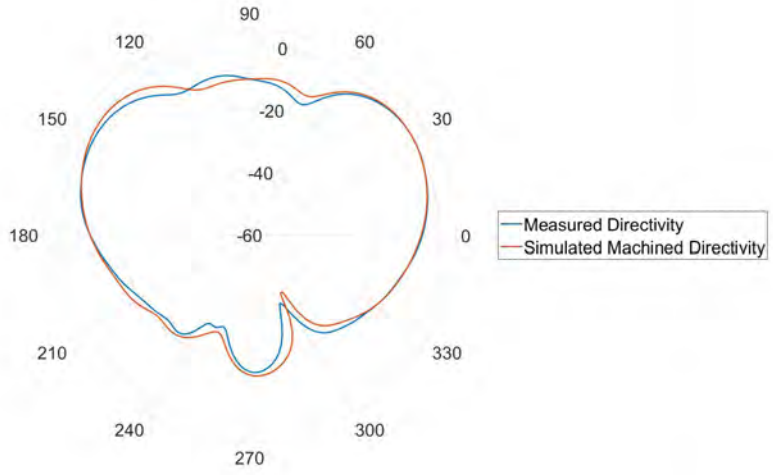

Figure 3.28: 1:100 Scale three element measured far-field directivity (blue) versus simulated machined far-field directivity (red) at 1.625 GHz, with set-up 2. Directivity, in dB, is on the radial axis while θ is on the angular axis of the polar plot.

The comparison between the far-field directivity of set-up 2's measured (blue) versus the simulated machined (red) results is shown in figure 3.28 at 1.625 GHz, with the antenna pointing to the right of the polar graph in the direction of 0°. The biggest difference is around θ = 300° where the model is mounted on the metallic stand.

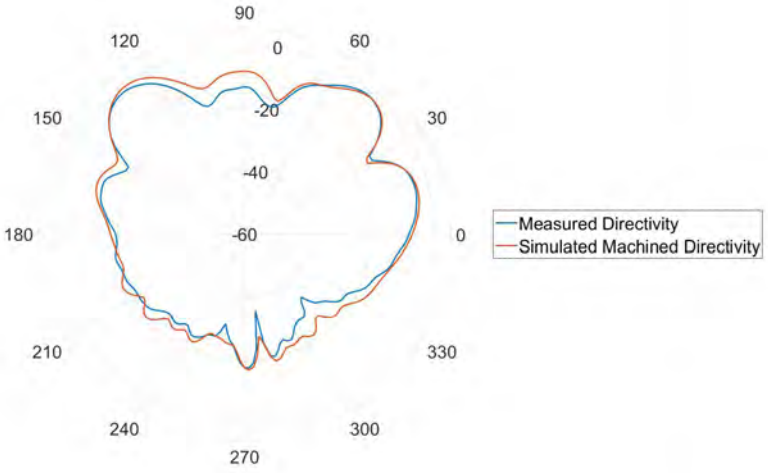

Figure 3.29: 1:100 Scale three element measured far-field directivity (blue) versus simulated machined far-field directivity (red) at 3.125 GHz, with set-up 2. θ is on the angular axis and directivity on the radial axis, in dB, of the polar plot.

Figure 3.29 shows the comparison between the far-field directivity of set-up 2's measured (blue) versus the simulated machined (red) results at 3.125 GHz, with the antenna pointing to the right of the polar graph in the direction of 0°. The greatest difference in results is at $\theta = 90°$ where the top reflector wire is located and $\theta = 300°$ where the model is mounted to the anechoic chamber.

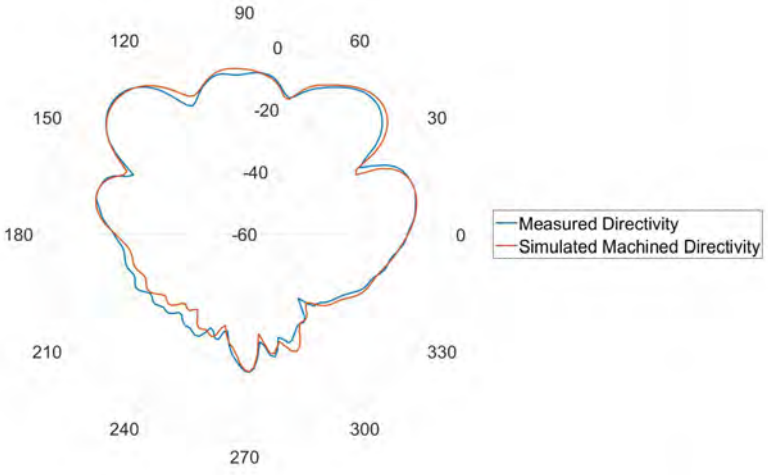

Figure 3.30: 1:100 Scale three element measured far-field directivity (blue) versus simulated machined far-field directivity (red) at 3.250 GHz, with set-up 2. Directivity, in dB, is on the radial axis while θ is on the angular axis of the polar plot.

The comparison at 3.250 GHz between the far-field directivity of set-up 2's measured (blue) versus the simulated machined (red) results, with the antenna pointing to the right of the polar graph in the direction of 0° are is shown in figure 3.30. The largest difference is about $\theta = 240°$ where the model is mounted to the anechoic chamber via the metallic stand.

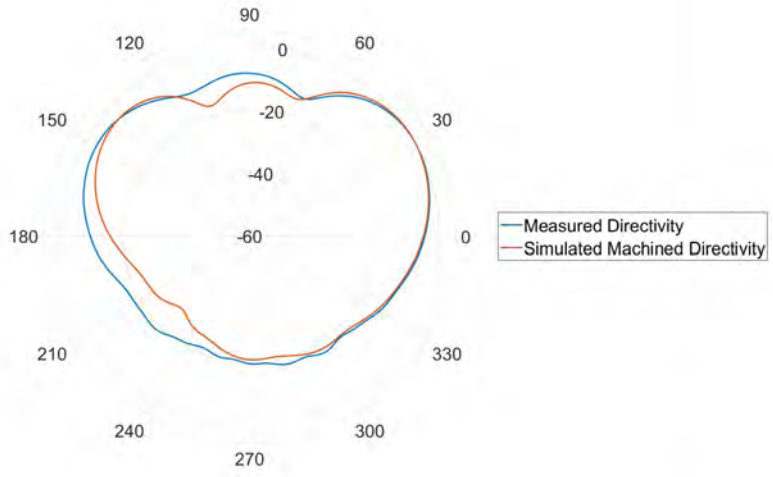

Figure 3.31: 1:100 Scale three element measured far-field directivity (blue) versus simulated machined far-field directivity (red) at 1.625 GHz, with set-up 3. θ is on the angular axis and directivity on the radial axis, in dB, of the polar plot.

The comparison between the far-field directivity of set-up 3's measured (blue) versus the simulated machined (red) results is shown in figure 3.31 at 1.625 GHz, with the antenna pointing to the right of the polar graph in the direction of 0°. The biggest differences are between $\theta = 90°$ - 270° where the reflector and metallic stand are located.

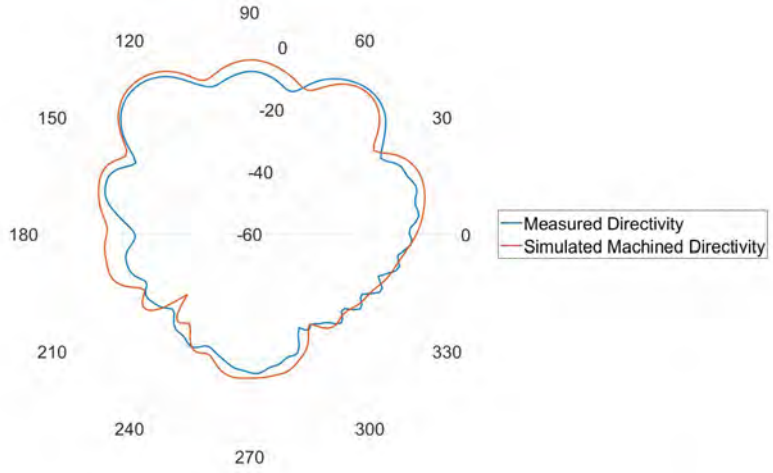

Figure 3.32: 1:100 Scale three element measured far-field directivity (blue) versus simulated machined far-field directivity (red) at 3.125 GHz, with set-up 3. Directivity, in dB, is on the radial axis while θ is on the angular axis of the polar plot.

Figure 3.32 shows the comparison between the far-field directivity of set-up 3's measured (blue) versus the simulated machined (red) results at 3.125 GHz, with the antenna pointing to the right of the polar graph in the direction of 0°. The greatest difference in results is at $\theta = 180°$ where the model is mounted to the anechoic chamber.

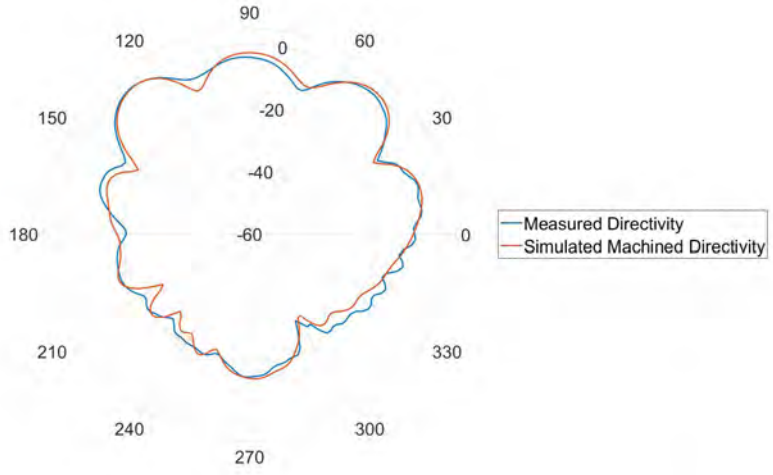

Figure 3.33: 1:100 Scale three element measured far-field directivity (blue) versus simulated machined far-field directivity (red) at 3.250 GHz, with set-up 3. θ is on the angular axis and directivity on the radial axis, in dB, of the polar plot.

The comparison between the far-field directivity of set-up 3's measured (blue)

versus the simulated machined (red) results is shown in figure 3.33 at 3.25 GHz, with the antenna pointing to the right of the polar graph in the direction of 0°. Here the biggest differences are at $\theta = 330°$ metallic stand is located.

Table 3.4: Summary of RMSE differences between simulated and measured results.

Model	Forward beam difference	Reverse beam difference	Overall difference
Scale single element	1.06 dB	2.1 dB	1.4 dB
Scale three element Set-up 1	1.98 dB	2.72 dB	1.99 dB
Scale three element Set-up 2	2.01 dB	2.56 dB	2.45 dB
Scale three element Set-up 3	1.85 dB	2.87 dB	2.09 dB

Through the use of two scale models and Altair Hyperworks FEKO EM software solver the differences between the measured and simulated results were quantified through the RMSE method with the summary of results shown in table 3.4.

3.4 Discussion

The purpose of the work done in this chapter was to verify scale modelling to provide confidence in the Altair Hyperworks FEKO software. This method would then determine whether or no the FEKO results of the full-scale model would be accurate. The chapter first outlined the design and manufacture of the 1:100 scale single and three element models. Followed by the simulation set-up and procedure for the 1:100 scale single element model and compared the real-world measured to the simulated machined results, namely looking at the comparisons between the S_{11} and far-field directivity. The process was then repeated for that of the 1:100 scale three element model.

The manufacturing errors were incorporated into the simulation models to more accurately represent the real-world model being tested. In the anechoic chamber the antenna under test (AUT) is slightly offset from the centre of measurement and although in the initial measurement set-up of setting the centre point of measurement for the probe antenna, along with mounting the AUT on a stand to get the AUT as close to the centre point as possible, this adds further discrepancies between the measured versus simulated results.

With the half corner reflector included in the scale model design, less energy is directed to the back of the antenna which would account for the differences in the measured versus simulated results between $\theta = 90°$ - $180°$, in the $\phi = 0°$ plane. Between $\theta = 180°$ - $360°$, in the $\phi = 0°$ plane, this was where the model was mounted with the metallic stand to the anechoic chamber mount with the absorber foam which creates even more uncertainty when the measurement antenna probe between these two angles. Where the simulated matching (S_{11}) is poor compared to the measured S_{11} input energy is sent back through the input cables, as seen at 2.9 GHz in figures 3.14 and 3.23 where the differences in S_{11} are 5.547 dB and 9.55 dB respectively. Between $\theta = 0°$ - $90°$, in the $\phi = 0°$ plane, is where the directivity of the forward beam is located and between these two angles, the simulation results closely match those of the measured results. With Altair Hyperworks FEKO total directivity level results having an average overall difference of 3 dB when compared to the measured total directivity level for the scale single element model and average overall difference of 3.7 dB for the directivity level of the scale three element model, when using the RMSE method. Stellenbosch's anechoic chamber has a measurement uncertainty of 2 dB - 4 dB between a frequency range of 0.75 GHz - 3 GHz [30] which were also taken into consideration. The summary of differences tabulated in table 3.4.

3.5 Conclusion

This chapter has discussed the method used to determine whether or not the FEKO EM solver software can be used to evaluate the full-scale SuperDARN radar model with confidence, through the use of two 1:100 scale models. Although there are some discrepancies between the measured versus simulated results, the RMSE values are all below 3 dB, lying well wihtin the confidence level of 8-9 dB described at the beginning of the chapter. It can be stated that the FEKO simulation software can be used with confidence to evaluate the full-scale SuperDARN radar antenna array.

Chapter 4

Simulation of Full-Scale Model

4.1 Introduction

In this chapter, the full-scale model will be evaluated using the FEKO EM solver software. The purpose of this chapter is to correctly characterise the directivity of the full-scale SuperDARN radar antenna array so that the front-to-back ratio can be improved, as it has been shown that if the backwards radiation has considerable power it will complicate data analysis as backscatter signals are received from unwanted paths [5]. For TTFD antennas with a full corner reflector it is expected to see a front-to-back ratio of around 10 - 12 dB [18]. The SuperDARN radar located at the SANAE IV base was originally designed in FEKO by only modelling the radar over an infinite PEC ground plane, which is used as the starting point for the simulations. The chapter will start off by looking at the installed radar set-up at the SANAE IV base shown in figure 2.8, which shows the complete view of the radar, and figure 4.1, which shows only the element of the radar, with the 90° half corner reflector. After that, various adjustments are made to the corner reflector, namely, (1) reflector's antenna cables connected behind the elements, (2) behind the elements and in-between elements, (3) behind the elements and in-between elements and then in-between again and (4) connected behind the elements with equal wire spacing in the reflector. All these variations are compared between the model over an infinite PEC ground-plane and an infinite ice and granite ground-plane. This process is then mimicked for a full-scale SuperDARN radar with a 90° full corner reflector. Appendix B contains the results of a 90° ideal half and full plate corner reflector of various dimensions, as well as 60° and 30° full corner reflectors with antenna cables connected behind the elements. The reason for these variations are to see which practically implementable solutions will improve the level of forward reflection. Higher density mesh compared to wavelength (λ=23.59 m at 12.75 MHz) should improve the reflection in theory. For all the simulations run in this chapter the first column of phase values in Appendix C were used to evaluate the model.

4.2 Simulation Set-ups

This section will look at the simulation set-up for the various full-scale models of the SuperDARN radar. The element for each antenna shown in figure 4.1 which uses wire ports for the excitation signal, using the phase matrix shown in Appendix C [18], and loads. The 16-elements that make up the front array are excited in this way while the 4-elements that make up the back array are switched off as they are used as receivers. Figure 4.2 shows the side views of the different 90° half and full corner reflector set-ups, while the isometric views are shown in figures 4.3 - 4.7 over the two different ground-planes.

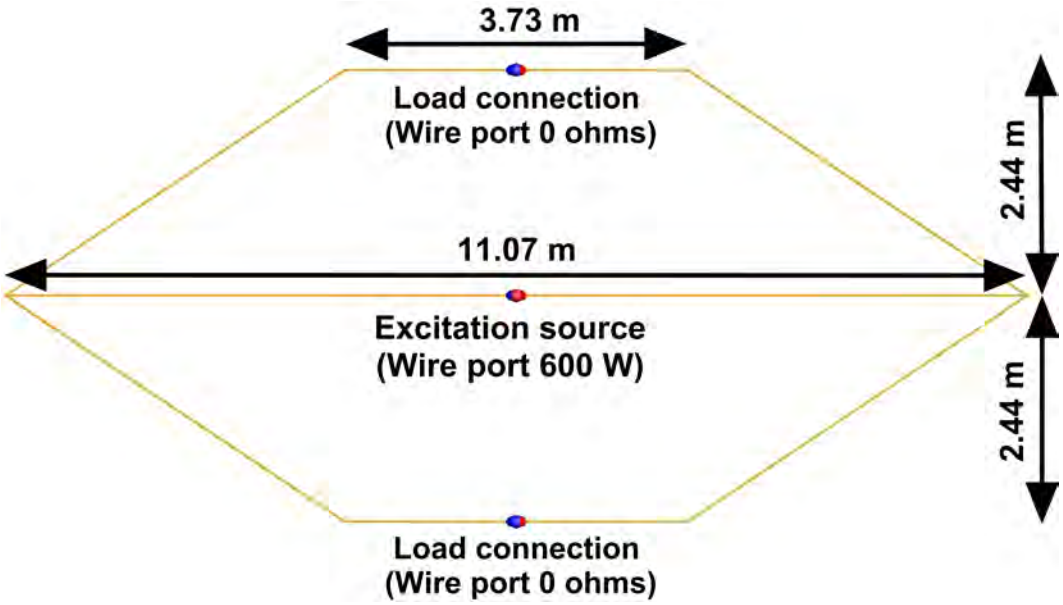

Figure 4.1: Element set-up for each antenna in the full-scale model. This figure shows the set-up configuration of the individual element with the load and excitation wire ports with the dimensions in figure 2.8 and each element's respective phase value shown in Appendix C.

Figure 4.1 clearly shows the an individual antenna element which is used on the 16-front elements and the 4-back elements that make up the SuperDARN radar. The wire ports are also shown to be defined at the centre of the wire segments with the loads on the top and bottom wires set to 0 Ω. As shown the antenna element is excited with a wire port also defined at the middle of the wire segment with a magnitude of 600 W and each element's respective phase value give in the phase matrix in Appendix C. The dimensions of the each wire segments have also been clearly shown which were used for the construction of the elements.

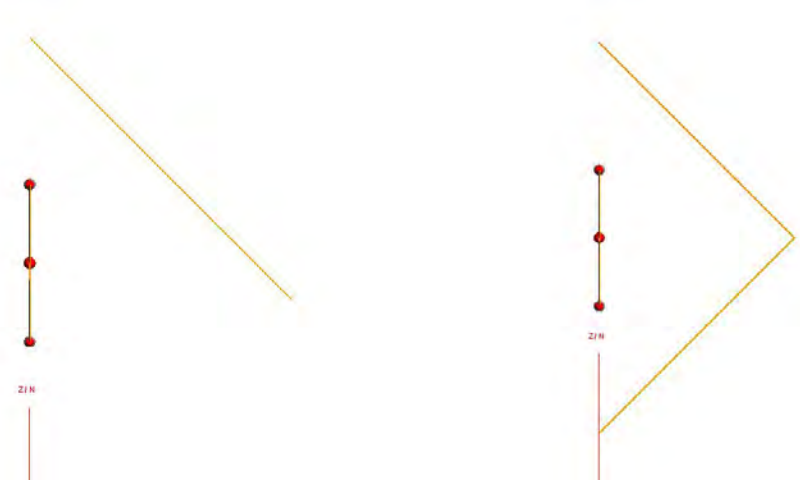

Figure 4.2: Side views of the 90° half corner reflector (left) and 90° full corner reflector (right). The two figure above show the side view of the 90° half and full corner reflectors simulated on the full-scale SuperDARN radar model.

The side views of the corner reflectors shown in figure 4.2, on the left is the currently installed 90° half corner reflector at the SANAE IV base while the figure on the right is of a 90° full corner reflector which will be simulated later in this chapter.

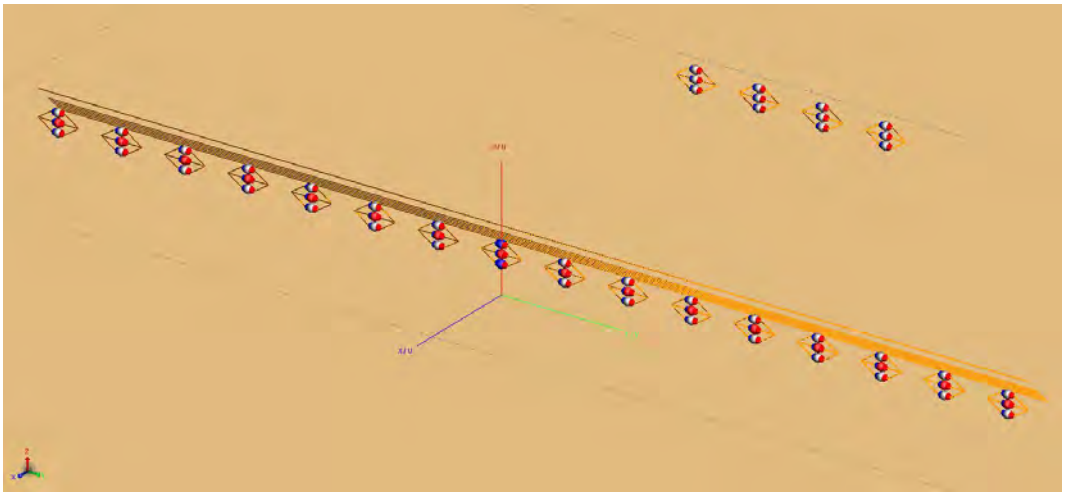

Figure 4.3: Simulation model of full-scale SuperDARN radar array with the installed 90° half corner reflector set-up over an infinite PEC ground-plane. The figure above is the isometric view of the full-scale radar antenna array with the dimensions shown in figure 2.8 over an infinite PEC ground-plane.

The SuperDARN radar is shown in figure 4.3 over an infinite PEC ground-plane, with the front 16-elements backed by the currently installed 90° half

corner reflector and behind, the 4-elements that make up the back array.

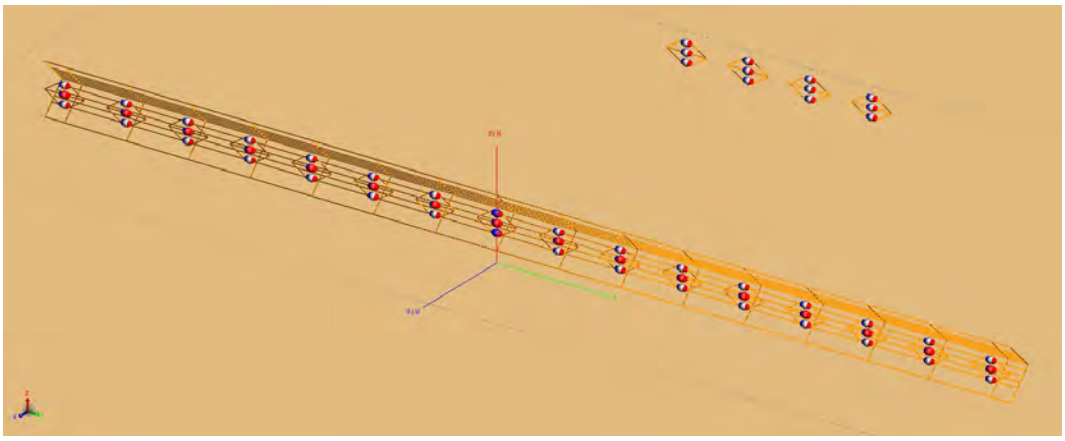

Figure 4.4: Simulation model of full-scale SuperDARN radar array with a 90° full corner reflector over an infinite PEC ground-plane. The figure above is the isometric view of the full-scale radar antenna array with a 90° full corner reflector with the antenna cable connected behind each element, over an infinite PEC ground-plane.

The 90° full corner reflector with the reflector wires connected behind the antenna elements is shown in figure 4.4 over an infinite PEC ground-plane. This is one of the 90° full corner reflector which will be discussed later in this chapter, with this figure clearly showing the antenna elements and spacing of these elements was kept the same throughout the chapter.

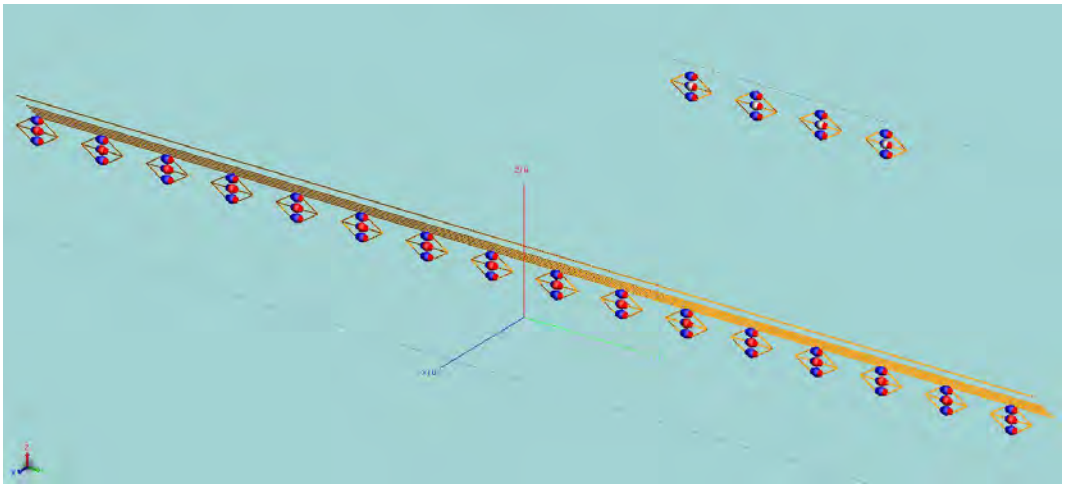

Figure 4.5: Simulation model of full-scale SuperDARN radar array with the installed 90° half corner reflector set-up over infinite ice and granite ground-plane. The figure above is the isometric view of the full-scale SuperDARN radar antenna array with the dimensions shown in figure 2.8 over an infinite ice and granite ground-plane.

Figure 4.5 shows the same SuperDARN array with the currently installed 90° half corner reflector shown in figure 4.3 but over a ground-plane consisting of an infinitely wide and deep granite medium covered with a 1 m thick and infinitely wide ice medium at -1°C.

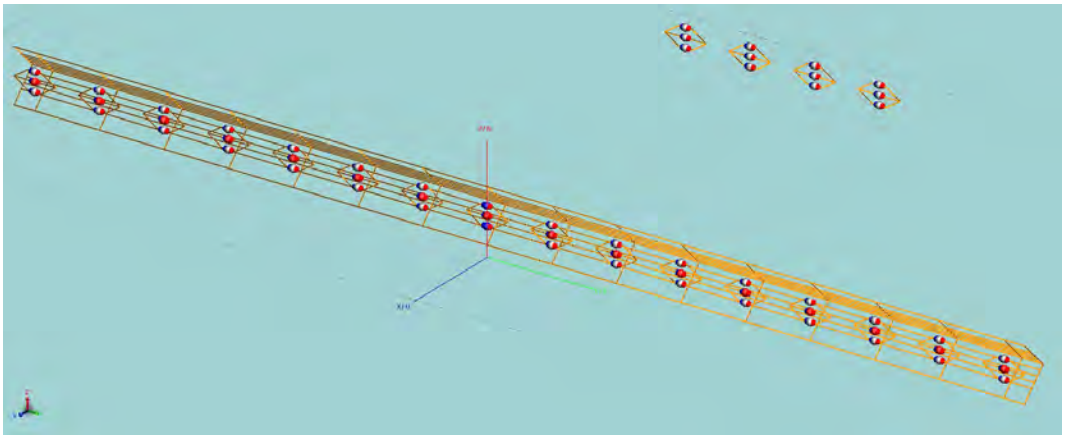

Figure 4.6: Simulation model of full-scale SuperDARN radar array with a 90° full corner reflector over an infinite PEC ground-plane. The figure above is the isometric view of the full-scale radar antenna array with a 90° full corner reflector with the antenna cable connected behind each element, over an infinite ice and granite ground-plane.

The same 90° full corner reflector configuration shown in figure 4.4 is shown in figure 4.6 over the infinite ice and granite ground-plane described above.

Figure 4.7 shows a zoomed out view to more clearly show the infinite ice and ground-plane configuration. The ice at -1°C which is 1 m thick and infinitely wide is depicted by the light blue square ground-plane shown in the figure. While, the granite ground which is both infinitely thick and wide is depicted by the brown arrows pointing down on the corners of the ground-plane.

The antenna elements and the reflectors were all constructed in the simulation software using PEC wiring, of radius 5 mm, to simulate the antenna cables used in the real-world full-scale model. Wire ports were used as excitation sources, with a magnitude of 600 W, and with a given phase value from SANSDR1 Phasing Matrix in Appendix C [18]. The loads were also defined as wire ports with their load value set to 0 Ω. The 4-back antennas, located 100 m from the 16-front elements, are identical to the front elements in the array except for their wire port excitation source set to a magnitude of 0 W i.e. the back array switched off.

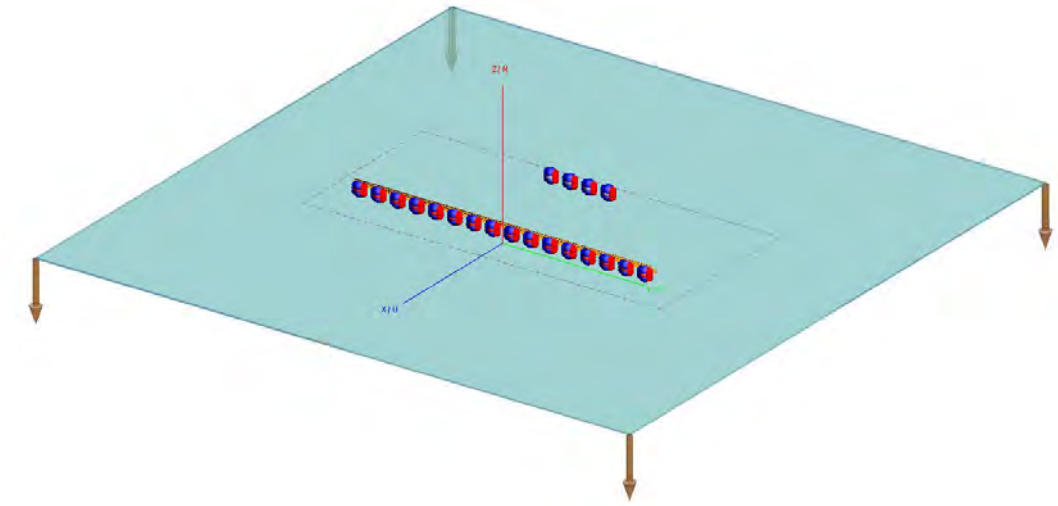

Figure 4.7: Simulation model of full-scale SuperDARN radar array with the installed 90° half corner reflector set-up over infinite ice and granite ground-plane. The figure above is the isometric view of the full-scale SuperDARN radar antenna array with the dimensions shown in figure 2.8 over an infinite ice and granite ground-plane showing the brown arrows on the corners of the ground-plane indicating a granite surface infinitely thick.

The infinite ice and granite ground consists of a layer of 1 m thick ice on top of an infinitely thick granite plane. With ice being defined as a dielectric material with the relative permittivity (ϵ_r) and conductivity (σ) characteristics of ice at -1°C using the graphs from [31] as a function of frequency. Granite was also defined as a dielectric material using the graphs from [31] but due to the large size of the simulation, it was chosen to keep the relative permittivity and conductivity as a constant instead of a function of frequency to reduce run time of the simulations. The relative permittivity and conductivity of granite were set to the worst-case scenario i.e. the lowest values of relative permittivity and conductivity with the values being 5 and 0.01 S/m respectively.

4.3 Results

The simulation results of the full-scale model are found in the subsections below, first various 90° half corner reflector set-up results are discussed in section 4.3.1, with the summary of the results shown in tables 4.1 and 4.2, in section 4.3.1.6. Section 4.3.1 then discusses what the results mean, moving on to section 4.3.2 where 90° full corner reflector set-up results are considered. Section 4.3.2.5 contains tables 4.3 and 4.4, which summarise the results of the various 90° full corner reflector set-ups.

Each 90° corner reflector set-up is compared over an infinite PEC ground to

the same set-up over an infinite granite, layered with 1 m ice, ground-plane, to more easily describe how the ice and granite influence the SuperDARN radar when it is operating at the SANAE IV base.

All results use the θ and ϕ co-ordinate system and for all polar plots in this chapter the front directivity was taken as the highest level of directivity between $\theta = 0°$ - $90°$, the back directivity was taken as the highest level of directivity between $\theta = 270°$ - $360°$ which are plotted on the angular axis of the plots. All θ angle's are measured from the zenith, shown in figure 4.8, with all polar plots taken at a plane cut of $\phi = 0°$ and all directivity levels are in dB on the radial axis of the polar plots.

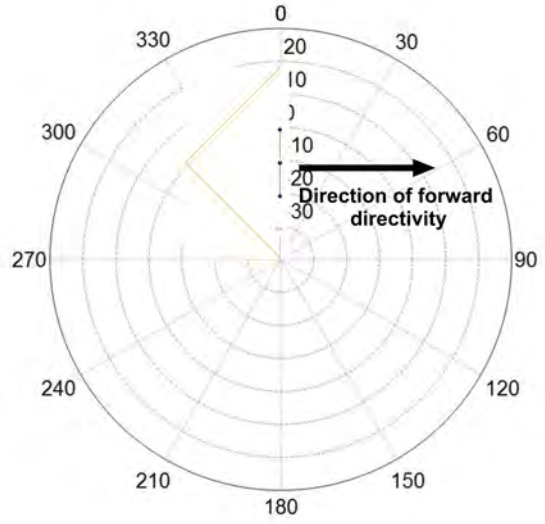

Figure 4.8: Full-scale SuperDARN radar orientation in respect to the polar plot of the results. Directivity, in dB, is on the radial axis while θ is on the angular axis with the polar plot at taken at a plane cut of $\phi = 0°$.

Figure 4.8 shows how the full-scale radar model is orientated when looking at the results on the polar plot, with the front of the antenna pointing towards the $90°$ direction on the angular axis.

4.3.1 Half Corner Reflector Results

This section considers the simulation results of the full-scale SuperDARN radar model with various $90°$ half corner reflectors. It compares the results to the same model over an infinite PEC ground-plane and over an infinite ice and granite ground-plane. The simulation models in sections 4.3.1.1 - 4.3.1.4 use

the reflector wire spacing shown in figure 4.9, which clearly shows the side view of the 90° half corner reflector.

Each antenna element in all the simulations have the dimensions shown in figure 4.1, with their respective phase value from the phase matrix in Appendix C [18]. The complete summary of results can be found in section 4.3.1.6 in tables 4.1 and 4.2.

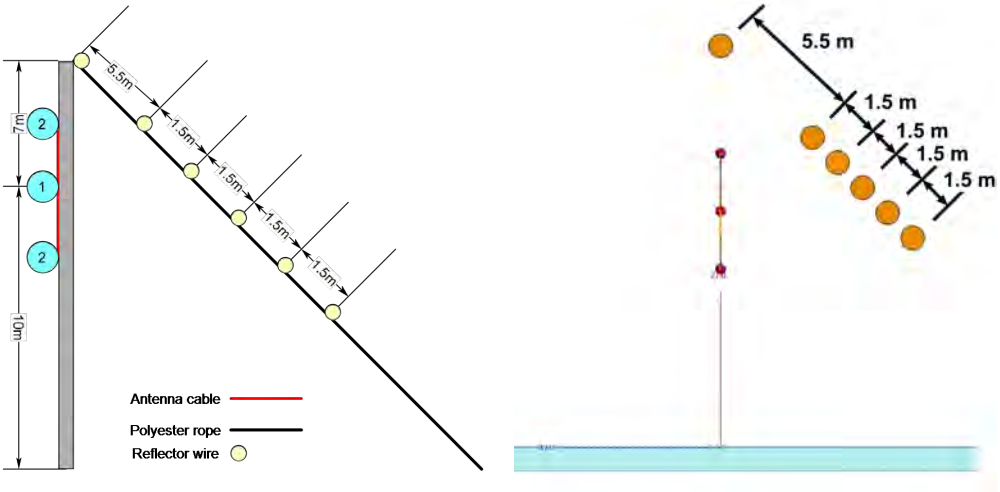

Figure 4.9: (Left)Antenna side view not to scale and (right) antenna side view to scale in FEKO. The figures above aim to give a clearer view to the scale of the dimensions for the half reflector, with the cross sections of the reflector wires in FEKO exaggerated.

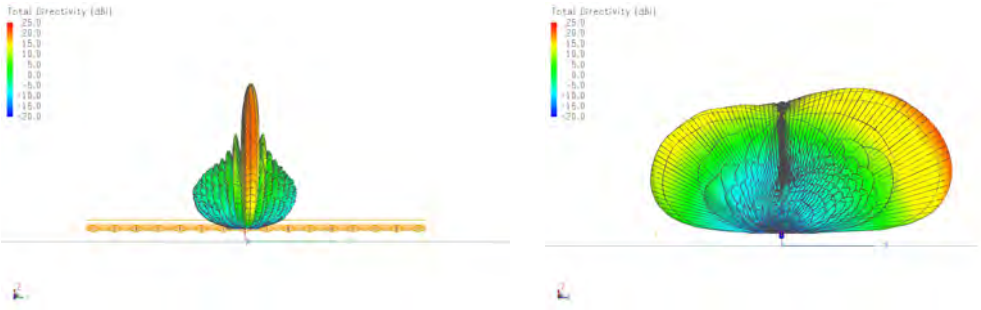

Figure 4.10: (Left) Front view and (right) left view of currently installed 90° half corner reflector with the dimensions in figure 4.9 over an infinite PEC ground. 3D Total far-field directivity results at 12.75 MHz of the installed SuperDARN radar at the SANAE IV base over an infinite PEC ground.

Figure 4.10 shows the 3D total far-field directivity of the currently installed 90° half corner reflector over an infinite PEC ground-plane, with the dimensions

in figure 4.9 from the front and left.

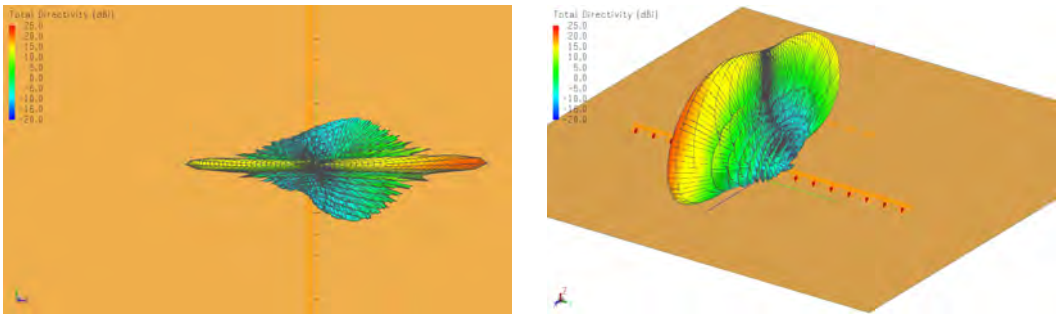

Figure 4.11: (Left) Top view and (right) isometric view of currently installed 90° half corner reflector with the dimensions in figure 4.9 over an infinite PEC ground. 3D Total far-field directivity results at 12.75 MHz of the installed SuperDARN radar at the SANAE IV base over an infinite PEC ground.

The top and ISO views of the currently installed 90° half corner reflector's 3D total far-field directivity over an infinite PEC ground-plane are shown in figure 4.11.

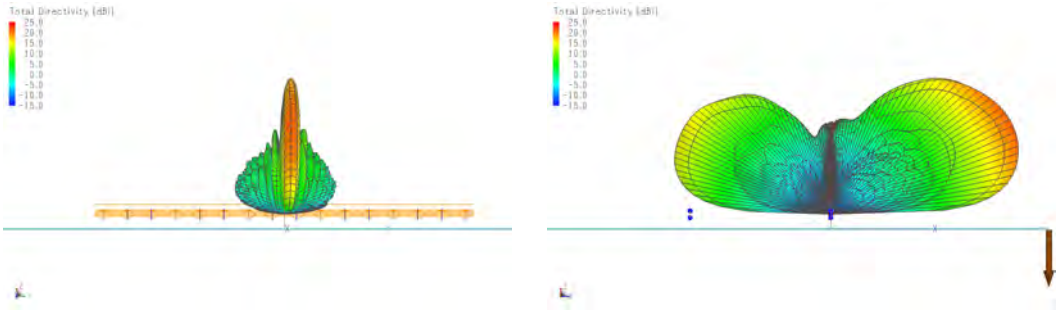

Figure 4.12: (Left) Front view and (right) left view of currently installed 90° half corner reflector with the dimensions in figure 4.9 over an infinite ice and granite ground. 3D Total far-field directivity results at 12.75 MHz of the installed Super-DARN radar array at the SANAE IV base over an infinite PEC ground.

Figure 4.12 shows the 3D total far-field directivity of the currently installed 90° half corner reflector over an infinite ice and granite ground-plane, with the dimensions in figure 4.9 from the front and left.

The top and ISO views of the currently installed 90° half corner reflector's 3D total far-field directivity over an infinite ice and granite ground-plane are shown in figure 4.13. The results of the simulations will be discussed in terms of polar plots for the following sections as directivity results can be quantified on polar plots.

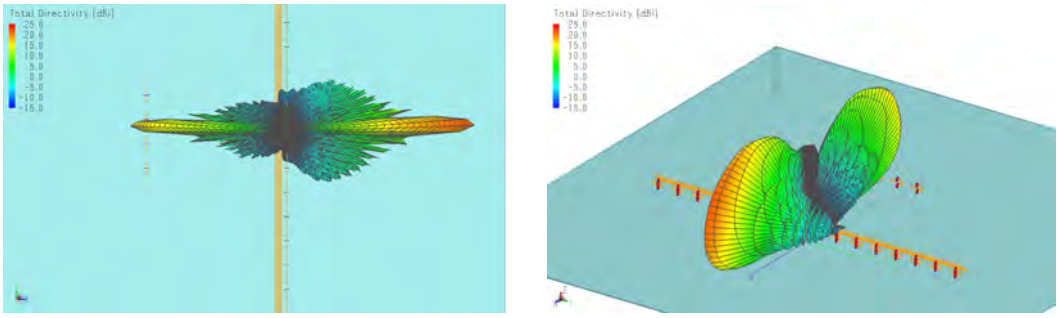

Figure 4.13: (Left) Top view and (right) isometric view of currently installed 90° half corner reflector with the dimensions in figure 4.9 over an infinite ice and granite ground. 3D Total far-field directivity results at 12.75 MHz of the installed SuperDARN radar array at the SANAE IV base over an infinite PEC ground.

4.3.1.1 Installed 90° Half Corner Reflector

Results are obtained of the first configuration of the installed 90° half corner wire reflector which is currently operating at the SANAE IV base, with its reflector dimensions shown in figure 4.9 and the reflector wires connected at the ends of the reflector shown in figure 4.14.

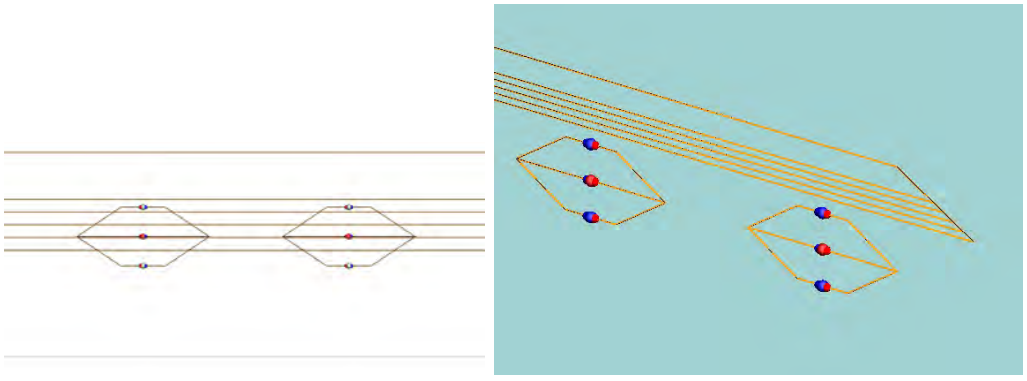

Figure 4.14: (Left) Back view and (right) ISO view of the 90° half corner reflector installed at the SANAE IV base. Back and ISO view of the current 90° half corner reflector installed at the SANAE IV base in the simulation model.

Over an infinite PEC ground-plane the installed 90° half corner wire reflector has a forward directivity level of 19.4 dB with a θ of 58° and a reverse directivity level of 11 dB with a θ of 51.9°, giving a front-to-back ratio of 8.4 dB.

Over an infinite ice and granite ground-plane the installed 90° half corner wire reflector has a forward directivity level of 18.1 dB with a θ of 62° and a reverse directivity level of 11.7 dB with a θ of 55.7°, giving a front-to-back ratio of 6.4 dB. With the comparison of ground-plane results shown on the polar plot in figure 4.15, the blue plot is the model over the infinite PEC ground-plane

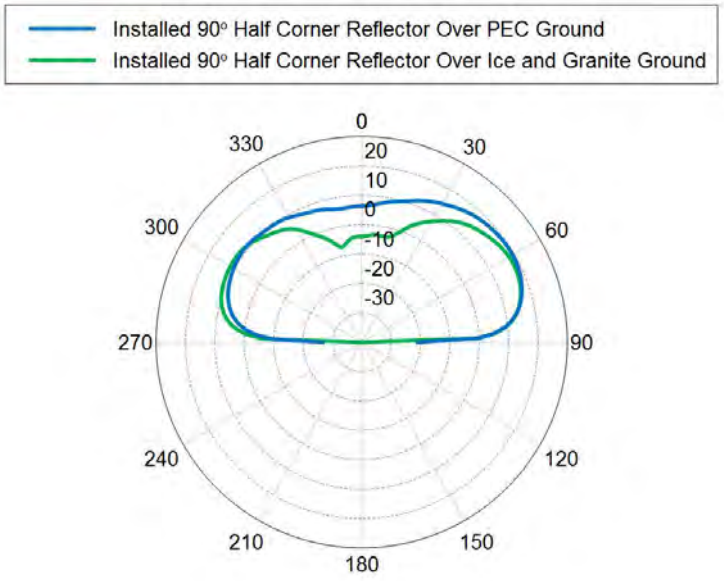

Figure 4.15: Directivity simulation results of the 90° half corner reflector installed at the SANAE IV base. The blue plot is the simulation model over an infinite PEC ground-plane while the green plot is the same model over an infinite ice and granite ground-plane.

while the green plot is the same model over an infinite ice and granite ground-plane. The angular axis shows the θ angles, the plot is taken at the plane cut of $\phi = 0°$ and the directivity levels are in dB on the radial axis.

PEC provides an ideal reflective surface with no losses, where the ice/granite has losses and does not reflect as perfectly. Hence the decrease in front-to-back ratio.

4.3.1.2 Installed 90° Half Corner Reflector Connected Behind Elements

This next section of results is of the 90° half corner wire reflector currently operating at the SANAE IV base, with its reflector dimensions shown in figure 4.9 and the reflector wires connected at the ends of the reflector and behind the antenna elements, shown in figure 4.16 which clearly show the connection locations of the added reflector wires behind the elements. The reason for extra connections are to replicate a more solid reflector surface compared to wavelength.

Over an infinite PEC ground-plane the 90° half corner wire reflector, with the reflector wires connected behind the antenna elements, has a forward directivity level of 19.4 dB with a θ of 58° and a reverse directivity level of 11.1 dB

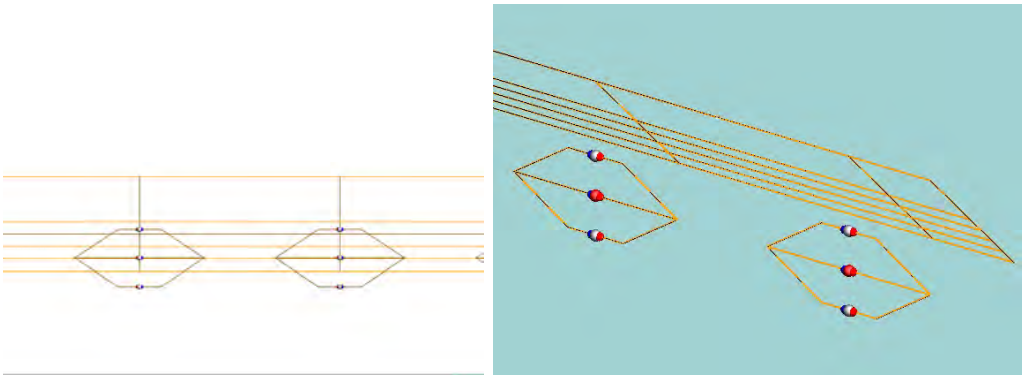

Figure 4.16: (Left) Back view and (right) ISO view of the 90° half corner reflector with the reflector wires connected behind the antenna elements. Back and ISO view of a similar 90° half corner reflector installed at the SANAE IV base, but with the reflector wires connected behind the antenna elements, in the simulation model.

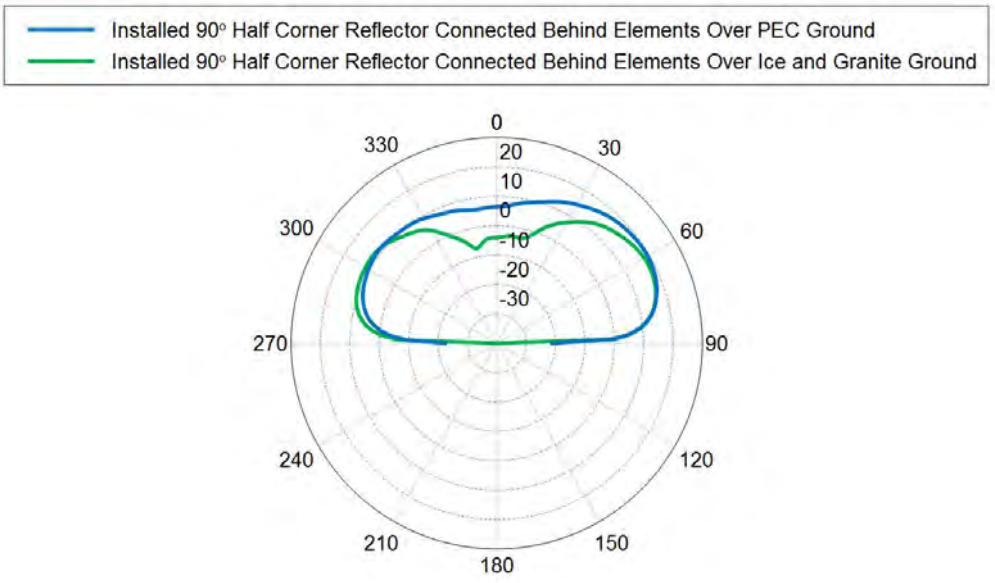

Figure 4.17: Directivity simulation results of the 90° half corner reflector installed at the SANAE IV base with the reflector wires connected behind the antenna elements. The blue plot is the simulation model over an infinite PEC ground-plane while the green plot is the same model over an infinite ice and granite ground-plane.

with a θ of 52.4°, giving a front-to-back ratio of 8.3 dB.

Over an infinite ice and granite ground-plane the 90° half corner wire reflector, with the reflector wires connected behind the antenna elements, has a forward directivity level of 18.1 dB with a θ of 62° and a reverse directivity level of 11.7 dB with a θ of 58.1°, giving a front-to-back ratio of 6.4 dB. The comparison

of ground-plane results are shown on the polar plot in figure 4.17, the blue plot is over the infinite PEC ground-plane while the green plot is the same model over an infinite ice and granite ground-plane. The angular axis shows the θ angles, the plot is taken at the plane cut of $\phi = 0°$ and the directivity levels are in dB on the radial axis.

The front-to-back ratio with the PEC ground-plane decreases by 0.1 dB compared to the previous section, while the PEC compared to ice and granite ground-plane are very similar ratios.

4.3.1.3 Installed 90° Half Corner Reflector Connected Behind and In-Between Elements

This section of results is of the 90° half corner wire reflector currently operating at the SANAE IV base, with its reflector dimensions shown in figure 4.9 and the reflector wires connected at the ends of the reflector, behind and in-between the antenna elements, shown in figure 4.18, showing the connection points behind and in-between the antenna elements. With the addition of more reflector wires connections further improving the reflector's surface area.

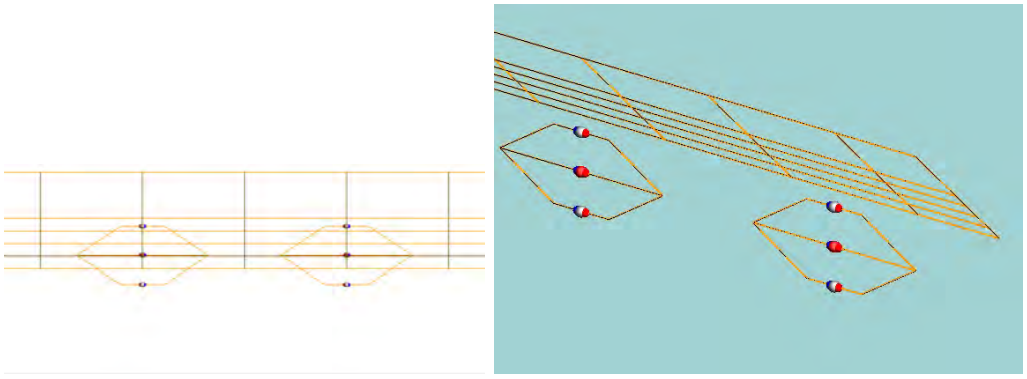

Figure 4.18: (Left) Back view and (right) ISO view of the 90° half corner reflector with the reflector wires connected behind and in-between the antenna elements. Back and ISO view of a similar 90° half corner reflector installed at the SANAE IV base, but with the reflector wires connected behind and in-between the antenna elements, in the simulation model.

Over an infinite PEC ground-plane the 90° half corner wire reflector, with the reflector wires connected behind and in-between the antenna elements, has a forward directivity level of 19.4 dB with a θ of 58° and a reverse directivity level of 11.2 dB with a θ of 51.8°, giving a front-to-back ratio of 8.2 dB.

Over an infinite ice and granite ground-plane the 90° half corner wire reflector, with the reflector wires connected behind and in-between the antenna elements,

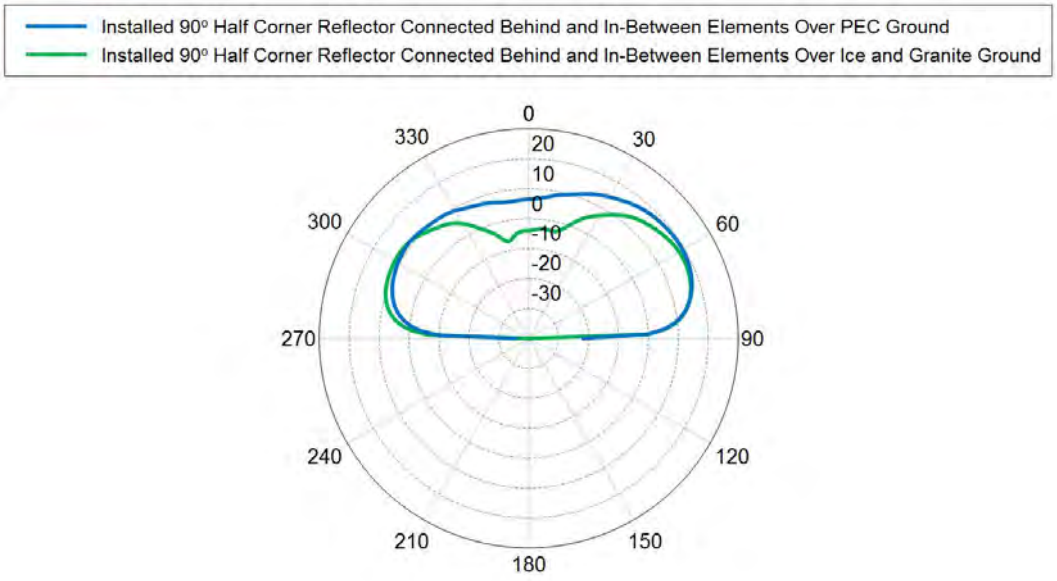

Figure 4.19: Directivity simulation results of the 90° half corner reflector installed at the SANAE IV base with the reflector wires connected behind and in-between the antenna elements. The blue plot is the simulation model over an infinite PEC ground-plane, the green plot is the same model over an infinite ice and granite ground-plane.

has a forward directivity level of 18.1 dB with a θ of 62° and a reverse directivity level of 11.7 dB with a θ of 58.1°, giving a front-to-back ratio of 6.4 dB. With the comparison of ground-plane results shown on the polar plot in figure 4.19, the blue plot is the model over the infinite PEC ground-plane while the green plot is the same model over an infinite ice and granite ground-plane. The angular axis shows the θ angles, the plot is taken at the plane cut of $\phi = 0°$ and the directivity levels are in dB on the radial axis.

The change in front-to-back ratio with the PEC ground-plane was negligible when compared to the previous section and the PEC compared to ice and granite ground-plane were again very similar ratios.

4.3.1.4 Installed 90° Half Corner Reflector Connected Behind, In-Between and In-Between Elements Again

This section of results is of the 90° half corner wire reflector currently operating at the SANAE IV base, with its reflector dimensions shown in figure 4.9 and the reflector wires connected at the ends of the reflector, behind, in-between and in-between again the antenna elements, with all the connection points along the reflector clearly shown in figure 4.20. This last scenario using the SuperDARN radar wire spacing is the reflector set-up which provides the largest surface

area.

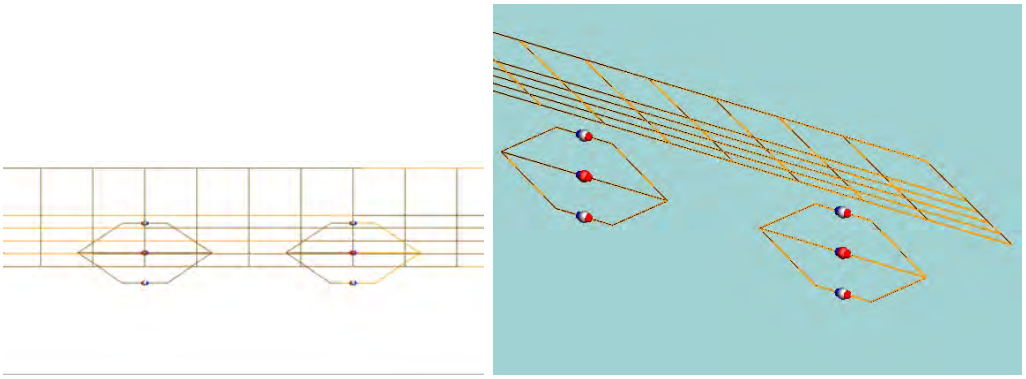

Figure 4.20: (Left) Back view and (right) ISO view of the 90° half corner reflector with the reflector wires connected behind and in-between, then in-between again, the antenna elements. Back and ISO view of a similar 90° half corner reflector installed at the SANAE IV base, but with the reflector wires connected behind and in-between, then in-between again, the antenna elements, in the simulation model.

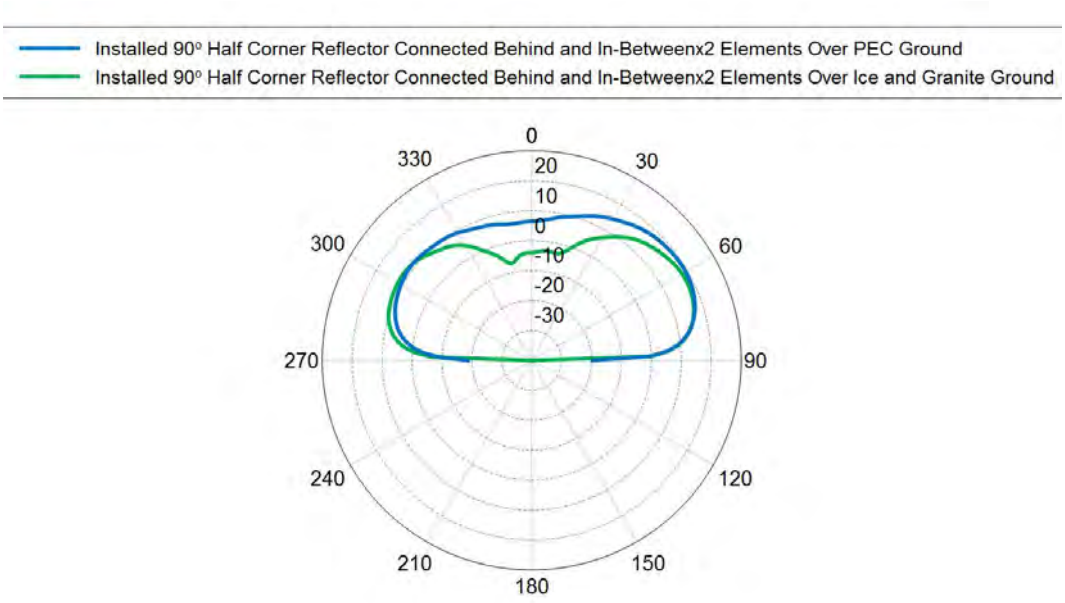

Figure 4.21: Directivity simulation results of the 90° half corner reflector installed at the SANAE IV base with the reflector wires connected behind and in-between, then in-between again, the antenna elements. The blue plot is the simulation model over an infinite PEC ground-plane while the green plot is the same model over an infinite ice and granite ground-plane.

Over an infinite PEC ground-plane the 90° half corner wire reflector, with the reflector wires connected behind, in-between and in-between again the antenna elements, has a forward directivity level of 19.4 dB with a θ of 58° and a reverse directivity level of 11.2 dB with a θ of 52.4°, giving a front-to-back ratio of 8.2 dB.

Over an infinite ice and granite ground-plane the installed 90° half corner wire reflector, with the reflector wires connected behind, in-between and in-between again the antenna elements, has a forward directivity level of 18.1 dB with a θ of 62° and a reverse directivity level of 11.7 dB with a θ of 58°, giving a front-to-back ratio of 6.4 dB. The comparison of ground-plane results are shown on the polar plot in figure 4.21, the blue plot is over the infinite PEC ground-plane while the green plot is the same model over an infinite ice and granite ground-plane. The angular axis shows the θ angles, the plot is taken at the plane cut of $\phi = 0°$ and the directivity levels are in dB on the radial axis.

The improvement of the front-to-back over the PEC ground-plane can again be considered negligible when compared to the previous section and the PEC compared to ice and granite ground-plane has a very similar ratio.

4.3.1.5 90° Half Corner Reflector with Equal Wire Spacing Connected Behind Elements

This section of results is of a 90° half corner wire reflector with the reflector wires equally spaced with 1.4 m between each wire to ensure a true equally spaced corner reflector, with figure 4.22 clearly showing this 1.4 m spacing between the reflector wire. Figure 4.23 shows the connection points of the added reflector wiring connected behind the antenna element.

Over an infinite PEC ground-plane the 90° half corner wire reflector with equal wire spacing, connected behind the antenna elements, has a forward directivity level of 19.1 dB with a θ of 60° and a reverse directivity level of 13.4 dB with a θ of 51.5°, giving a front-to-back ratio of 5.7 dB.

Over an infinite ice and granite ground-plane the 90° half corner wire reflector with equal wire spacing, connected behind the antenna elements, has a forward directivity level of 17.8 dB with a θ of 64° and a reverse directivity level of 12.5 dB with a θ of 57.6°, giving a front-to-back ratio of 5.3 dB. The comparison of ground-plane results are shown on the polar plot in figure 4.24, the blue plot is over the infinite PEC ground-plane while the green plot is the same model over an infinite ice and granite ground-plane. The angular axis shows the θ angles, the plot is taken at the plane cut of $\phi = 0°$ and the directivity levels are in dB on the radial axis.

There is a decrease in front-to-back by 2.5 dB over the PEC ground-plane when

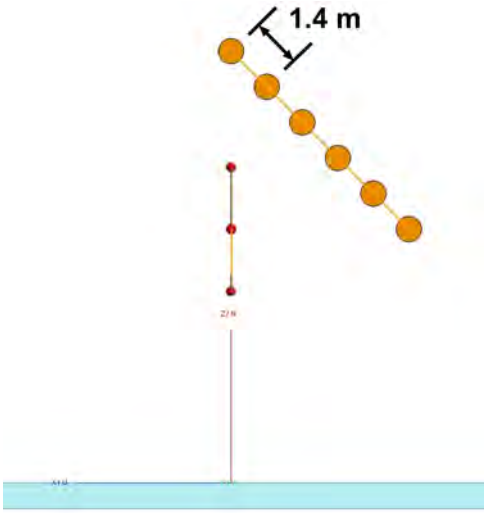

Figure 4.22: Side view of equally spaced 90° half corner reflector with the wires connected behind the antenna elements. Cross section of the side view of a 90° half corner reflector with the reflector wires equally spaced in the simulation model, wire cross sections are exaggerated.

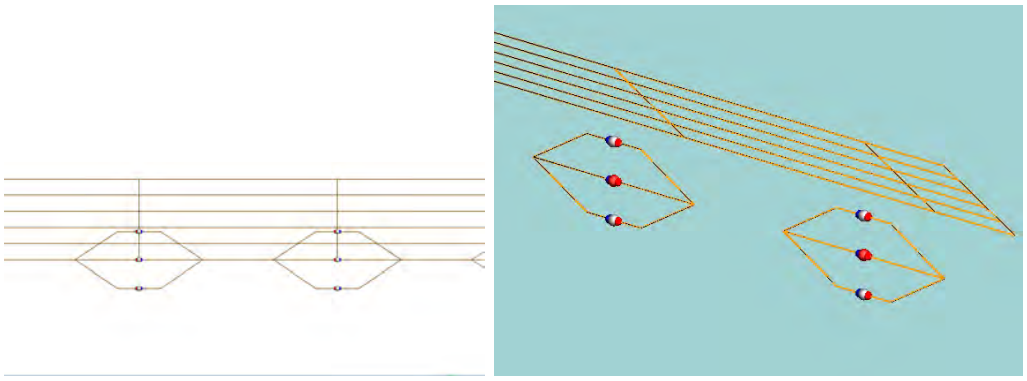

Figure 4.23: (Left) back view and (right) ISO view of a 90° half corner reflector with the wires equally spaced and connected behind the antenna elements. Back and ISO view of a 90° half corner reflector with the reflector wires equally spaced in the simulation model.

compared to the previous section. While the PEC compared to ice and granite ground-plane have the lowest forward directivity level and the hight reverse directivity level of all the 90° half corner wire reflector set-ups simulated.

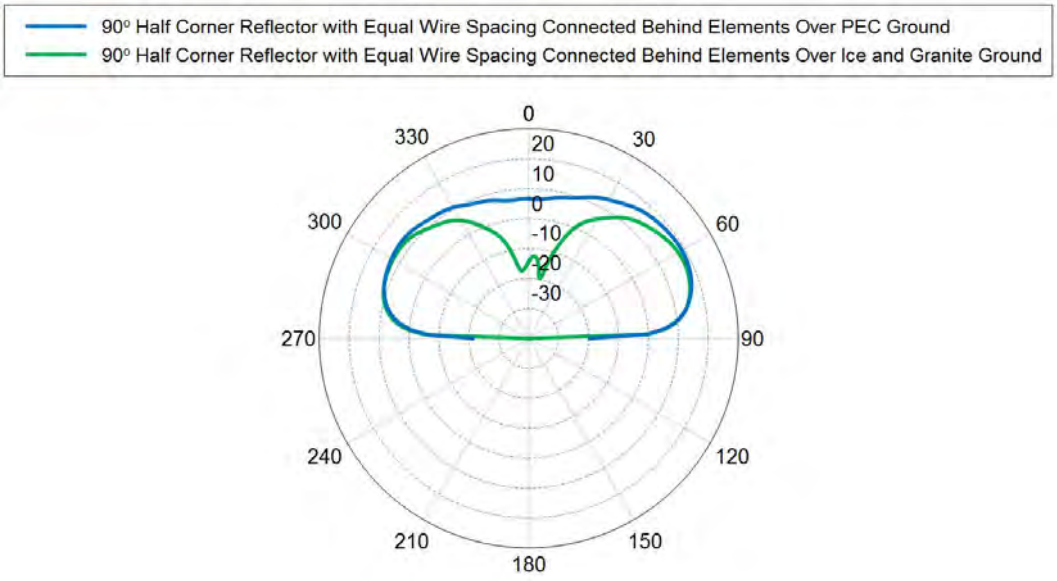

Figure 4.24: Directivity simulation results of a 90° half corner reflector with the reflector wires equally spaced from each other and connected behind the antenna elements. The blue plot is the simulation model over an infinite PEC ground-plane while the green plot is the same model over an infinite ice and granite ground-plane.

4.3.1.6 Summary of Half Corner Reflector Results

In this section the 90° half corner wire reflectors are summarised first in table 4.1 for the different models over an infinite PEC ground-plane and then in table 4.2 for the same models over an infinite granite ground-plane layer with a 1 m thick layer of ice at -1°C. It is important to note that all angles in tables 4.1 and 4.2 are taken from the zenith.

Table 4.1: Simulation results of full-scale SuperDARN radar array with a 90° half corner reflector over an infinite PEC ground.

Model	Front Directivity and Angle	Back Directivity and Angle	Front-to-Back Ratio
·Wire corner reflector (half) ·Current set-up	19.4 dB 58°	11 dB 51.9°	8.4 dB
·Wire corner reflector (half) ·Connected behind elements	19.4 dB 58°	11.1 dB 52.4°	8.3 dB
·Wire corner reflector (half) ·Connected behind elements and in-between	19.4 dB 58°	11.2 dB 51.8°	8.2 dB
·Wire corner reflector (half) ·Connected behind elements and in-between x 2	19.4 dB 58°	11.2 dB 52.4°	8.2 dB
·Wire corner reflector (half) ·Connected behind elements ·Equal wire spacing	19.1 dB 60°	13.4 dB 51.5°	5.7 dB

Table 4.2: Simulation results of full-scale SuperDARN radar array with a 90° half corner reflector over an infinite ice and granite ground.

Model	Front Directivity and Angle	Back Directivity and Angle	Front-to-Back Ratio
· Wire corner reflector (half) ·Installed set-up	18.1 dB 62°	11.7 dB 55.7°	6.4 dB
·Wire corner reflector (half) ·Connected behind elements	18.1 dB 62°	11.7 dB 58.1°	6.4 dB
·Wire corner reflector (half) ·Connected behind elements and in-between	18.1 dB 62°	11.7 dB 58.1°	6.4 dB
·Wire corner reflector (half) ·Connected behind elements and in-between x 2	18.1 dB 62°	11.7 dB 58°	6.4 dB
·Wire corner reflector (half) ·Connected behind elements ·Equal wire spacing	17.8 dB 64°	12.5 dB 57.6°	5.3 dB

4.3.1.7 Discussion

The polar plots shown in figures 4.15, 4.17, 4.19, 4.21 and 4.24 are the results in section 4.3.1, the biggest difference between the results of a model over an infinite PEC ground-plane versus the over an infinite ice and granite ground-plane occur directly above the antenna element. This can be attributed to two factors, firstly, the difference in relative permittivity (ϵ_r) and conductivity (σ) between the two ground-planes i.e. the PEC ground-plane reflects the EM waves from the SuperDARN radar with minimal loses while the ice and granite ground-plane reflects the EM waves though some energy is dissipated through the ice and granite. This is further confirmed by the decrease θ for both the forward and reverse directivity. Secondly, the 90° half corner reflector, while reflecting EM waves in the forward direction, also reflects a large amount of the EM waves directly back into the ground-plane and not outwards to the forward direction of the array. From these results of increasing the surface area of the reflector by adding more wires to the 90° half corner wire reflector, little to no improvement the front-to-back ratio for all of the set-ups simulated.

With respects to the two different ground-planes, the forward directivity levels only decrease by around 1.3 dB for each model while the reverse directivity levels remain practically unchanged. This indicates two particular points; firstly the 90° half corner wire reflector does indeed reflect EM waves to the forward direction but secondly, it does little to hinder EM wave propagation in the reverse direction. To try and improve on this hindrance of EM wave propagation in the reverse direction a 90° full corner wire reflector was looked at next.

4.3.2 Full Corner Reflector Results

This section considers the simulation results of the full-scale SuperDARN radar model with various 90° full corner reflectors and compares the results to the same model over an infinite PEC ground-plane and over an infinite ice and granite ground-plane. The simulation models in sections 4.3.2.1 - 4.3.2.3 the reflector dimensions shown in figure 4.25. In order to keep the 1.5 m wire spacings, the initial wire spacing of 5.5 m was reduced to 3.9 m.

Each antenna element in all the simulations have the dimensions shown in figure 4.1, with their respective phase value from the phase table in [18]. The complete summary of results can be found in section 4.3.2.5 in tables 4.3 and 4.4.

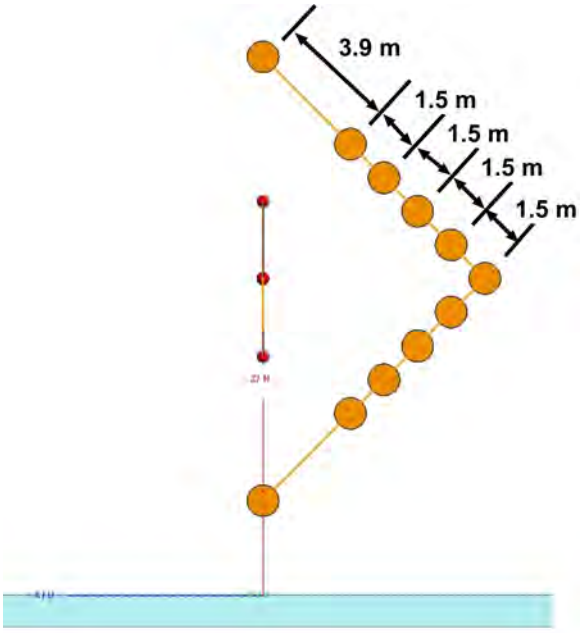

Figure 4.25: Antenna side view showing the 90° full corner wire reflector to scale in FEKO. The figure above shows the dimensions of the 90° full corner wire reflector simulated in FEKO with the wire cross sections exaggerated.

Figure 4.26: (Left) Front view and (right) left view 90° full corner reflector over an infinite PEC ground-plane. 3D Total far-field directivity simulation results at 12.75 MHz of the SuperDARN radar array with a 90° full corner reflector over an infinite PEC ground.

Figure 4.26 shows the 3D total far-field directivity, front the front and left, of a 90° full corner reflector with the reflector wires connected behind the antenna elements and the dimensions in figure 4.25 over an infinite PEC ground-plane.

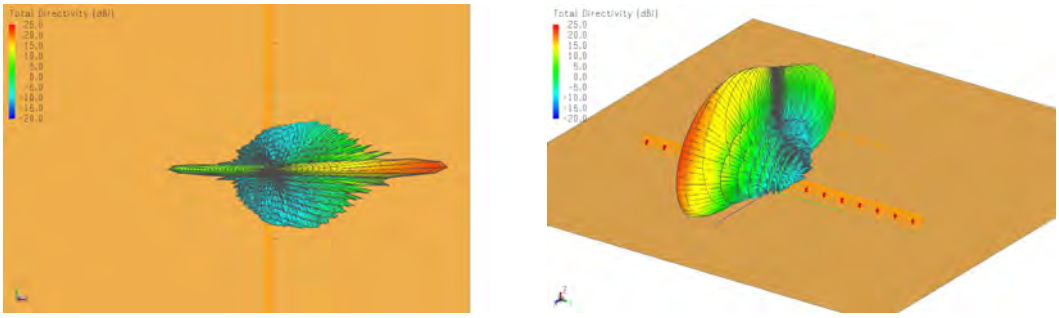

Figure 4.27: (Left) top view and (right) isometric view of 90° full corner reflector over an infinite PEC ground-plane. 3D Total far-field directivity simulation results at 12.75 MHz of the SuperDARN radar array with a 90° full corner reflector over an infinite PEC ground.

The top and ISO views are shown in figure 4.27 of a 90° full corner reflector with the reflector wires connected behind the antenna elements over an infinite PEC ground-plane.

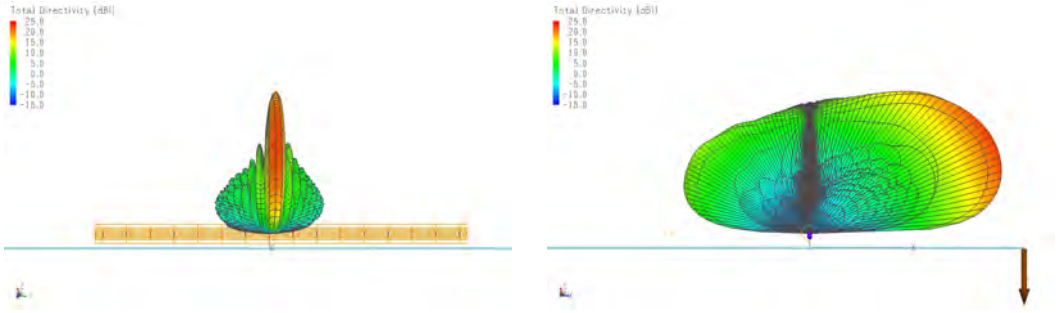

Figure 4.28: (Left) front view and (right) left view of 90° full corner reflector over an infinite ice and granite ground-plane. 3D Total far-field directivity results at 12.75 MHz of the SuperDARN radar with a 90° full corner reflector over an infinite ice and granite ground.

Figure 4.28 shows the 3D total far-field directivity, front the front and left, of a 90° full corner reflector with the reflector wires connected behind the antenna elements and the dimensions in figure 4.25 over an infinite ice and granite ground-plane.

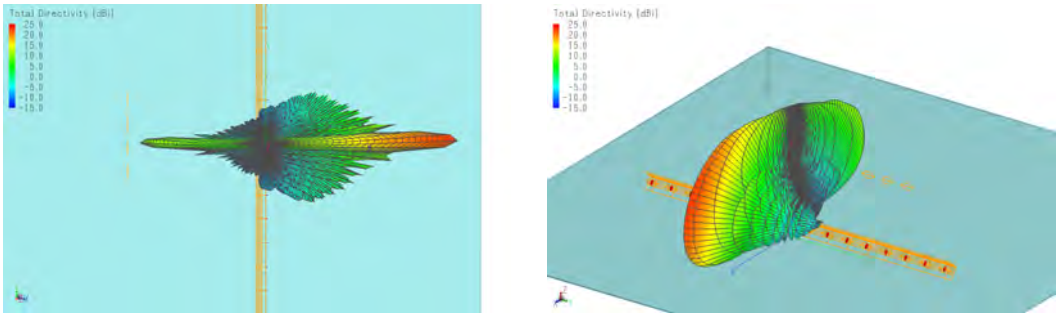

Figure 4.29: (Left) top view and (right) isometric view of 90° full corner reflector over an infinite ice and granite ground-plane. 3D Total far-field directivity results at 12.75 MHz of the SuperDARN radar with a 90° full corner reflector over an infinite ice and granite ground.

The top and ISO views are shown in figure 4.29 of a 90° full corner reflector with the reflector wires connected behind the antenna elements over an infinite ice and granite ground-plane.

4.3.2.1 90° Full Corner Reflector Connected Behind Elements

This first section of results is of the 90° full corner wire reflector, with its reflector dimensions shown in figure 4.9 and the reflector wires connected at the ends of the reflector and behind the antenna elements, clearly shown in figure 4.30.

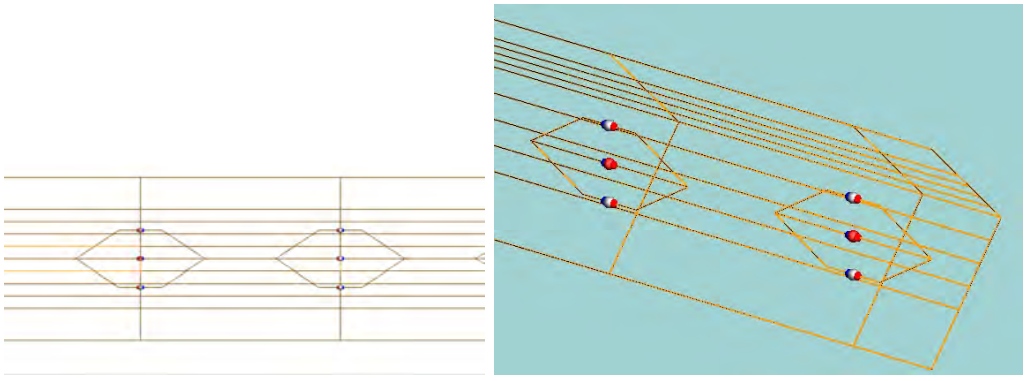

Figure 4.30: (Left) Back view and (right) ISO view of a 90° full corner reflector with the reflector wires connected behind the antenna elements. Back and ISO view of a 90° full corner reflector with the reflector wires connected behind the antenna elements, in the simulation model.

Over an infinite PEC ground-plane the 90° full corner wire reflector, with the

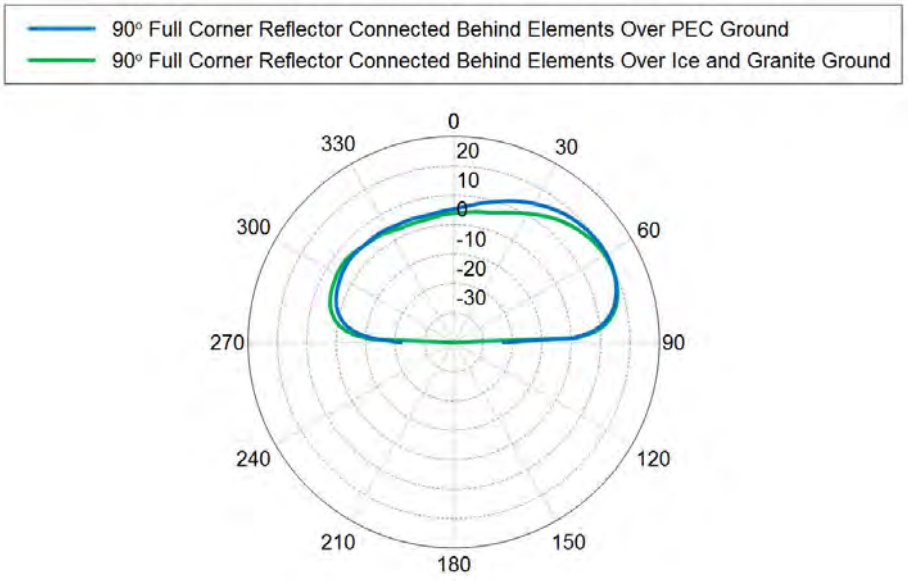

Figure 4.31: Directivity simulation results of the 90° full corner reflector with the reflector wires connected behind the antenna elements. The blue plot is the simulation model over an infinite PEC ground-plane while the green plot is the same model over an infinite ice and granite ground-plane.

reflector wires connected behind the antenna elements, has a forward directivity level of 20 dB with a θ of 60° and a reverse directivity level of 5.2 dB with a θ of 50.4°, giving a front-to-back ratio of 14.8 dB.

Over an infinite ice and granite ground-plane the 90° full corner wire reflector, with the reflector wires connected behind the antenna elements, has a forward directivity level of 19.5 dB with a θ of 64° and a reverse directivity level of 6.2 dB with a θ of 54.1°, giving a front-to-back ratio of 13.3 dB. The comparison of ground-plane results are shown on the polar plot in figure 4.31, the blue plot is over the infinite PEC ground-plane while the green plot is the same model over an infinite ice and granite ground-plane. The angular axis shows the θ angles, the plot is taken at the plane cut of $\phi = 0°$ and the directivity levels are in dB on the radial axis.

PEC provides an ideal reflective surface with no losses, where the ice/granite has losses and does not reflect as perfectly. Hence the decrease in front-to-back ratio.

For the rest of this report, this 90° full corner reflector set-up will be referred to as the proposed 90° full corner reflector as it has the greatest increase in performance of the front-to-back ratio, over an infinite ice and granite ground-plane, of all the set-ups simulated, while requiring the least amount of reflector

wiring to construct.

4.3.2.2 90° Full Corner Reflector Connected Behind and In-Between Elements

This next section of results is of the 90° full corner wire reflector, with its reflector dimensions shown in figure 4.9, with the reflector wires connected at the ends of the reflector, behind and in-between the antenna elements, shown in figure 4.32.

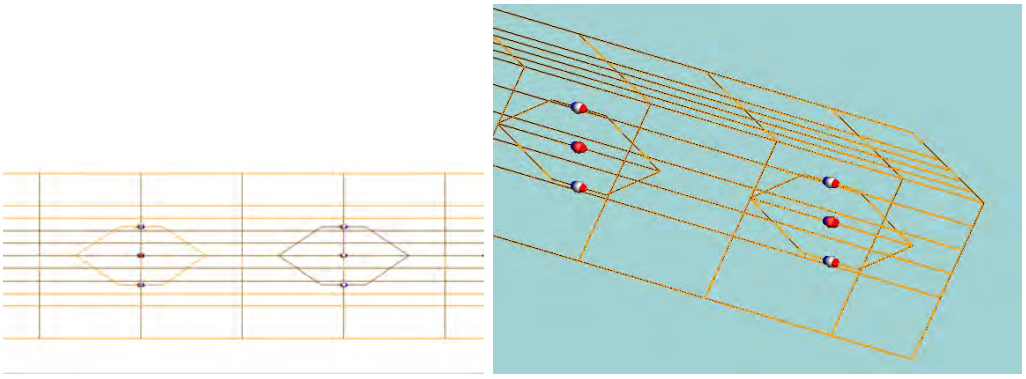

Figure 4.32: (Left) Back view and (right) ISO view of a 90° full corner reflector base with the reflector wires connected behind and in-between the antenna elements. Back and ISO view of a 90° full corner reflector with the reflector wires connected behind and in-between the antenna elements, in the simulation model.

Over an infinite PEC ground-plane the 90° full corner wire reflector, with the reflector wires connected behind and in-between the antenna elements, has a forward directivity level of 19.9 dB with a θ of 60° and a reverse directivity level of 5.2 dB with a θ of 50.4°, giving a front-to-back ratio of 14.7 dB.

Over an infinite ice and granite ground-plane the 90° full corner wire reflector, with the reflector wires connected behind and in-between the antenna elements, has a forward directivity level of 19.5 dB with a θ of 64° and a reverse directivity level of 6.2 dB with a θ of 54°, giving a front-to-back ratio of 13.3 dB. With the comparison of ground-plane results shown on the polar plot in figure 4.33, the blue plot is the model over the infinite PEC ground-plane while the green plot is the same model over an infinite ice and granite ground-plane. The angular axis shows the θ angles, the plot is taken at the plane cut of $\phi = 0°$ and the directivity levels are in dB on the radial axis.

The decrease in front-to-back ratio with the PEC ground-plane was negligible when compared to the previous section and the PEC compared to ice and granite ground-plane were again very similar ratios.

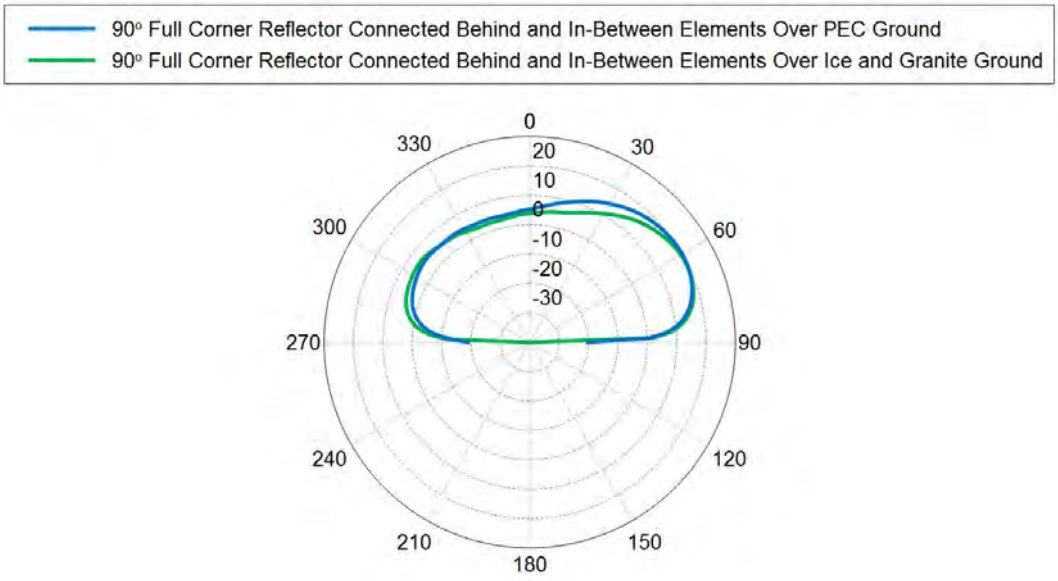

Figure 4.33: Directivity simulation results of the 90° full corner reflector with the reflector wires connected behind and in-between the antenna elements. The blue plot is the simulation model over an infinite PEC ground-plane while the green plot is the same model over an infinite ice and granite ground-plane.

4.3.2.3 90° Full Corner Reflector Connected Behind, In-Between and In-Between Elements Again

This section of results is of the 90° full corner wire reflector, with its reflector dimensions shown in figure 4.9, with the reflector wires connected at the ends of the reflector, behind, in-between and in-between again, the antenna elements, shown in figure 4.34.

Over an infinite PEC ground-plane the 90° full corner wire reflector, with the reflector wires connected at the ends of the reflector, behind, in-between and in-between again, the antenna elements, has a forward directivity level of 20 dB with a θ of 60° and a reverse directivity level of 5.2 dB with a θ of 49.8°, giving a front-to-back ratio of 14.8 dB.

Over an infinite ice and granite ground-plane the 90° full corner wire reflector, the reflector wires connected at the ends of the reflector, behind, in-between and in-between again, the antenna elements, has a forward directivity level of 19.5 dB with a θ of 64° and a reverse directivity level of 6.2 dB with a θ of 54°, giving a front-to-back ratio of 13.3 dB. The comparison of ground-plane results are shown on the polar plot in figure 4.35, the blue plot is over the infinite PEC ground-plane while the green plot is the same model over an infinite ice and granite ground-plane. The angular axis shows the θ angles, the plot is

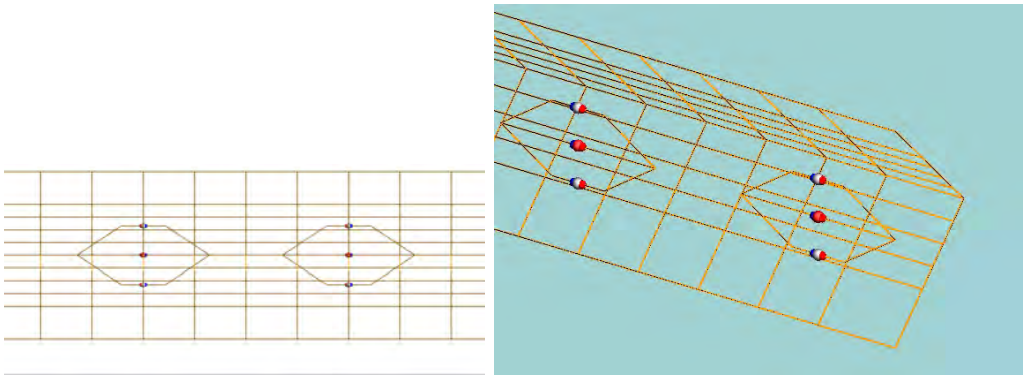

Figure 4.34: (Left) Back view and (right) ISO view of a 90° full corner reflector with the reflector wires connected behind and in-between, then in-between again, the antenna elements. Back and ISO view of a 90° full corner reflector with the reflector wires connected behind and in-between, then in-between again, the antenna elements, in the simulation model.

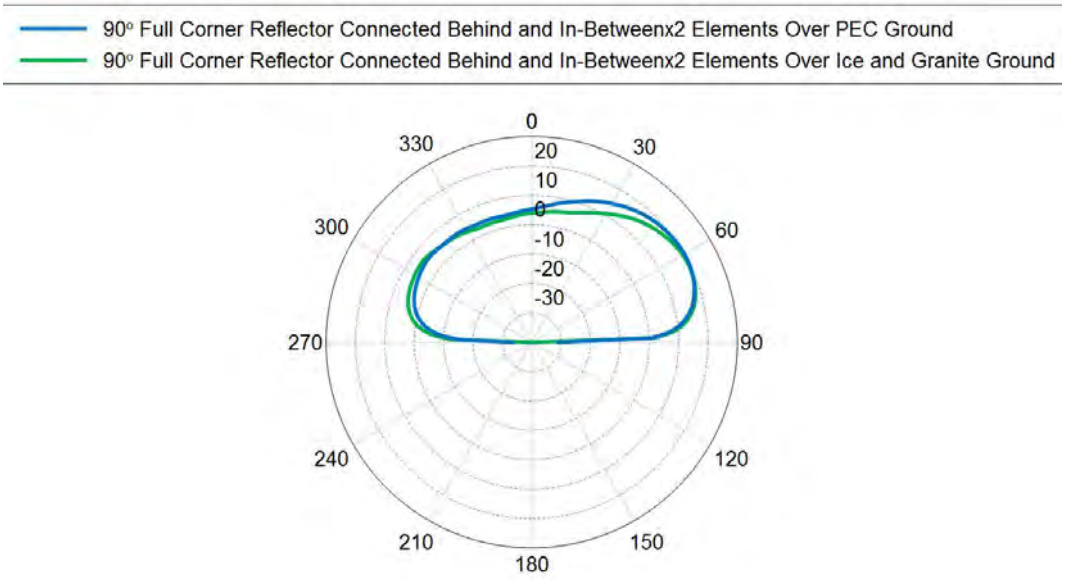

Figure 4.35: Directivity simulation results of the 90° full corner reflector with the reflector wires connected behind and in-between, then in-between again, the antenna elements. The blue plot is the simulation model over an infinite PEC ground-plane while the green plot is the same model over an infinite ice and granite ground-plane.

taken at the plane cut of $\phi = 0°$ and the directivity levels are in dB on the radial axis.

The improvement of the front-to-back over the PEC ground-plane can be considered negligible when compared to the previous section and the PEC com-

pared to ice and granite ground-plane has a very similar ratio.

4.3.2.4 90° Full Corner Reflector with Equal Wire Spacing Connected Behind Elements

This final section of results is of a 90° full corner wire reflector with the reflector wires equally spaced with 1.4 m between each wire to ensure a true equally spaced corner reflector, show in figures 4.36 and 4.37.

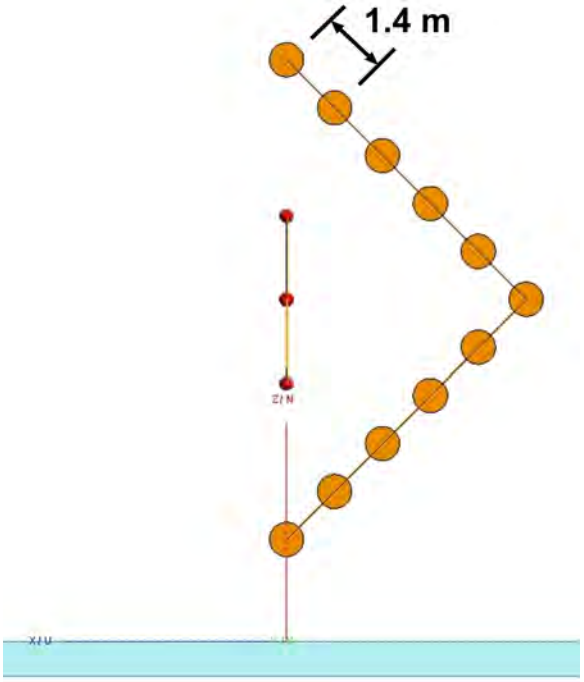

Figure 4.36: Side view of equally spaced 90° full corner reflector with the wires connected behind the antenna elements. Cross section of the side view of a 90° full corner reflector with the reflector wires equally spaced in the simulation model, wire cross sections are exaggerated.

Over an infinite PEC ground-plane the 90° full corner wire reflector with equal wire spacing, connected behind the antenna elements, has a forward directivity level of 20 dB with a θ of 60° and a reverse directivity level of 6.4 dB with a θ of 52°, giving a front-to-back ratio of 13.6 dB.

Over an infinite ice and granite ground-plane the 90° full corner wire reflector with equal wire spacing, connected behind the antenna elements, has a forward directivity level of 19.5 dB with a θ of 64° and a reverse directivity level of 6.7 dB with a θ of 56.1°, giving a front-to-back ratio of 12.8 dB. The comparison of ground-plane results are shown on the polar plot in figure 4.38, the blue plot

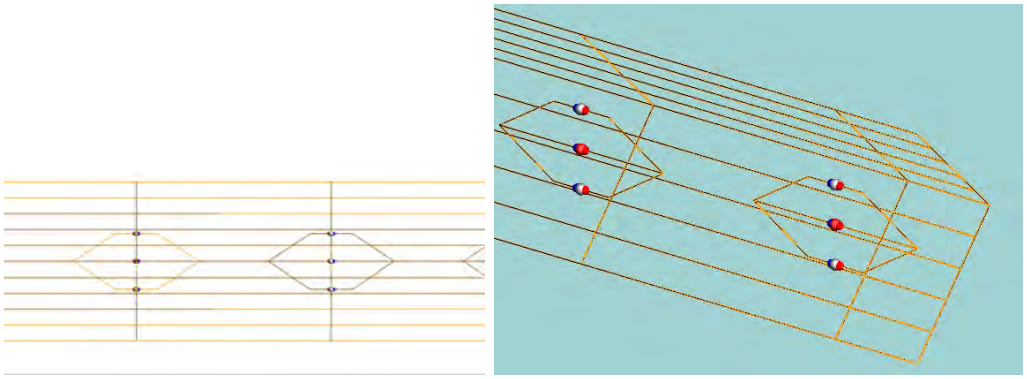

Figure 4.37: (Left) back view and (right) ISO view of a 90° full corner reflector with the wires equally spaced and connected behind the antenna elements. Back and ISO view of a 90° full corner reflector with the reflector wires equally spaced in the simulation model.

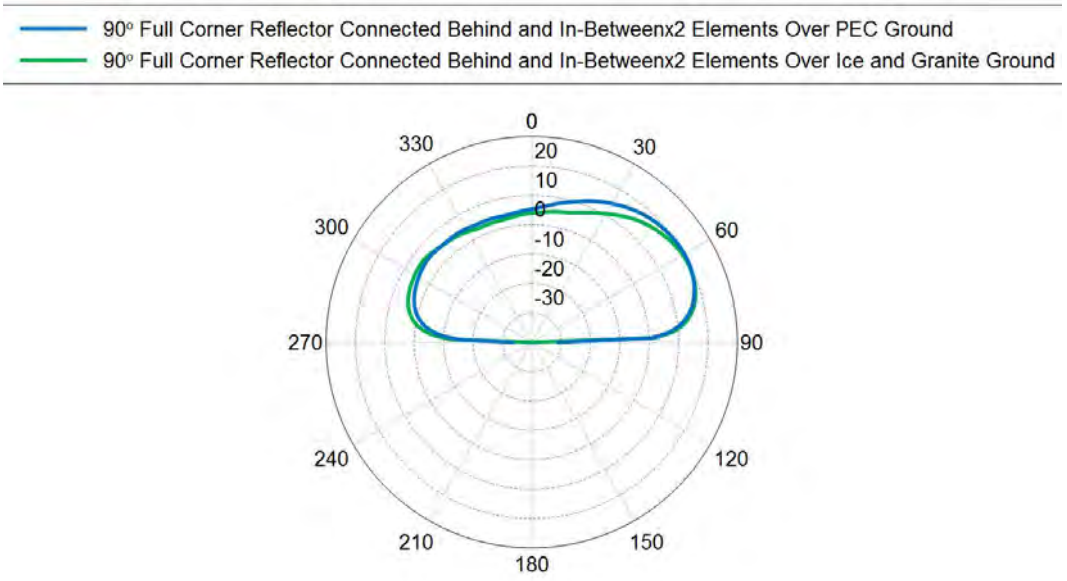

Figure 4.38: Directivity simulation results of the 90° full corner reflector with the reflector wires equally spaced from each other and connected behind the antenna elements. The blue plot is the simulation model over an infinite PEC ground-plane while the green plot is the same model over an infinite ice and granite ground-plane.

is over the infinite PEC ground-plane while the green plot is the same model over an infinite ice and granite ground-plane. The angular axis shows the θ angles, the plot is taken at the plane cut of $\phi = 0°$ and the directivity levels are in dB on the radial axis.

The front-to-back decreases by 1.2 dB over the PEC ground-plane when com-

pared to the previous section. While the PEC compared to ice and granite ground-plane have the lowest forward directivity level and the hight reverse directivity level of all the 90° full corner wire reflector set-ups simulated.

4.3.2.5 Summary of Full Corner Reflector Results

Similar to the half reflectors, the 90° full corner wire reflectors are summarised in this sections. First in table 4.3 for the different models over an infinite PEC ground-plane and then in table 4.4 for the same models over an infinite granite ground-plane layer with a 1 m thick layer of ice at -1°C. It is important to note that all angles in tables 4.3 and 4.4 are taken from the zenith.

Table 4.3: Simulation results of full-scale SuperDARN radar array with a 90° full corner reflector over an infinite PEC ground.

Model	**Front Directivity and Angle**	**Back Directivity and Angle**	**Front-to -Back Ratio**
·Wire corner reflector (full) ·Connected behind elements	20 dB 60°	5.2 dB 50.4°	14.8 dB
·Wire corner reflector (full) ·Connected behind elements and in-between	19.9 dB 60°	5.2 dB 50.4°	14.7 dB
·Wire corner reflector (full) ·Connected behind elements and in-between x 2	20 dB 60°	5.19 dB 49.8°	14.8 dB
·Wire corner reflector (full) ·Connected behind elements ·Equal wire spacing	20 dB 60°	6.4 dB 52°	13.6 dB

Table 4.4: Simulation results of full-scale SuperDARN radar array with a 90° full corner reflector over an infinite ice and granite ground.

Model	Front Directivity and Angle	Back Directivity and Angle	Front-to-Back Ratio
·Wire corner reflector (full) ·Connected behind elements	19.5 dB 64°	6.2 dB 54.1°	13.3 dB
·Wire corner reflector (full) ·Connected behind elements and in-between	19.5 dB 64°	6.2 dB 54°	13.3 dB
·Wire corner reflector (full) ·Connected behind elements and in-between x 2	19.5 dB 64°	6.2 dB 54°	13.3 dB
·Wire corner reflector (full) ·Connected behind elements ·Equal wire spacing	19.5 dB 64°	6.7 dB 56.1°	12.8 dB

4.3.2.6 Discussion

As was seen from the polar plots in figures 4.31, 4.33, 4.35 and 4.38 of the results in section 4.3.2, in all the simulations run over both the PEC ground-plane and the ice and granite ground-plane, the front-to-back ratio is greatly improved by replacing the 90° half corner reflector with a 90° full corner reflector.

In section 4.3.1 the largest difference between the results of a model over an infinite PEC ground-plane versus those over an infinite ice and granite ground-plane occurred directly above the antenna element. While this is still the case, the difference now, between the two ground-planes, above the antenna element has been reduced significantly. Indicating that, with a 90° full corner reflector, the EM waves are not reflected directly back into the ground-plane but rather that the EM waves are better reflected outwards towards the front of the array and the energy does not dissipate through the ice and granite ground-plane, directly below the antenna element. This is confirmed by the 4° decrease in the forward directivity's θ indicating that most of the EM waves are being reflected in the forward direction.

With respect to the two different ground-planes, the forward directivity levels only decrease by around 0.5 dB for each model while the reverse directivity levels increase by around 1 dB from PEC to ice and granite ground. The most significant improvement that was extracted from this section was the sizeable increase in the front-to-back ratio. In section 4.3.1 the highest front-to-back ratio was 6.4 dB, while in section 4.3.2 the highest front-to-back ratio was

13.3 dB, over an infinite ice and granite ground-plane.

The simulations run in sections 4.3.1 and 4.3.2 are only of the ideal ground models. With both the PEC, and ice and granite ground-planes being infinitely big. The next section will look at the SuparDARN array over a more realistic ground model.

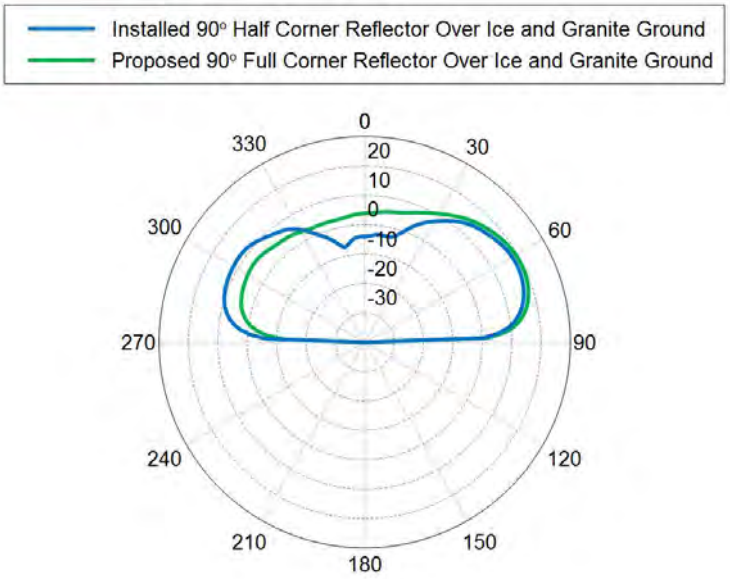

Figure 4.39: Comparison of the simulation results between the installed 90° half corner reflector (blue) versus the proposed 90° full corner reflector (green). Directivity in dB is on the radial axis while θ is on the angular axis. With the front of the radar point towards $\phi = 90°$ on the axis and the results plotted on the plane cut at $\phi = 0°$.

Figure 4.39 is a polar plot showing the change in directivity between the installed 90° half corner reflector (blue) and the proposed 90° full corner reflector (green) over an infinite ice and granite ground-plane. From this figure the improvement in backwards directivity is clearly shown with the proposed 90° full corner reflector having a maximum backwards directivity of 6.2 dB at $\theta = 54.1°$ and the currently installed 90° half corner reflector having a maximum backwards directivity of 11.7 dB at $\theta = 55.7°$.

4.4 Realistic Ground Model Simulation

The Centre for High Performance Computing (CHPC), South Africa, provides computational resources to many institutes for use in conjunction with software

such as Altair Hyperworks FEKO when standard computing resources are not large enough to find a solution to a model [32].

With the use of Google Earth's satellite images and CHPC's computing resources, a more realistic ice and granite cliff and an infinitely big ice ground plane ground-plane was defined, shown in figures 2.6 and 2.7, to be able to run with the full-scale SuperDARN radar array as shown in figures 4.40, 4.41, 4.42 and 4.43.

4.4.1 Realistic Ground Model Simulation Set-up

The ground-plane shown in figures 4.40 - 4.43, of the realistic ground plane layout from various views, were constructed by mapping out points on the cliff face at SANAE IV base using Google Earth and then those points were plotted in FEKO to construct a conducting surface. Once the conducting surface had been defined the correct placement of the part was necessary to model a cliff 100 m deep. The cliff however, is not made from one material but two, ice and granite. The original surface part was copied and both conducting surfaces were lowered to the middle of the respective material regions, with the top conducting surface being defined as ice at -1°C and the bottom conducting surface as granite, similar to that done in section 4.3. The conducting surfaces were then defined as having a dielectric coating of 0.5 m thick ice for the top surface and 50 m thick granite for the bottom surface. The reason for placing the face in the middle of their respective regions is because when a layered dielectric or coating is applied to a face in FEKO, FEKO coats the face with equal thickness on each side of the face [26]. As is shown in figure 4.44. The entire model was then defined over an infinitely wide and thick ice ground to represent the ice shelf.

The antenna elements are exactly the same as the ones used in the simulations for section 4.3, shown in figure 4.1, and the same 90° half corner wire reflector as seen in figure 4.9. While the proposed 90° full corner wire reflector realistic ground simulations uses the reflector wire spacing dimensions shown in figure 4.25. This simulation, makes use of Altair FEKO's RL-GO solver due to the huge size of the two ground conducting surfaces. The overall simulation model is solved using the MoM solver and the two ground conducting surfaces have their locally defined solver set to RL-GO.

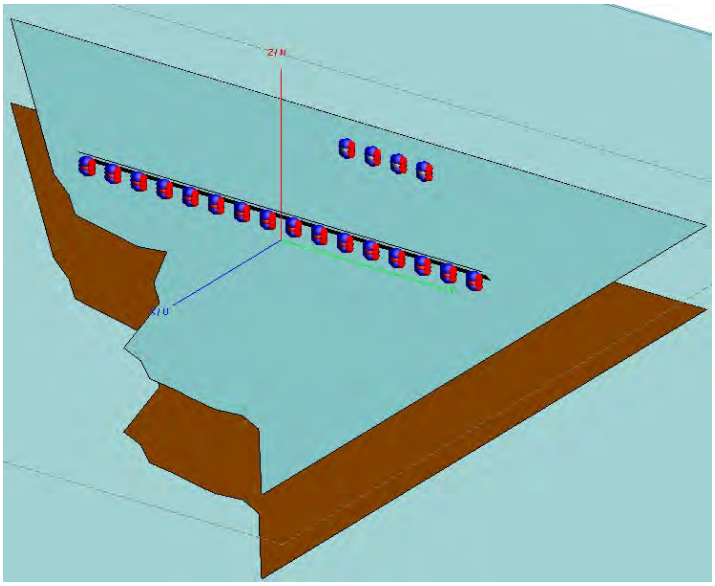

Figure 4.40: Close up ISO view of the currently installed SuperDARN radar array over a more realistic ground-plane. The two conducting surfaces used for the granite cliff (brown) and the ice layer on top of the granite cliff (light blue) shown in the figure.

The image taken from FEKO shown in figure 4.40 is a close up ISO view of the two surfaces which were defined by mapping out points at the SANAE IV base using Google Earth and then plotting these point in FEKO to construct conducting surfaces that would be used for the realistic ground-plane.

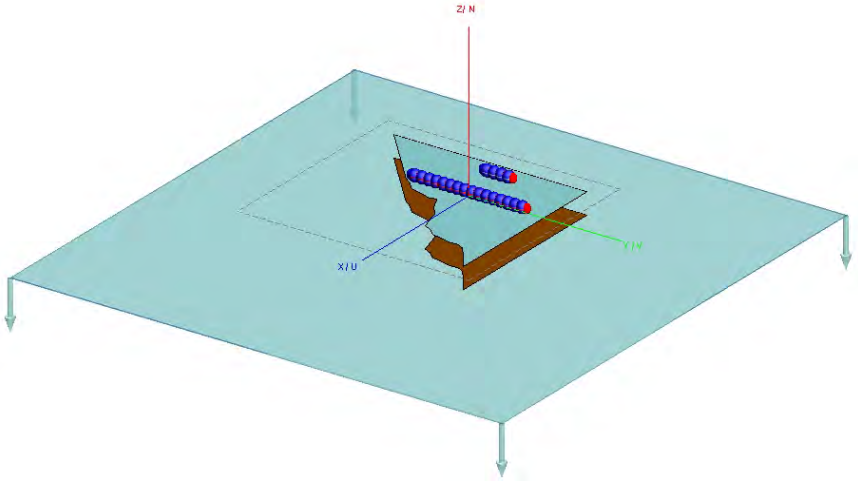

Figure 4.41: Zoomed out ISO view of the currently installed SuperDARN radar array over a more realistic ground-plane. The full ground-plane configuration is shown in this figure.

From figure 4.41 the full ground-plane set-up is shown, starting with a 1 m layer of ice at -1°C at the top, then a cliff made of granite 100 m deep and finally an infinite ice ground-plane at the bottom to represent the ice shelf.

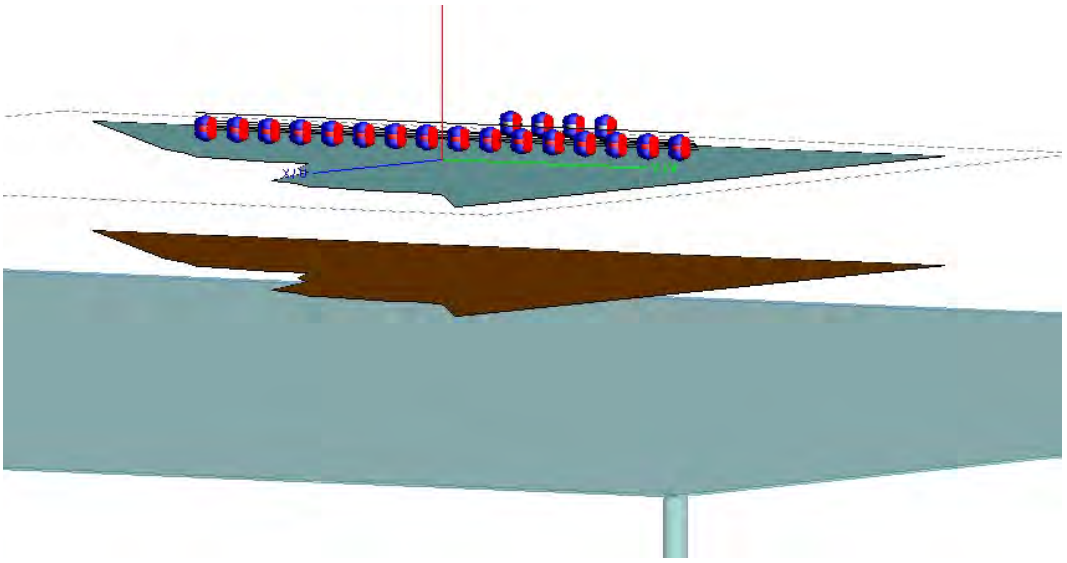

Figure 4.42: ISO view showing the placement of the ground conducting surfaces. In this FEKO image the two surfaces which define the ice layer on top of the granite (top) and granite cliff (bottom). Here the placement of the two conducting surfaces making up the configuration of the cliff face are more clearly shown.

In figure 4.42 the placement of the conducting surfaces is more clearly shown, with ice surface placed 0.5 m below the SuperDARN radar array to create a 1 m thick layer of ice while the granite surface was placed 51 m below the radar to create the 100 m cliff face.

Figure 4.43: Top view of the realistic ground in FEKO. Here the profile of the surface which makes up the cliff face can be seen more clearly.

Using Google Earth, the profile of the cliff face was defined and modelled in Altair Hyperworks FEKO which is shown in figure 4.43, with the front of the radar pointing to the right of the figure.

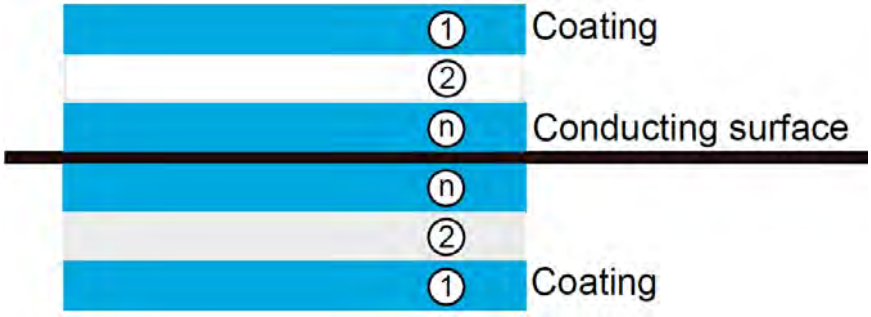

Figure 4.44: Layout indicating how coating is applied to a conducting surface in Altair Hyperworks FEKO [26]. The figure shows how Altair Hyperworks FEKO applies coating layers by mirroring the layers along the plane defined by a conducting surface.

Figure 4.44 shows that it is possible to apply more than one coating layer to a conducting surface with this image showing how Altair FEKO applies the coating layer to both sides of the conducting surface, hence the reason for placing the ground face in the middle of their respective material regions.

Two simulations were running using CHPC's computing resources for the realistic ground model, (1) the currently installed 90° half corner reflector and

(2) the proposed 90° full corner reflector which will be discussed in the next sections.

4.4.2 Realistic Ground Model Simulation Results of 90° Half Corner Reflector

This section considers the simulation results over a realistic ground-plane of the currently installed SuperDARN radar with the 90° half corner reflector located at the SANAE IV base. The figures of results are shown in two forms, namely, in 3D total far-field directivity plots and various polar plots taken at different ϕ plane cuts.

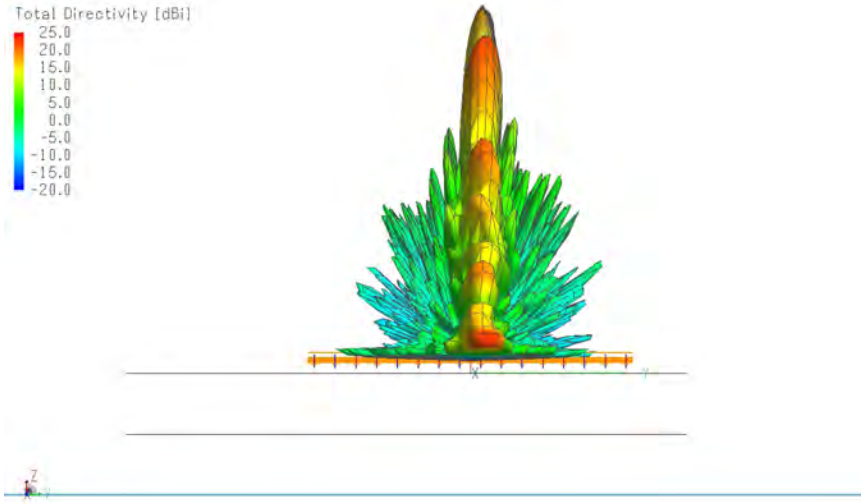

Figure 4.45: Front view of the currently installed 90° half corner reflector over a realistic ice and granite ground-plane. 3D Total far-field directivity results at 12.75 MHz of the SuperDARN radar with a 90° half corner reflector over a realistic ice and granite ground.

Figure 4.45 shows the 3D total far-field directivity simulation results from the front of the currently installed SuperDARN radar configuration with the 90° half corner reflector over the realistic ground-plane set-up.

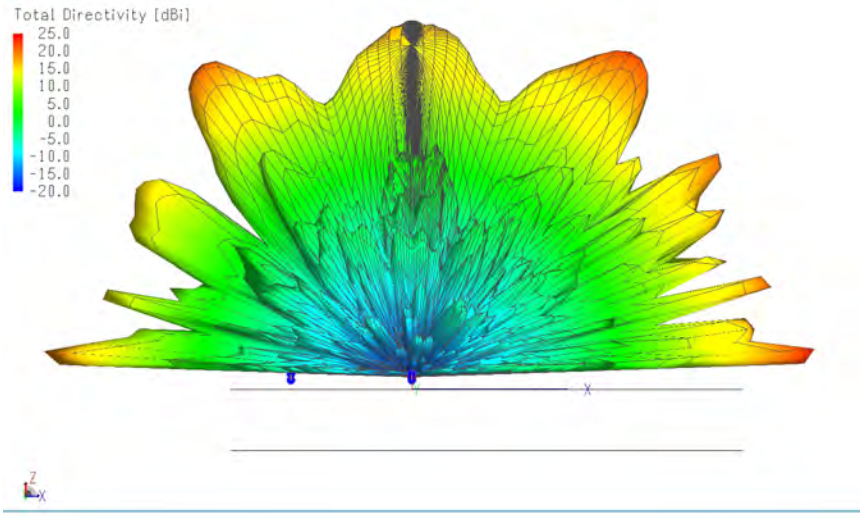

Figure 4.46: Left view of the currently installed 90° half corner reflector over a realistic ice and granite ground-plane. 3D Total far-field directivity results at 12.75 MHz of the SuperDARN radar with a 90° half corner reflector.

In figure 4.46, with the front of the radar pointing to the right of the figure, it can clearly be seen that the currently installed 90° half corner reflector does little to hinder EM wave propagation towards the back of the radar for the realistic ground model simulation.

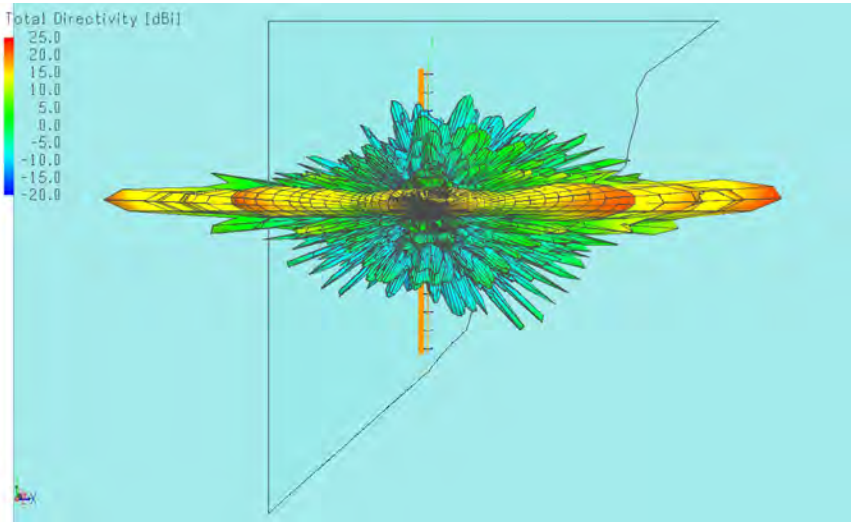

Figure 4.47: Top view of the currently installed 90° half corner reflector over a realistic ice and granite ground-plane. 3D Total far-field directivity results at 12.75 MHz of the SuperDARN radar with a 90° half corner reflector.

Figure 4.47 shows the 3D total far-field directivity simulation results from the top of the currently installed SuperDARN radar configuration with the 90° half corner reflector over the realistic ground-plane set-up. The front of the radar points to the right of the figure, where an offset front the centre in the azimuth plane can be seen.

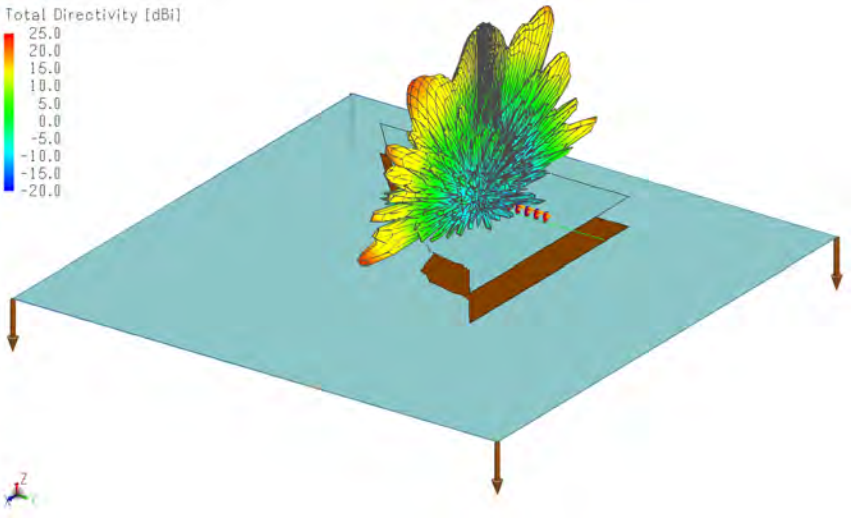

Figure 4.48: ISO view of the currently installed 90° half corner reflector over a realistic ice and granite ground-plane. 3D Total far-field directivity results at 12.75 MHz of the SuperDARN radar with a 90° half corner reflector over a realistic ice and granite ground, with the front of the array pointing to the bottom left of the figure.

An ISO view of the 3D total far-field directivity simulation results of the currently installed SuperDARN radar configuration with the 90° half corner reflector is shown in figure 4.48. With the radar over the realistic ground-plane configuration and the front of the radar pointing to the bottom left corner of the figure.

Considering figure 4.47, it can bee seen that the forward directivity is now offset from the centre, i.e. the maximum level of directivity no longer lies along the $\phi = 0°$ plane, shown on the polar plot in figure 4.49.

At $\phi = 0°$ the maximum backwards directivity levels is 17.4 dB at $\theta = 34°$. The forward directivity has two levels to consider when considering figure 4.49, the first level is 23.2 dB at $\theta = 86°$ and the second level is 22 dB at $\theta = 36°$, with both of these directivity levels lying along the $\phi = 2°$ plane. This gives a front-to-back ratio of 5.8 dB when considering the first forward directivity level of interest and a front-to-back ratio of 4.6 dB when considering the second forward directivity level of interest.

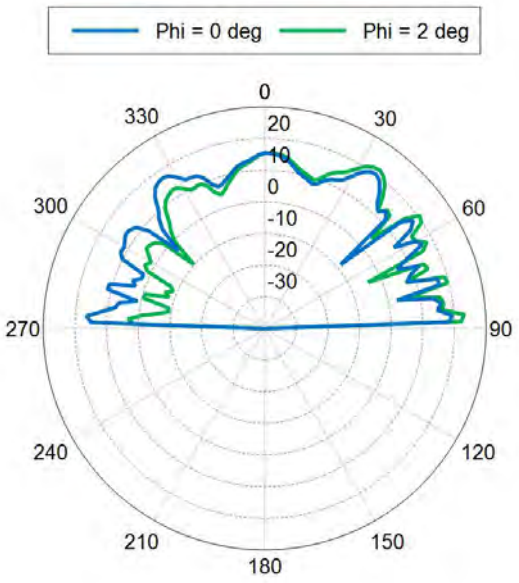

Figure 4.49: Simulation results of the 90° half corner reflector installed at the SANAE IV base, over a realistic ground. As shown in figure 4.47 the maximum forward directivity has been offset from the $\phi = 0°$ plane. The blue plot shows the maximum backwards directivity level lies on the $\phi = 0°$ plane, while the green plot shows the maximum forward directivity level lies on the $\phi = 2°$ plane.

Neither of these results lie along the expected $\theta = 60°$ angle and the results in figure 4.49 reveal that the majority of the forward power is being directed, either, roughly straight out along the horizon or almost directly up to the zenith.

When the realistic ground-plane model is compared to those of the infinite PEC, and ice and granite ground-plane model, as shown in figure 4.50, the change in directivity pattern can more clearly be seen.

The offset of $\phi = 2°$ and unexpected θ in the forward direction can be attributed to the proximity of the SuparDARN array to the cliff face. The sharp drop in the cliff ground-plane down to the ice shelf, 100 m below, indicate that the array's EM signals have no or little ground-plane surface to reflect off of before travelling into the far-field region of the array. This in conjunction with the nonparallel cliff surface in front of the array before the 100 m drop would account for the $\phi = 2°$ offset in the forward direction.

By simulating a more realistic ground-plane set-up with CHPC's computing resources, it was able to be determined that the expected directivity pattern and angle of elevation, as were seen with the infinite ground-plane simulations, were

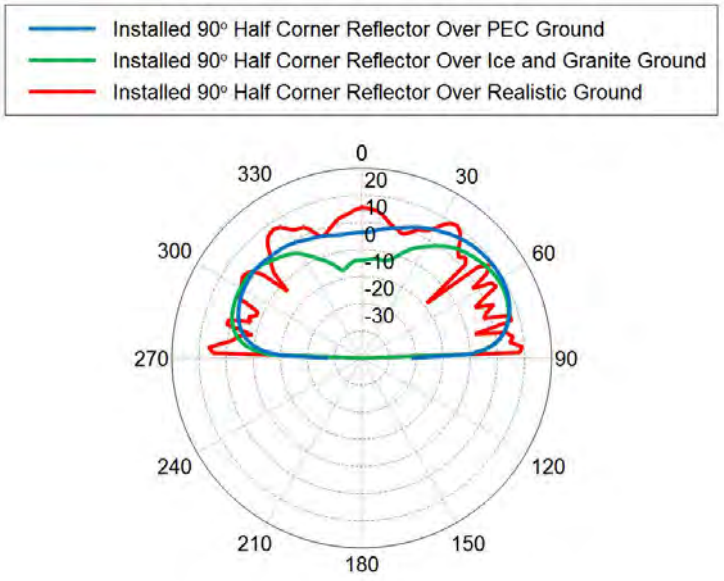

Figure 4.50: Directivity comparison plot of the currently installed 90° half corner reflector over the different ground-plane set-ups. Directivity in dB is on the radial axis while θ is on the angular axis. With the front of the radar point towards $\phi = 90°$ on the axis and the results plotted on the plane cut at $\phi = 0°$.

not the case for the realistic ground-plane set-up. By using CHPC's computing resources a more accurate directivity characterisation of the SuperDARN located at the SANAE IV base was able to be achieved.

4.4.3 Realistic Ground Model Simulation Results of Proposed 90° Full Corner Reflector

The simulation results of proposed 90° full corner reflector are considered in this section over the realistic ground configuration. The figures of results are shown in 3D total far-field directivity plots and various polar plots taken at different ϕ plane cuts.

The 3D total far-field directivity simulation results of the proposed 90° full corner reflector are shown from the front view in figure 4.51.

With the front of the radar pointing to the right of figure 4.52, the proposed 90° full corner reflector clearly improves the EM wave propagation hindrance towards the back of the radar.

Similar to the results from figure 4.47, figure 4.53 clearly shows the offset of the forward directivity's maximum levels. Which lies on the $\phi = 2°$ plane,

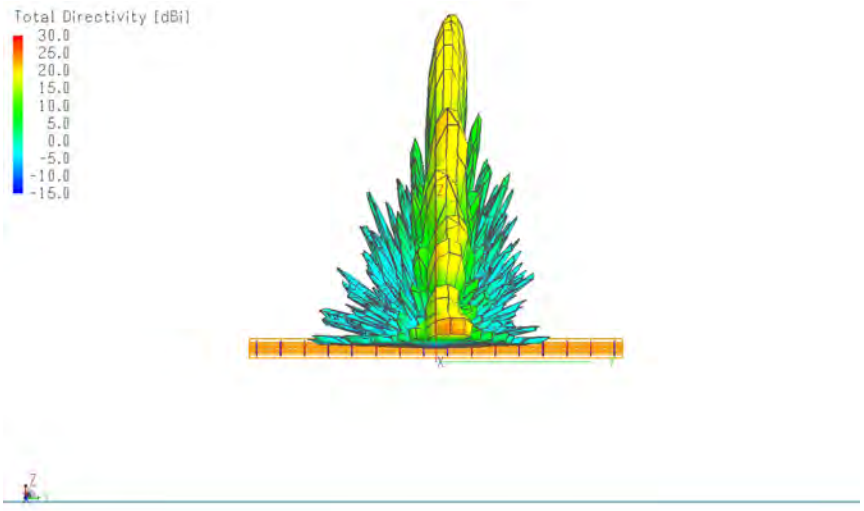

Figure 4.51: Front view of the proposed 90° full corner reflector over a realistic ice and granite ground-plane. 3D Total far-field directivity results at 12.75 MHz of the SuperDARN radar with a 90° full corner reflector over a realistic ice and granite ground.

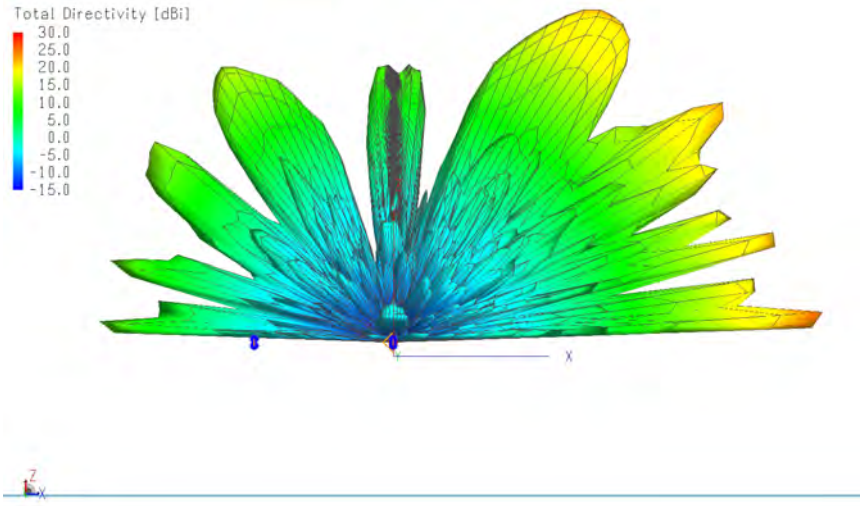

Figure 4.52: Left view of the proposed 90° full corner reflector over a realistic ice and granite ground-plane. 3D Total far-field directivity results at 12.75 MHz of the SuperDARN radar with a 90° full corner reflector over a realistic ice and granite ground.

while the maximum backwards directivity level still lies on the $\phi = 0°$ plane.

An ISO view of the 3D total far-field directivity simulation results of the proposed 90° full corner reflector is shown in figure 4.54. With the radar over the realistic ground-plane configuration and the front of the radar pointing to

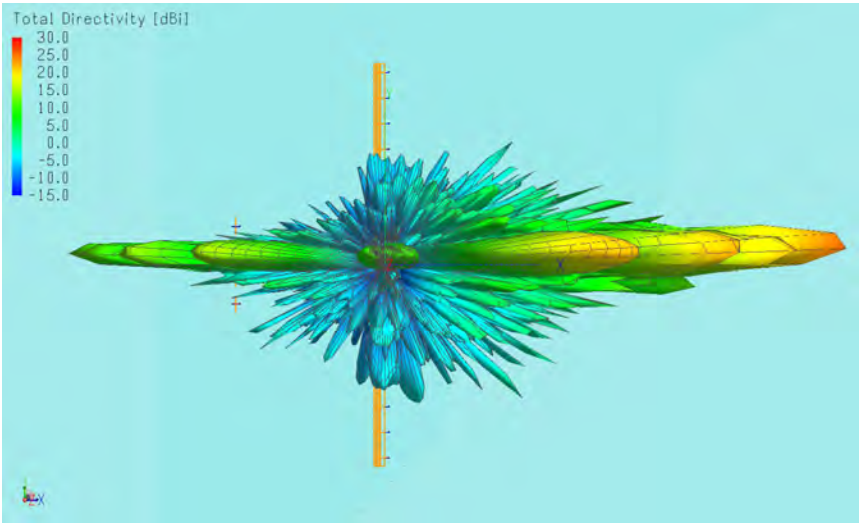

Figure 4.53: Top view of the proposed 90° full corner reflector over a realistic ice and granite ground-plane. 3D Total far-field directivity results at 12.75 MHz of the SuperDARN radar with a 90° full corner reflector over a realistic ice and granite ground, with the front of the array pointing to the right of the figure.

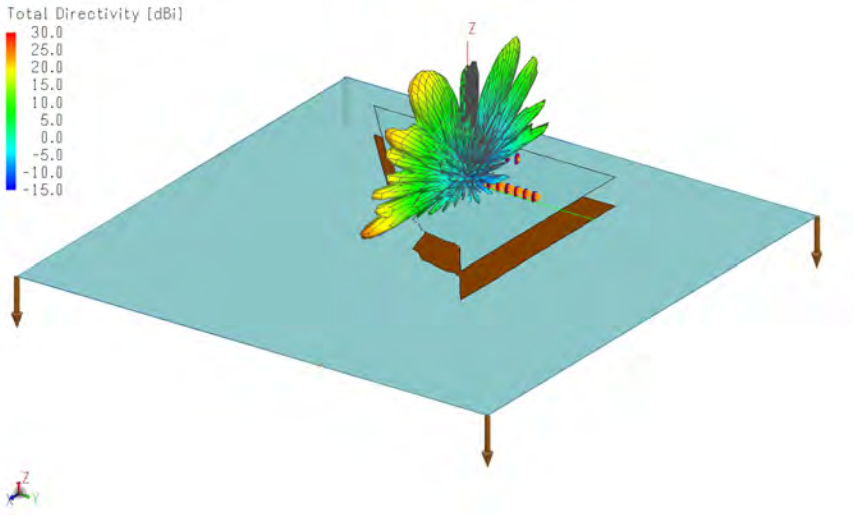

Figure 4.54: ISO view of the proposed 90° full corner reflector over a realistic ice and granite ground-plane. 3D Total far-field directivity results at 12.75 MHz of the SuperDARN radar with a 90° full corner reflector over a realistic ice and granite ground, with the front of the array pointing to the bottom left of the figure.

the bottom left corner of the figure.

These results reaffirm that the proximity of the SuperDARN radar to the cliff face causes the EM signals to have little or no ground-plane to reflect off of before the drop off to te ice shelf and the nonparallel cliff surface causes the

forward directivity to be offset by 2°. The results also reaffirm that a 90° full corner reflector will improve the hindrance of EM wave propagation in the reverse direction as the backwards directivity level decreases by 5.1 dB with a 90° full corner reflector.

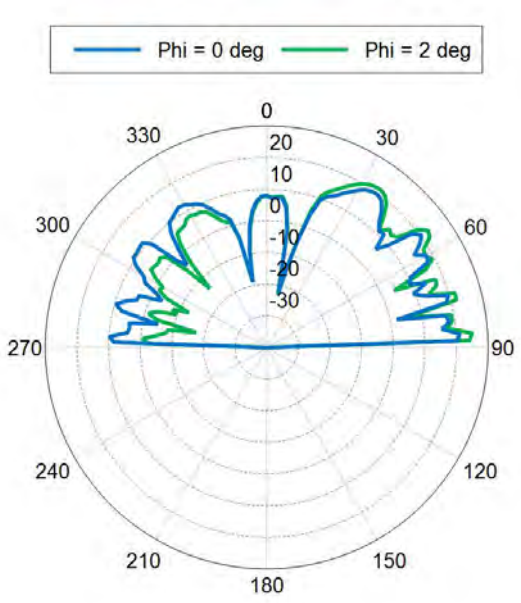

Figure 4.55: Simulation results of the proposed 90° half corner reflector over a realistic ground. In figure 4.53 the maximum forward directivity has been offset from the $\phi = 0°$ plane. The blue plot shows the maximum backwards directivity level lies on the $\phi = 0°$ plane, while the green plot shows the maximum forward directivity level lies on the $\phi = 2°$ plane.

The forward directivity has two levels to consider when examining figure 4.55, the first level is 25.2 dB at $\theta = 86°$ and the second level is 23 dB at $\theta = 54.1°$, with both of these directivity levels lying along the $\phi = 2°$ plane. While maximum backwards directivity, which lies on the $\phi = 0°$ plane, is 12.3 dB at $\theta = 32.2°$. This gives a front-to-back ratio of 12.9 dB when considering the first forward directivity level of interest and a front-to-back ratio of 10.7 dB when considering the second forward directivity level of interest.

4.4.4 Realistic Ground Model Simulation Discussion

After simulations of the ideal conditions were run, a simulation with a more realistic ground-plane set-up as in Antarctica at the SANAE IV base was constructed. Two models were simulated over the realistic ground plane configuration, the first was the currently installed SuperDARN radar with the

90° half corner wire reflector and the second was the SuperDARN radar with the proposed 90° full corner wire reflector. From the top views shown in figures 4.47 and 4.53, an offset from the centre by $\phi = 2°$ was seen in the 3D total far-field simulation results. This offset is due to close proximity of the radar to the cliff face and the cliff face profile in front of the radar.

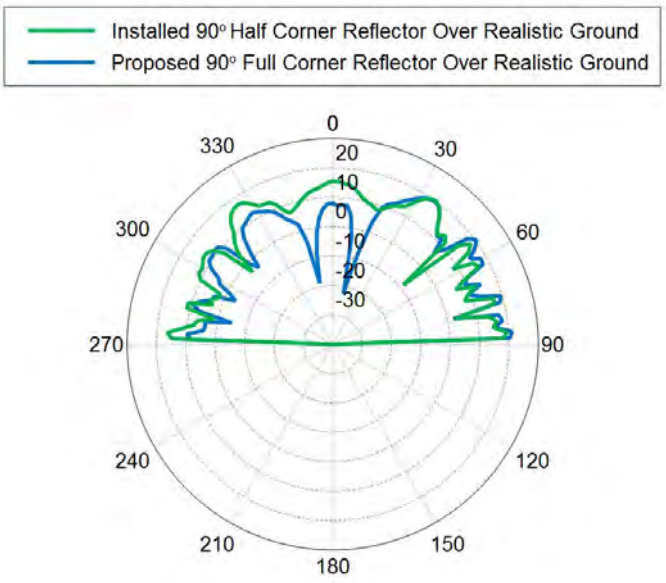

Figure 4.56: Simulation results of the currently installed 90° half corner reflector (green) versus proposed 90° full corner reflector (blue) over a realistic ground at $\phi = 0°$ plane cut. Directivity in dB is on the radial axis while θ is on the angular axis. With the front of the radar point towards $\phi = 90°$ on the axis.

Figure 4.56 clearly shows that both models have maximum backwards directivity levels along the $\phi = 0°$ plane over the realistic ground-plane configuration. With the half corner reflector model having a maximum backwards directivity of 17.4 dB at $\theta = 34°$ and the proposed full corner reflector model having a maximum backwards directivity of 12.3 dB at $\theta = 32.2°$.

Figure 4.57 shows that both models have a maximum forward directivity levels at $\theta = 86°$ and $\phi = 2°$, with the half corner reflector's being 23.2345 dB and the proposed full corner reflector's being 25.1557 dB. Using these two forward directivity results the currently installed 90° half corner reflector model had a front-to-back ratio of 5.8345 dB, while the proposed 90° full corner reflector model had a front-to-back ratio of 12.8557 dB with the realistic ground-plane configuration. This $\theta = 86°$ angle indicates that the EM waves propagating

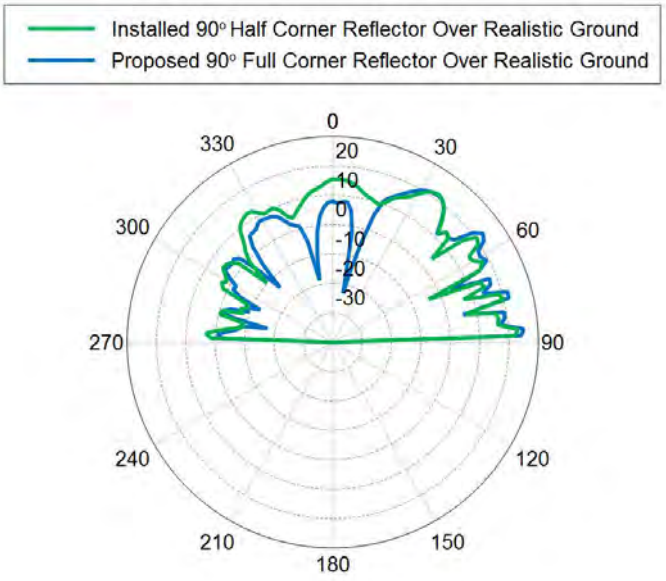

Figure 4.57: Simulation results of the currently installed 90° half corner reflector (green) versus proposed 90° full corner reflector (blue) over a realistic ground at $\phi = 2°$ plane cut. θ is plotted on the angular axis and directivity in dB is on the radial axis. With the front of the radar point towards $\phi = 90°$ on the axis.

from the radar in the forward direction have little to no ground plane to reflect off of before the 100 m cliff drop to the ice shelf.

Each simulation model had one more forward directivity level that was considered in the $\phi = 2°$ plane, for the currently installed 90° half corner reflector model it was 22 dB at $\theta = 36°$ giving a front-to-back ratio of 4.5 dB. While, for the proposed 90° full corner reflector model it was 23 dB at $\theta = 54.1°$ giving a front-to-back ratio of 10.7 dB. Considering these results, the proposed 90° full corner reflector improves the front-to-back ratio of the radar from 4.5 dB to 10.7 dB while also improving the θ angle at which the EM waves propagate in the forward direction.

4.5 Conclusion

This chapter has looked at the full-scale SuperDARN radar simulation model with various 90° half and full corner wire reflector set-ups over two different ground-planes, namely, PEC and a combination of ice layered on granite. With the results from section 4.3.1 of the 90° half corner wire reflectors, it was shown that this design can be altered to improve the amount of EM wave propagation in the forward direction and in-turn improving the front-to-back ratio. The 90° half corner wire reflector was replaced with a 90° full corner

wire reflector in section 4.3.2 and it was shown that this corner reflector set-up significantly improves the SuperDARN radar array's front-to-back ratio, from 6.4 dB with the 90° half corner wire reflector to 13.3 dB with a 90° full corner wire reflector. With a specific set-up being proposed as the suggested upgrade to the system. Lastly, the currently installed 90° half corner wire reflector and the proposed 90° full corner wire reflector were run over a more realistic ground-plane configurations with the use of CHPC's computing resources. The 90° half corner wire reflector had a front-to-back ratio of 4.5 dB over the realistic ground while the proposed 90° full corner wire reflector improved the front-to-back ratio to 10.7 dB. The currently installed 90° half corner wire reflector causes the maximum forward directivity of the radar to have an elevation angle of 54° and an azimuth angle of 2°, while, the proposed 90° full corner wire reflector causes the maximum forward directivity of the radar to have an elevation angle of 35.9° and an azimuth angle of 2°. A summary of the most significant results are shown in table 4.5 with the directivity angles measured from the zenith. The proposed 90° full corner reflector would require a total length of 3317 m reflector wiring to construct, this number could be reduced if the currently installed 90° half corner reflector wires are salvageable.

Table 4.5: Most significant simulation results.

Model	**Front Directivity and Angles**	**Back Directivity and Angles**	**Front-to -Back Ratio**
·**Wire corner reflector (half)** ·**Installed set-up** ·**Ice and granite ground**	18.1 dB $\theta = 62°$ $\phi = 0°$	11.7 dB $\theta = 55.7°$ $\phi = 0°$	6.4 dB
·**Proposed wire corner reflector (full)** ·**Connected behind elements** ·**Ice and granite ground**	19.5 dB $\theta = 64°$ $\phi = 0°$	6.2 dB $\theta = 54.1°$ $\phi = 0°$	13.3 dB
·**Wire corner reflector (half)** ·**Installed set-up** ·**Realistic ground**	22 dB $\theta = 36°$ $\phi = 2°$	17.4 dB $\theta = 34°$ $\phi = 0°$	4.5 dB
·**Proposed wire corner reflector (full)** ·**Connected behind elements** ·**Realistic ground**	23 dB $\theta = 54.1°$ $\phi = 2°$	12.3 dB $\theta = 32.2°$ $\phi = 0°$	10.7 dB

Chapter 5

Discussion and Conclusion

This final chapter is the concluding chapter of this project, discussing all the work done and results obtained throughout the project, of the scale model and full-scale model. It then concludes all the work done during this project and discusses a few recommendations on the full-scale SuperDARN radar as to the proposed 90° full corner reflector and, if every, on-site measurements for characterisation are to be done.

5.1 Scale Model Discussion

In chapter 3 the single and three element 1:100 scale model of the full-scale SuperDARN radar antenna array was designed and an evaluated to determine whether or not the Altair Hyperworks FEKO EM simulation solver software would be sufficiently accurate so that it could be used to evaluate the full-scale radar. The models had some design compromises, with the major one being a sleeve balun was used to replace the 1250:50 impedance transformer used in the full-scale model.

Though the measured results were somewhat different from the simulated results, the overall comparisons of results were acceptable. With the average RMSE difference between measured and simulated total directivity being 1.4 dB for the scale single element and 2.09 dB for the scale three element models. The general shapes of the comparisons of the total far-field directivity were very similar in the polar plots in chapter 3, with the various excitation and load set-ups, for the single and three element scale models.

In these polar plots, the direction of the main beam is located between 0° - 90° and this is where the measured results most agree with the simulated results. This is significant, in that, this is the region of most interest when the simulated results of the full-scale model are to be looked at, as this is the region where the full-scale SuperDARN radar forward beam is pointing. In the region between

90° - 180° the difference in results becomes more prominent, which can be attributed to the 90° wire half corner reflector and how it functions to restrict the flow of EM waves. Between 180° - 360° is the greatest discrepancy between the measured versus simulated results, in this region the model is connected to the measurement mount, covered in absorber foam, via a metallic stand. Though the metallic stand was included in the simulation models, it does add more EM wave conduction in this region and the absorber foam hinders EM waves in this region, though the relation between conduction and hindrance are not proportional. The region between 180° - 360° is of least importance when the full-scale model is to be evaluated as this is the region which is fully enclosed by an ice and granite ground-plane at the SANAE IV base in Antarctica.

With the full sets of total far-field directivity measured and simulated results acquired, it was then stated that the results achieved using the FEKO software would be used with confidence and could be used to evaluate the full-scale SuperDARN radar model as the RMSE of less than 3 dB lies well within the stated confidence level of 8-9 dB.

5.2 Full-Scale Model Discussion

Chapter 4 dealt with the simulation of the full-scale model. Comparing the same SuperDARN radar model with various 90° half and full corner reflectors over two different ground-plane, namely, an infinite PEC ground-plane and an infinite granite ground-plane cover by a 1 m thick layer of ice at -1°C.

From the results of the 90° half corner reflector, it was seen that the 90° half corner reflector provides the necessary 30° angle of elevation of the forward directivity with an adequate level of directivity in the forward direction but the 90° half corner reflector does little to hinder the level of reverse directivity.

Theoretically, this issue should be solved by changing the 90° half corner reflector to a 90° full corner reflector, to which, the results from the simulation of various 90° full corner reflector substantiate this claim. The 90° full corner reflector causes the forward directivity to increase by around 1.5 dB, the reverse directivity to decrease by around 5.5 dB and the angle of elevation to decrease by 2° when compared to its respective 90° half corner reflector counterpart.

Various other simulations were also run on both the 90° half and full corner reflector. Namely, a plate corner reflector to understand how an ideal 90° plate corner reflector would cause the SuperDARN radar to operate. Two other 60° and 30° full corner reflectors were simulated to determine if a 90° corner reflector would truly be the best corner angle suited for the radar, with the results reaffirming that it is.

5.3 Realistic Ground-Plane Model Discussion

Chapter 4 also considers two corner reflector set-ups modelled over a realistic ground plane using Google Earth, similar to the one at the SANAE IV base, using the Altair Hyperworks FEKO EM solver software and CHPC's computing resources. The ground plane configuration consisted of two conducting surfaces placed in the centre of their respective ice and granite regions, layered with a coating of their respective thickness and their local solver set to RL-GO. An infinitely wide and thick ice ground-plane at -1°C was added to the set-up to represent the ice shelf at the bottom of the cliff.

From the results it was determined that the close proximity of the SuperDARN radar to the cliff face in conjunction with the profile at which the cliff face drops provides little to no ground surface area for the radar's forward beam to reflect off of and causes the forward beam to have an offset of $\phi = 2°$ from the centre. It can also be concluded from the simulation results that the 90° half corner reflector's front-to-back ratio of 4.5 dB can be improved upon by upgrading the half corner reflector to the proposed 90° full corner reflector giving a front-to-back ratio of 10.7 dB over the realistic ground-plane.

5.4 Conclusion

This project set out to determine the array characteristics of the current SuperDARN radar installed at the SANAE IV base. Through the use of common EM practices and terminologies used today a scale model was built to determine whether or not an EM solver software, such as Altair Hyperworks FEKO, would provide results accurate enough to give correct feedback on the full-scale SuperDARN radar. From the measured versus simulated scale model results it was seen that, although the results do differ in some areas, the overall comparison between simulated versus machined proved that the FEKO software could be used to provide an accurate account of the full-scale SuperDARN radar's characteristics. Whilst confirming that the currently installed half-reflector layout is sufficient for the SuperDARN radar array, the FEKO simulations showed that the full 90 degree corner reflectors improves the front-to-back ratio by 6.2 dB.

5.5 Recommendations

From the results in chapter 4 a 90° half corner reflector works well enough for the required operations of the SuperDARN radar but a 90° full corner reflector greatly improves the operations when added to the system. As such, it is suggested, from the work done in this project, the installed 90° half corner reflector be amended with a proposed 90° full corner reflector with the reflector

wires connected behind the antenna elements to increase the surface area which reflects the EM wave propagation. The proposed 90° full corner reflector with the reflector wires connected behind the antenna elements would require a total length 3317 m reflector wiring to construct.

During the earlier stages of this project, it was discussed that a multi-copter could be used to do measurements to characterise the SuperDARN radar on-site at the SANAE IV base. However, due to the regulatory licensing requirements to fly multi-copters and cost and time constraints that compliance with the regulatory requirements would involve, it was decided to replace this concept with one involving modelling the SuperDARN radar in an EM solver such as FEKO. If the idea of using a multi-copter is investigated further, two ESA antenna designs which could be mounted onto the multi-copter can be found in Appendix D.

Appendices

Appendix A

Scale Model Engineering Drawings

The figures in this Appendix are the Engineering drawing used for the manufacturing of the 1:100 scale single and three element models and as discussed in 3.2 all dimensional tolerances in figures A.1 - A.12 are machined to the closest 0.5 mm.

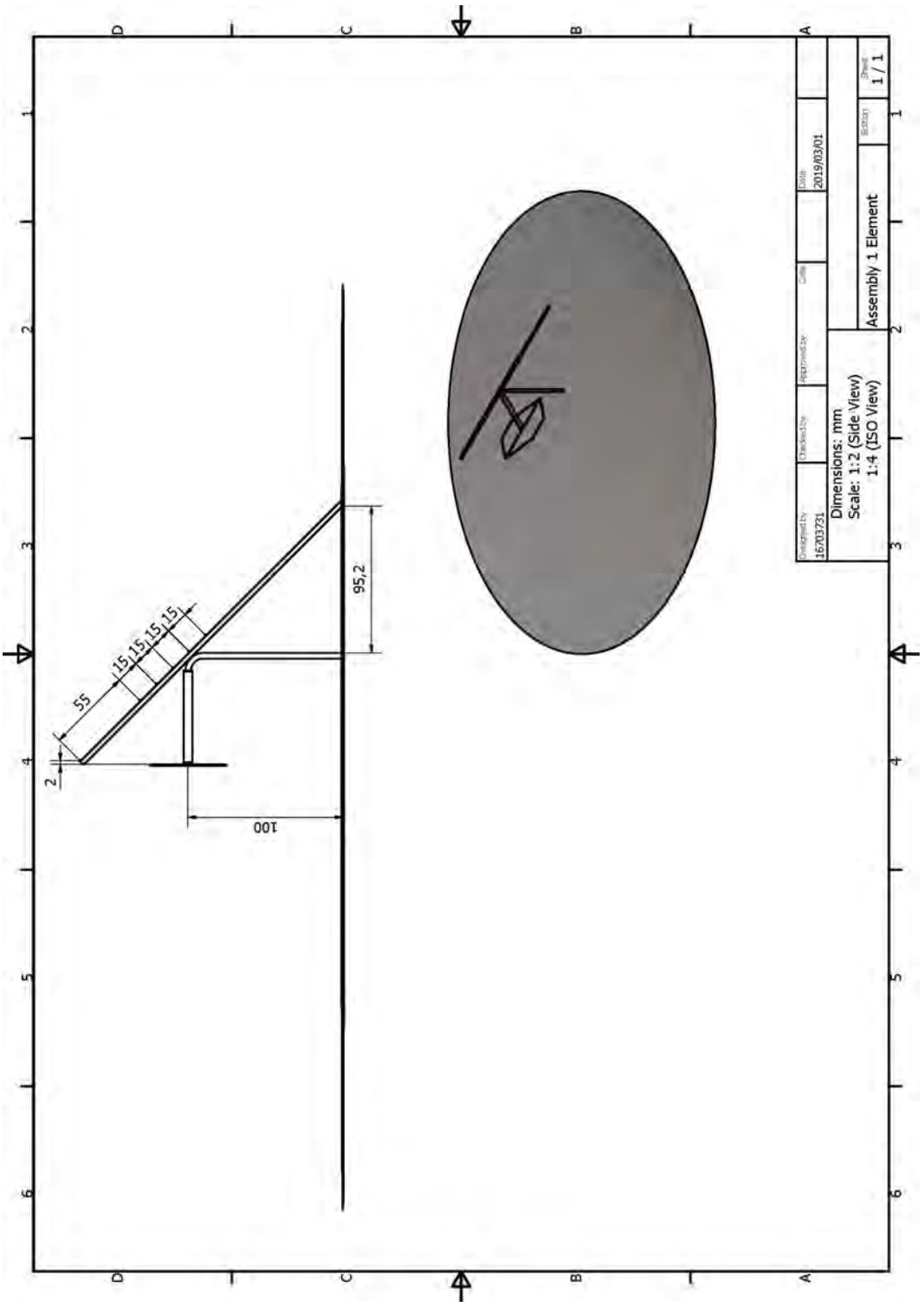

Figure A.1: 1:100 scale single element model assembly drawing. This engineering drawing shows the completed construction of the 1:100 scale single element model.

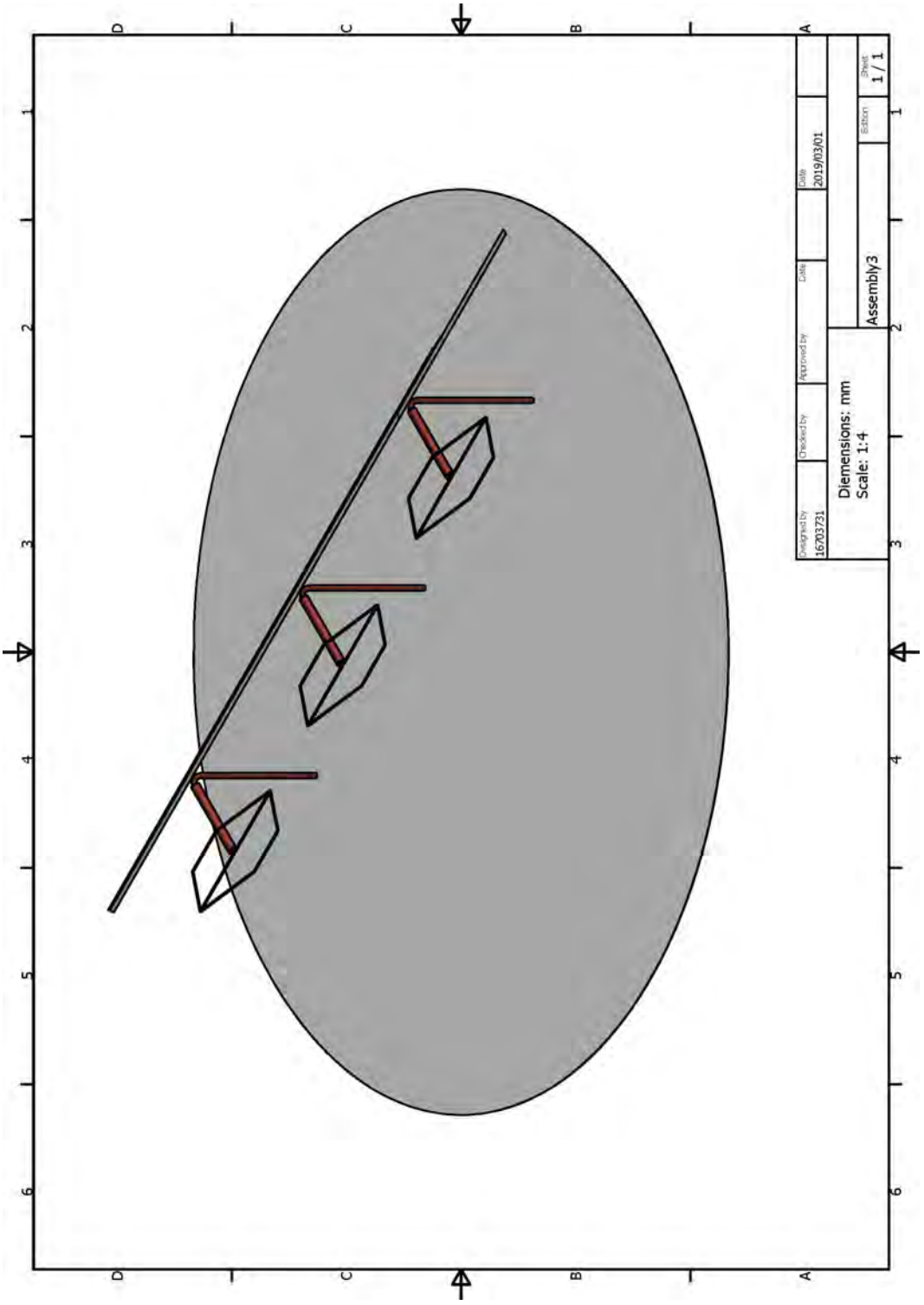

Figure A.2: 1:100 scale three element model assembly drawing. This engineering drawing shows the completed construction of the 1:100 scale three element model.

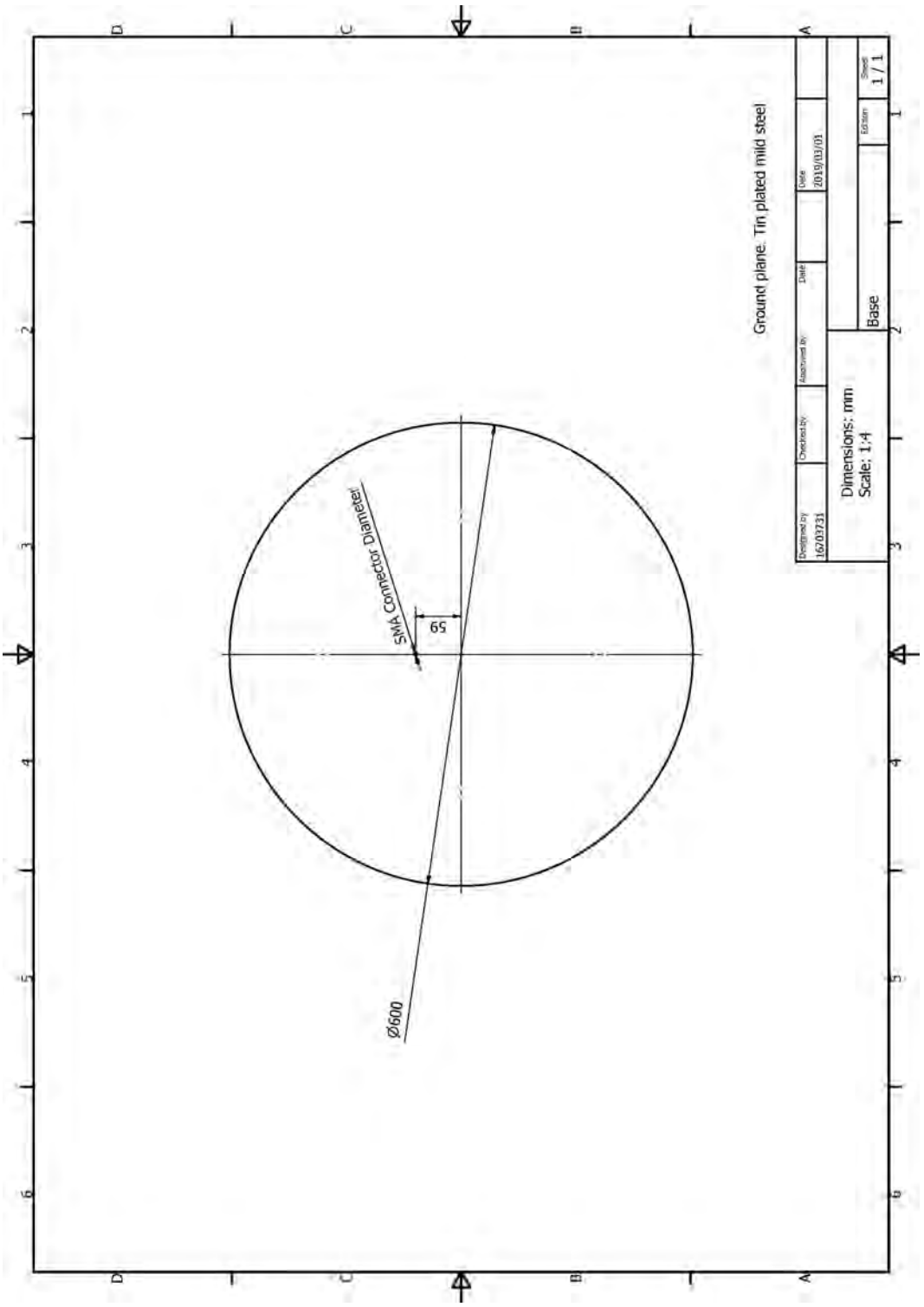

Figure A.3: 1:100 scale single element model tin plated mild steel base plate engineering drawing. This engineering drawing shows the base plate used for the 1:100 scale single element model.

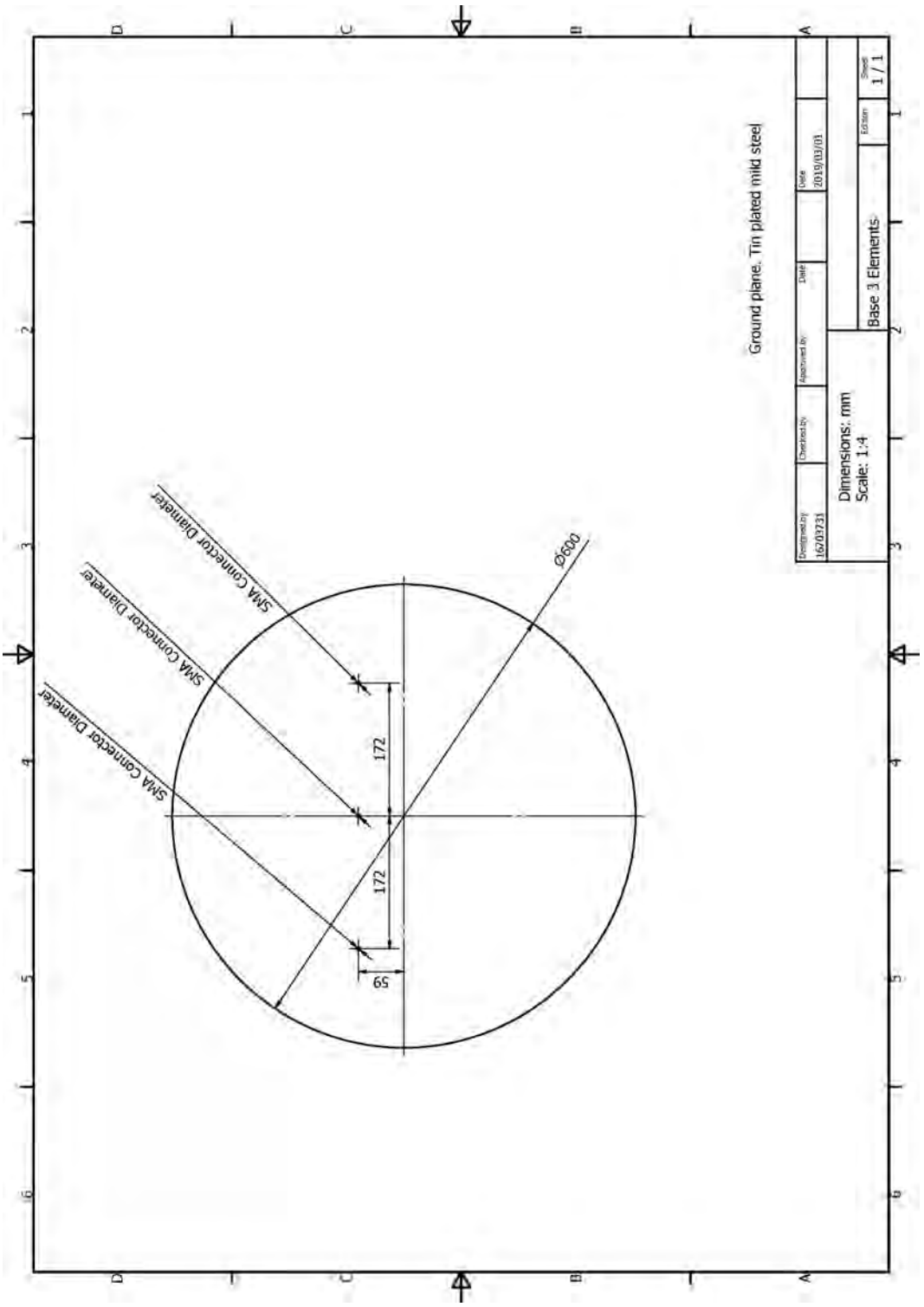

Figure A.4: 1:100 scale three element model tin plated mild steel base plate engineering drawing. This engineering drawing shows the base plate used for the 1:100 scale three element model.

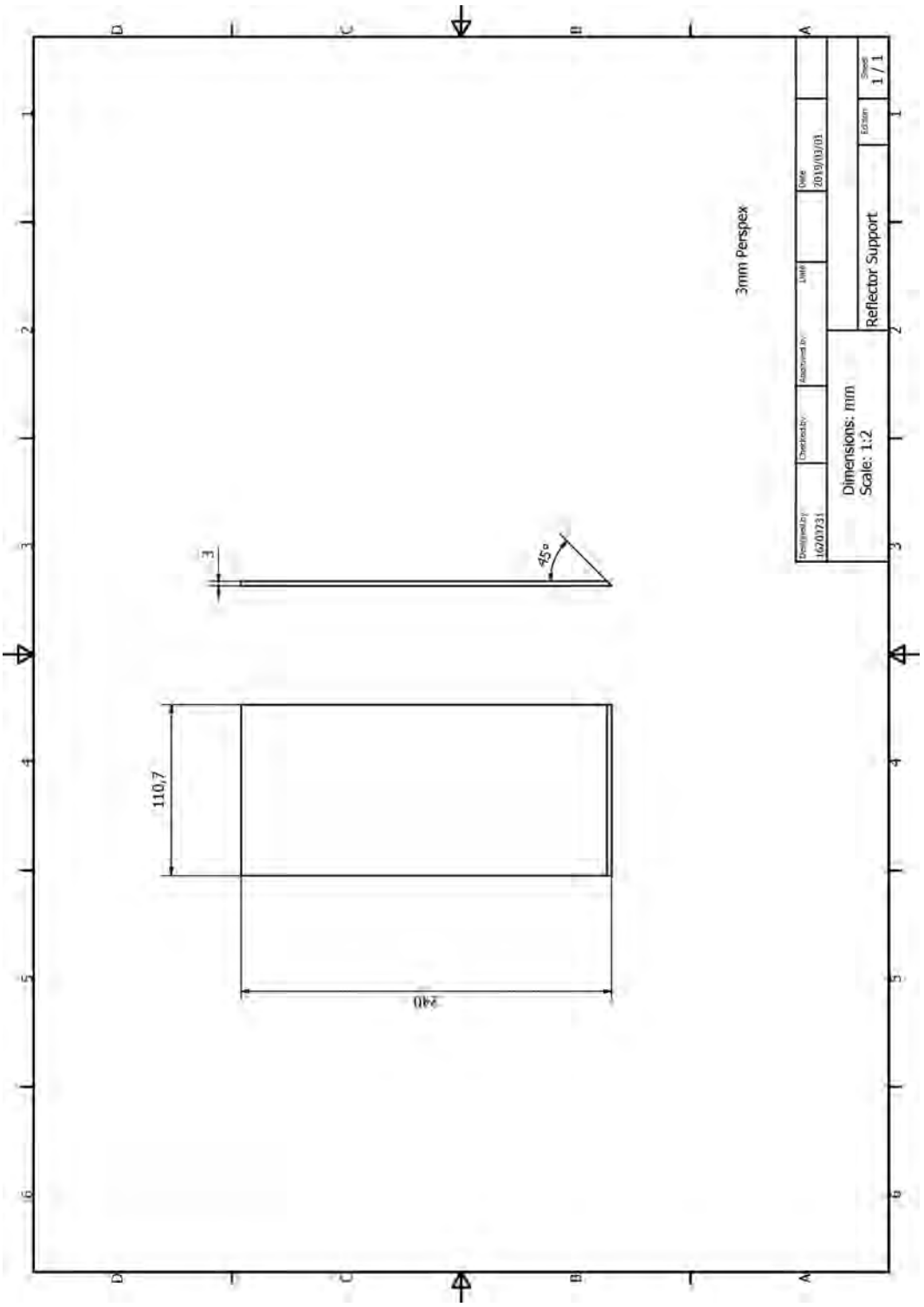

Figure A.5: 1:100 scale single element model perspex reflector support engineering drawing. This engineering drawing shows the 3 mm perspex reflector used to hold the reflector wires in place in the 1:100 scale single element model.

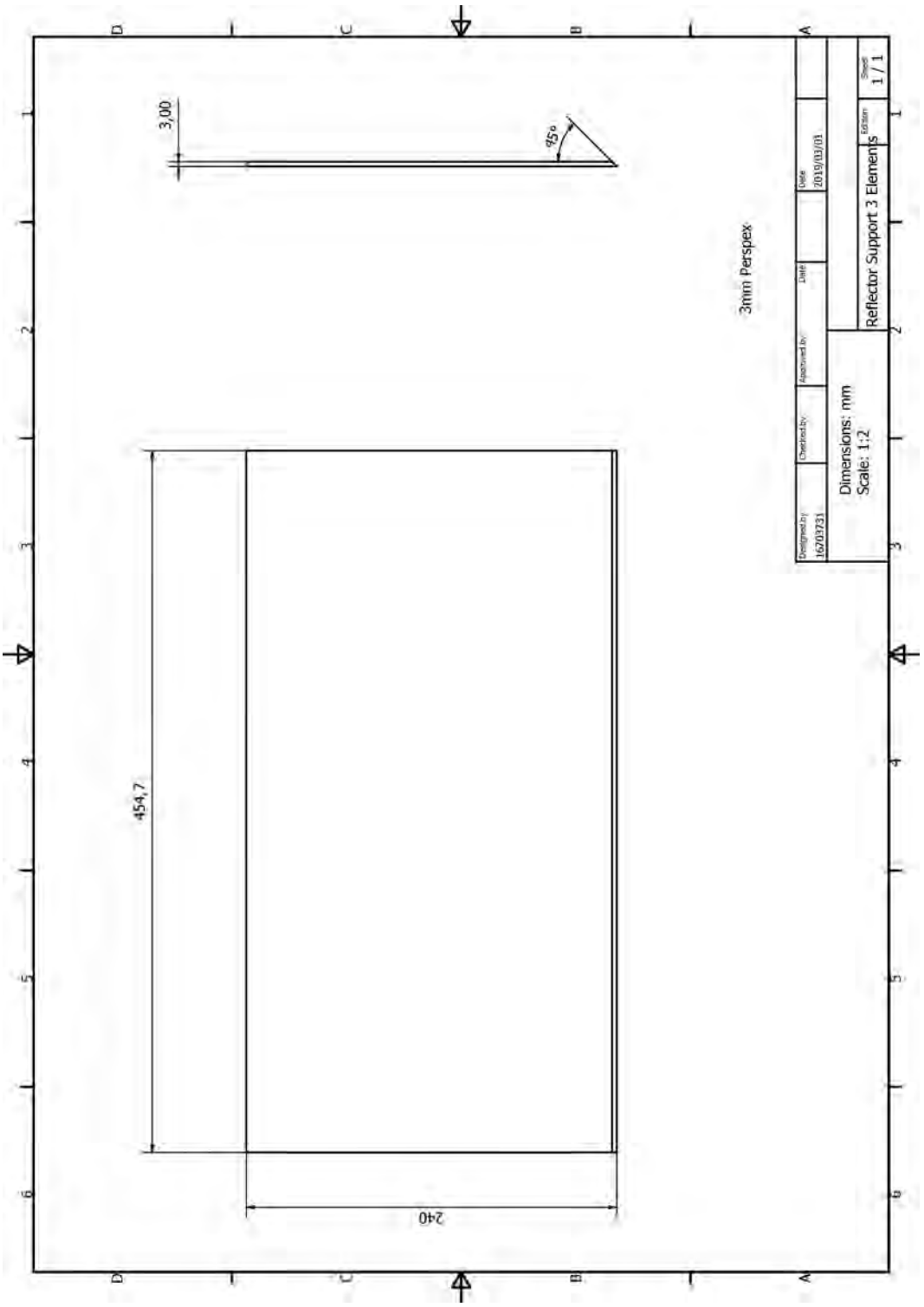

Figure A.6: 1:100 scale three element model perspex reflector support engineering drawing. This engineering drawing shows the 3 mm perspex reflector used to hold the reflector wires in place in the 1:100 scale three element model.

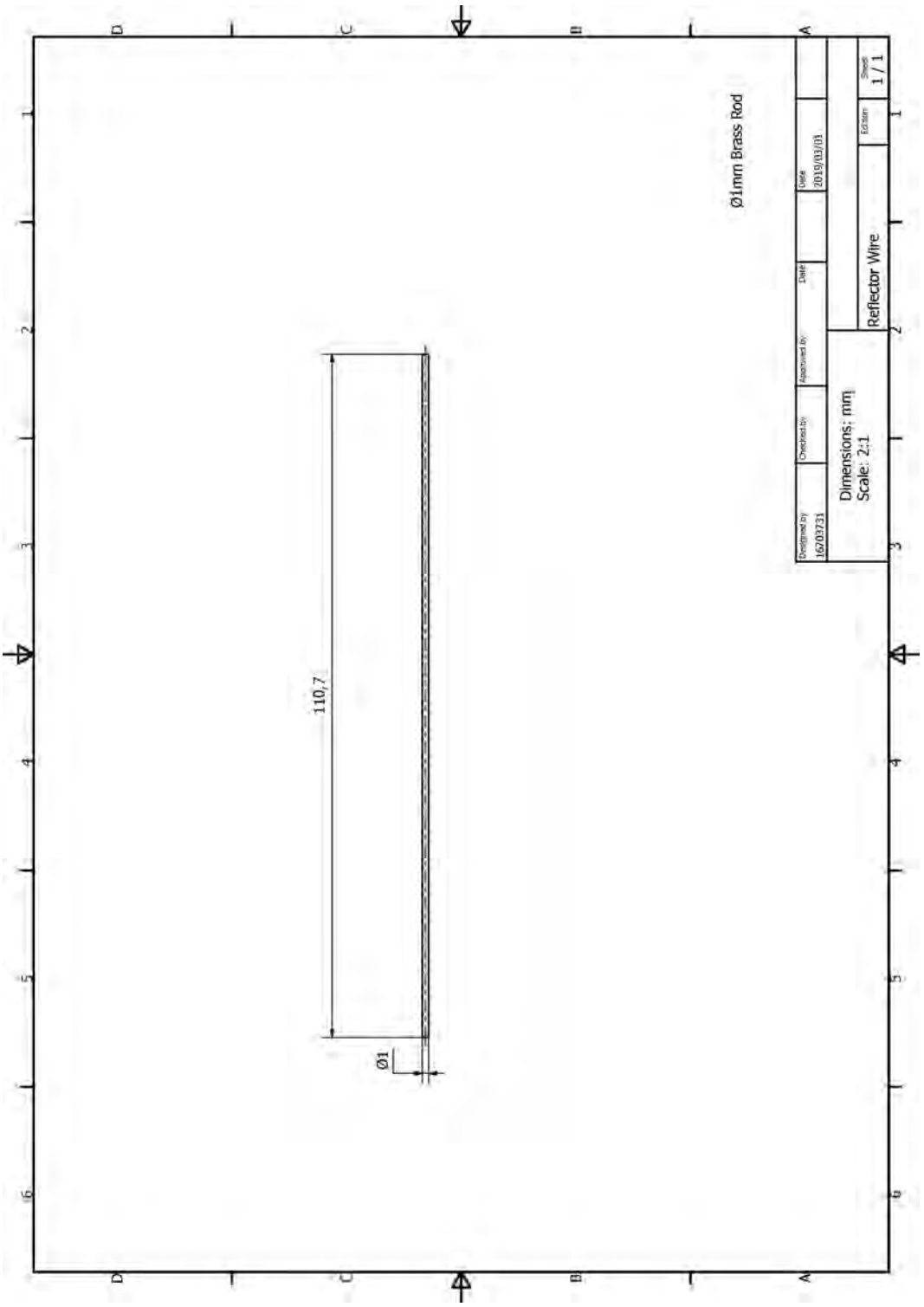

Figure A.7: 1:100 scale single element model brass reflector wire engineering drawing. This engineering drawing shows the ∅1 mm brass rods used for the half reflector in the 1:100 scale single element model.

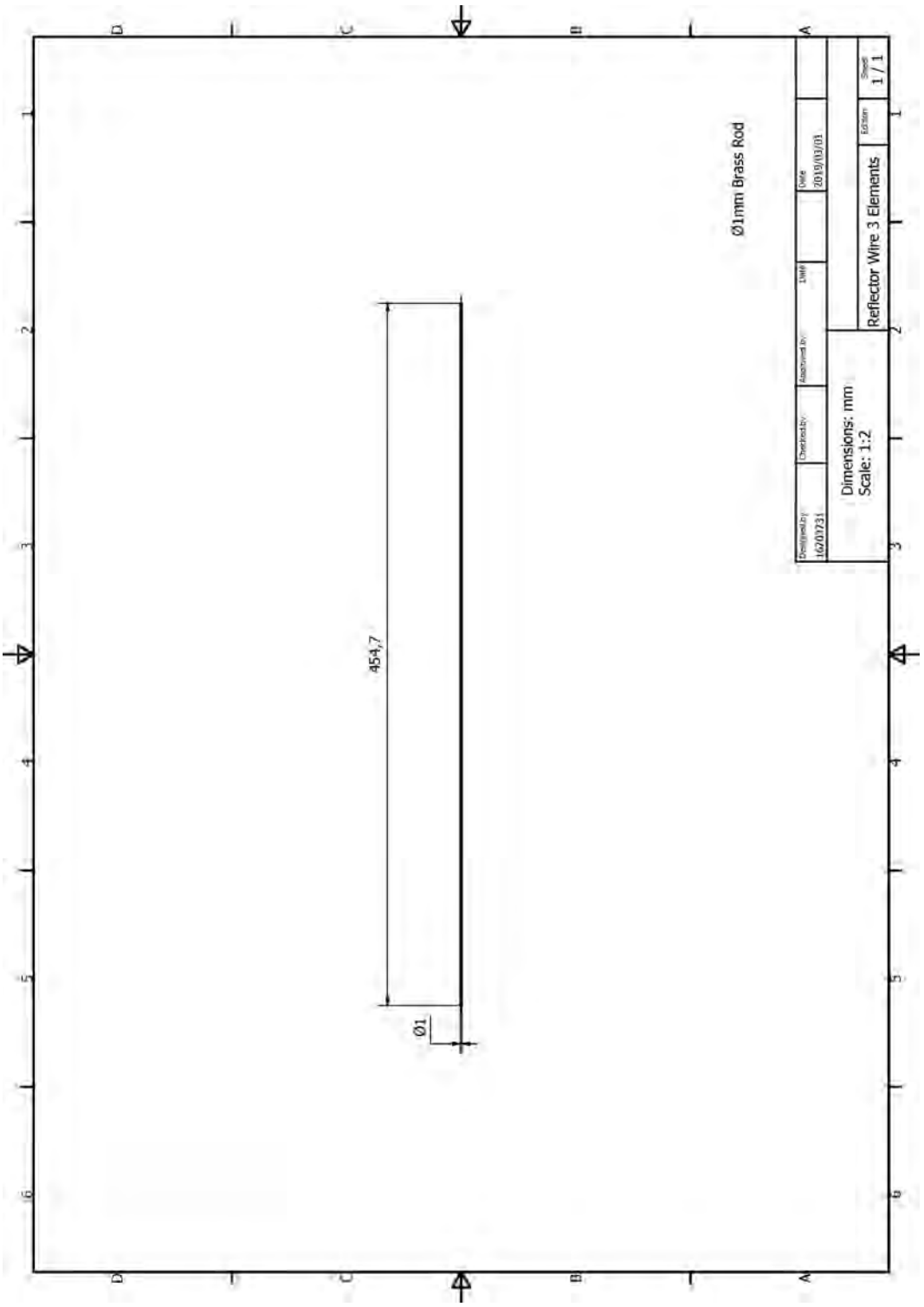

Figure A.8: 1:100 scale three element model brass reflector wire engineering drawing. This engineering drawing shows the ∅1 mm brass rods used for the half reflector in the 1:100 scale three element model.

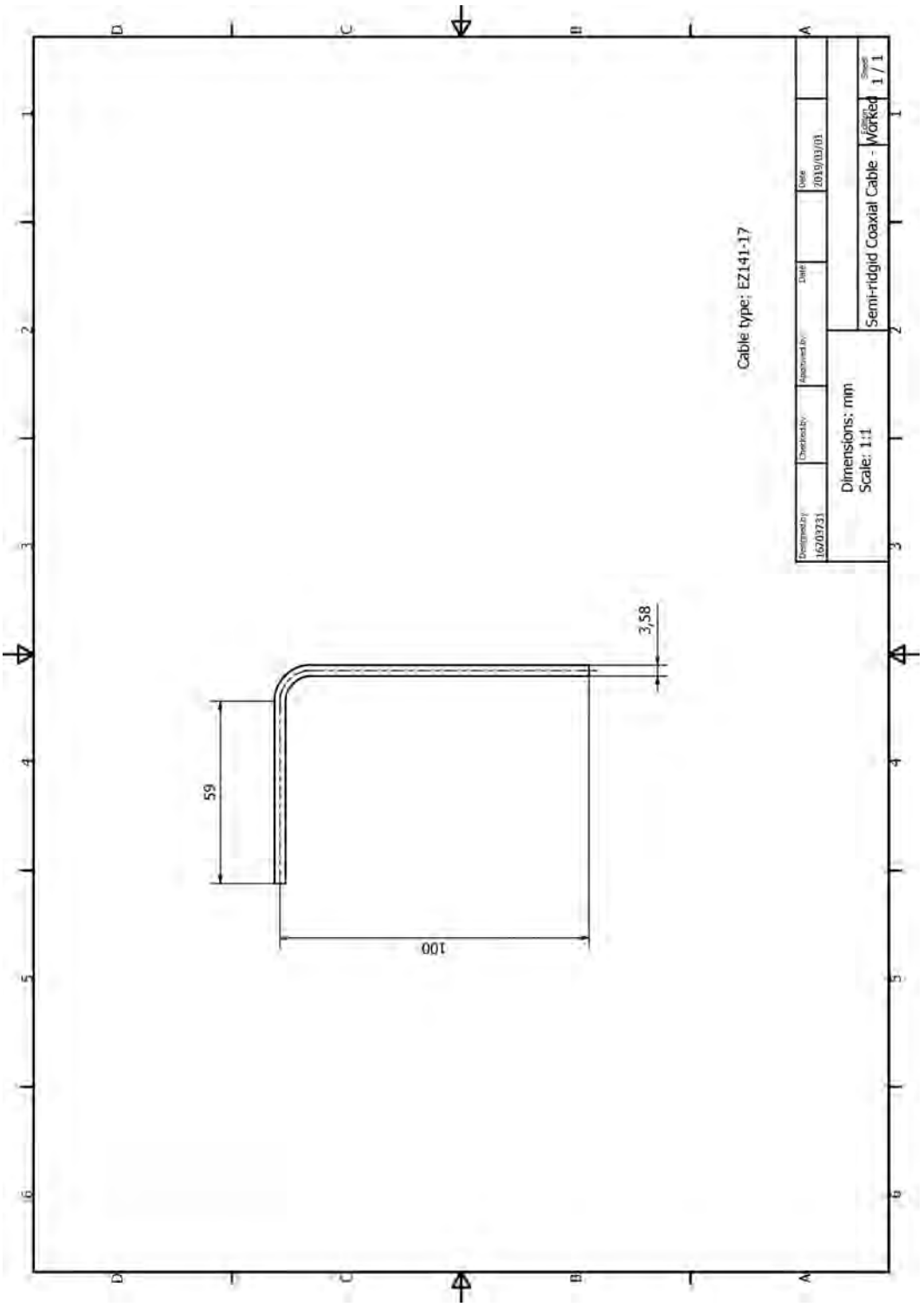

Figure A.9: 1:100 scale model semi-rigid coaxial cable engineering drawing. This engineering drawing shows the worked 50Ω semi-rigid coaxial cable which the sleeve balun is placed on and hold the antenna element in place, of both models.

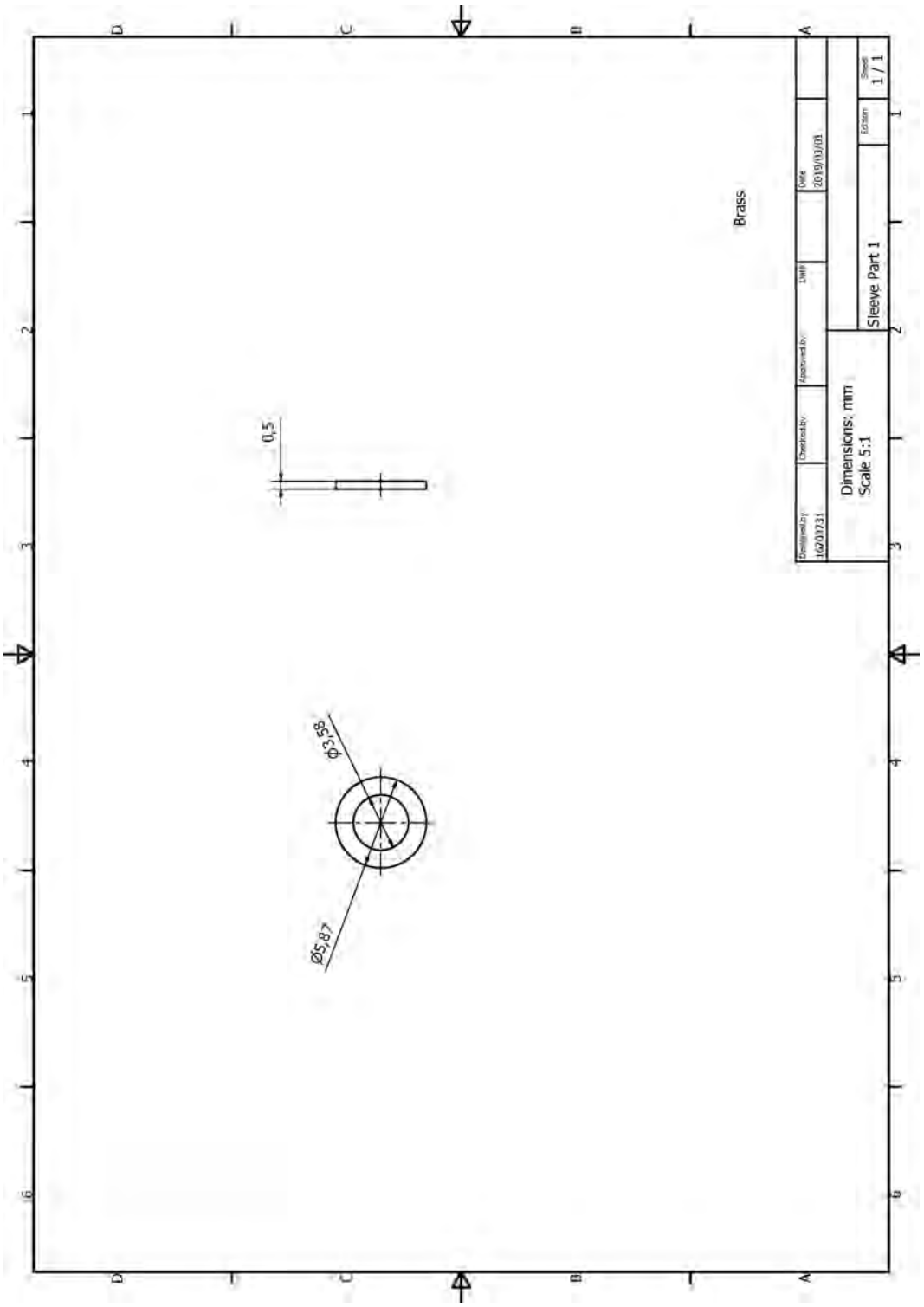

Figure A.10: 1:100 scale model sleeve balun part 1 engineering drawing. This engineering drawing shows the part of the sleeve balun which is connected to the furthest point from the radiation creating the short-circuit, of both models.

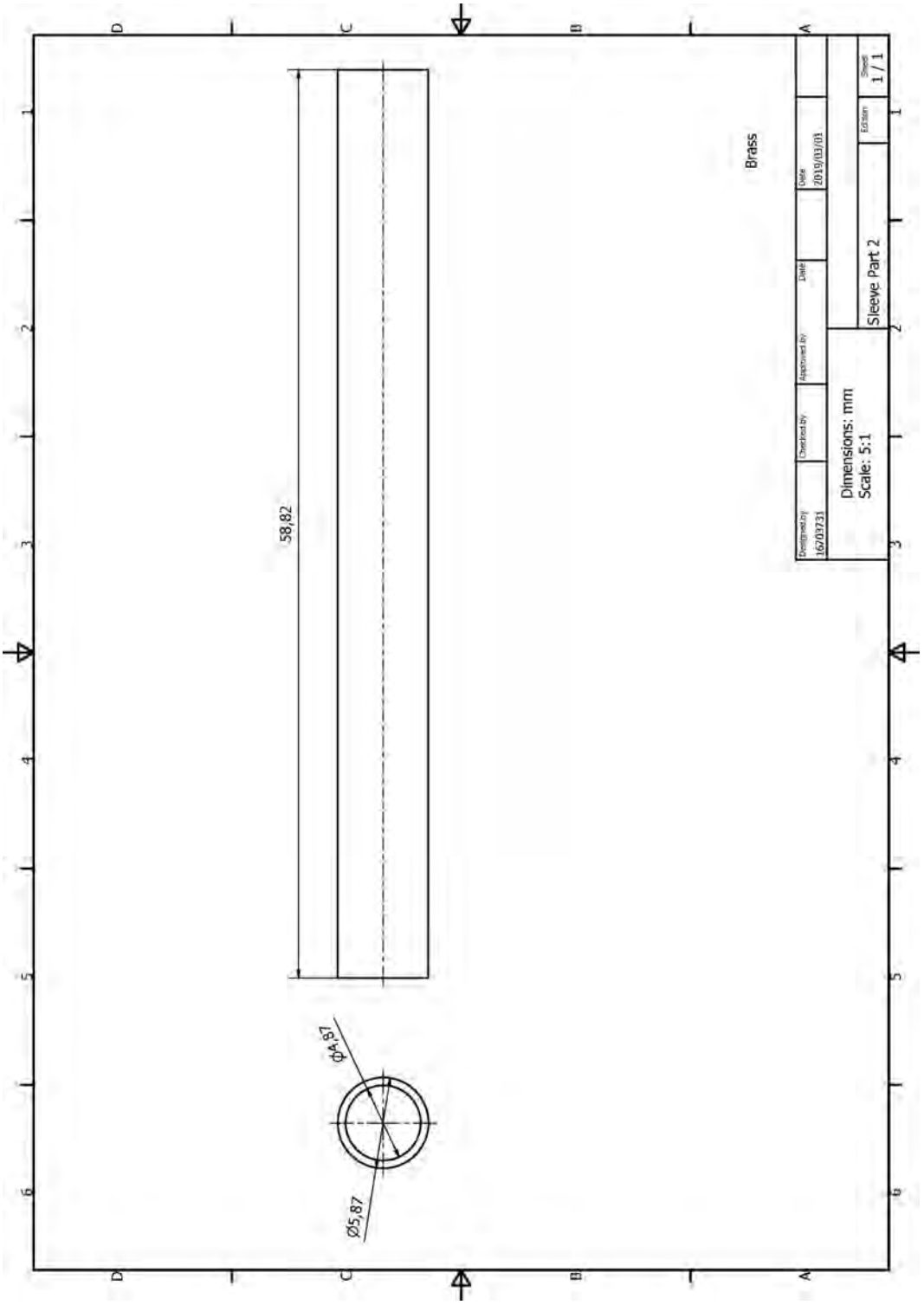

Figure A.11: 1:100 scale model sleeve balun part 2 engineering drawing. This engineering drawing shows the sleeve component of the sleeve balun, of both models.

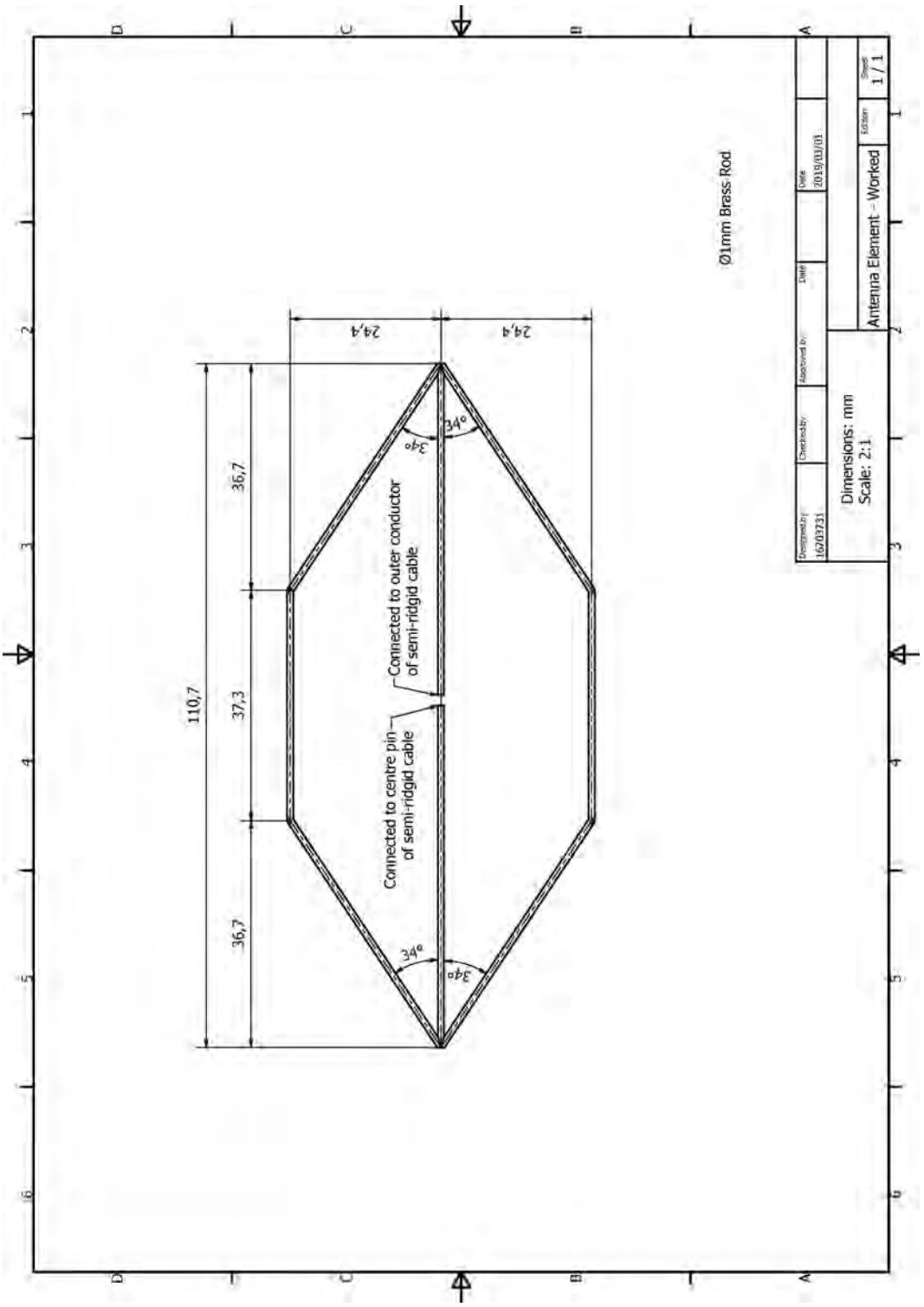

Figure A.12: 1:100 scale model antenna element engineering drawing. This engineering drawing shows the worked ∅1 mm brass rod used to create the antenna elements of both models.

Appendix B

Simulation Results Not Listed in Chapter 4.

The tables in this Appendix are a summary of the simulation results of various 90° half and full corner reflectors not listed in chapter 4. They contain the results of various 90° half and full ideal plate corner reflectors for comparison of the wire corner reflector used and simulated. The Appendix also includes 30° and 60° full wire corner reflectors which were used to confirm that the stated 90° was indeed the optimal corner angle to use in the various simulations run.

Table B.1: Simulation results of full-scale SuperDARN array with 90° half corner reflector not listed in chapter 4.

Model	Front Directivity and Angle	Back Directivity and Angle	Front to Back Ratio
·Plate corner reflector (half) ·Reflector 90° ·SuperDARN dimensions ·PEC ground	20.00009 dBi 60°	3.94 dBi 311.4°	16.06009 dBi
·Plate corner reflector (half) ·Reflector 90° ·PEC ground	19.7398 dBi 60°	8.71 dBi 310.2°	11.0298 dBi
·Plate corner reflector (half) ·Reflector 90° ·SuperDARN dimensions ·Ice and granite ground	18.3754 dBi 64°	7.21 dBi 312°	11.1654 dBi
·Plate corner reflector (half) ·Reflector 90° ·Ice and granite ground	18.0152 dBi 64°	9.63 dBi 310.1°	8.3852 dBi

Table B.2: Simulation results of full-scale SuperDARN array with 90° full corner reflector not listed in chapter 4.

Model	Front Directivity and Angle	Back Directivity and Angle	Front to Back Ratio
·Plate corner reflector (full) ·Reflector 90° ·PEC ground	20.4407 dBi 60°	-4.47 dBi 320.7°	24.9007 dBi
·Wire corner reflector (full) ·Reflector 60° ·Connected behind elements ·SuperDARN wire spacing ·PEC ground	19.8549 dBi 58°	6.12 dBi 308.3°	13.7349 dBi
·Wire corner reflector (full) ·Reflector 30° ·Connected behind elements ·SuperDARN wire spacing ·PEC ground	20.0462 dBi 60°	5.85 dBi 309.1°	14.1962 dBi
·Plate corner reflector (full) ·Reflector 90° ·Ice and granite ground	20.0274 dBi 66°	-3 dBi 318.1°	23.0274 dBi
·Wire corner reflector (full) ·Reflector 60° ·Connected behind elements ·SuperDARN wire spacing ·Ice and granite ground	19.3436 dBi 62°	7.61 dBi 304.3°	11.7336 dBi
·Wire corner reflector (full) ·Reflector 30° ·Connected behind elements ·SuperDARN wire spacing ·Ice and granite ground	19.5725 dBi 64°	6.37 dBi 305.9°	13.2025 dBi

Appendix C

Phase Matrix of SuperDARN Radar.

Ae pairs	1-2	2-3	3-4	4-5	5-6	6-7	7-8	8-9	9-10	10-11	11-12	12-13	13-14	14-15	15-16
Beam#															
0	75.4	70.1	72.4	75.1	74.5	72.6	73.2	73.4	74.8	75.0	73.4	69.7	73.9	74.0	70.0
1	63.9	61.6	60.4	66.7	63.4	60.7	64.7	62.5	64.9	64.0	63.6	60.9	65.6	62.7	61.9
2	51.0	55.1	51.0	54.4	53.7	57.0	52.9	55.3	50.2	54.1	54.6	53.6	51.4	54.3	54.2
3	39.4	46.3	43.7	40.9	43.7	46.5	43.5	43.9	42.4	40.4	46.2	44.0	41.2	45.4	45.4
4	33.8	31.6	33.5	34.7	32.8	34.0	33.7	37.8	31.7	36.4	30.1	31.5	31.1	34.3	33.2
5	22.8	23.1	22.7	23.3	23.5	24.0	23.9	25.9	23.5	22.5	22.7	21.3	22.6	25.2	23.1
6	13.8	11.8	12.7	14.6	13.6	14.6	13.3	16.9	13.5	12.5	13.5	11.0	12.9	15.4	13.2
7	4.1	2.2	3.4	3.9	1.7	4.5	3.5	5.5	3.5	2.2	2.7	2.0	4.2	4.7	3.1
8	-6.0	-7.8	-6.8	-5.1	-6.0	-5.1	-6.7	-6.7	-6.5	-7.4	-5.1	-7.2	-6.1	-5.3	-6.9
9	-16.1	-18.3	-15.8	-14.3	-15.9	-14.8	-17.1	-18.1	-16.9	-17.3	-16.6	-17.9	-15.8	-14.7	-16.9
10	-26.3	-28.6	-25.4	-25.3	-24.9	-25.7	-26.5	-27.3	-27.4	-27.3	-25.7	-27.2	-25.9	-26.7	-26.3
11	-36.2	-37.0	-34.4	-34.7	-33.2	-39.1	-35.1	-39.2	-37.4	-37.3	-35.4	-38.6	-36.8	-34.9	-37.0
12	-48.7	-48.1	-44.2	-48.2	-48.8	-43.1	-45.1	-45.4	-47.9	-48.4	-46.6	-43.7	-48.2	-49.9	-44.0
13	-57.8	-58.6	-55.6	-58.8	-58.1	-57.5	-54.2	-57.8	-58.2	-60.5	-57.4	-58.3	-56.3	-59.8	-56.5
14	-65.6	-66.9	-69.9	-65.8	-67.8	-67.0	-68.7	-65.3	-70.1	-63.2	-67.4	-71.1	-65.2	-66.4	-69.7
15	-74.0	-78.4	-78.0	-75.0	-78.3	-78.6	-78.9	-76.3	-78.2	-75.2	-78.8	-79.0	-78.5	-74.9	-81.1

Appendix D

Electrically Small Antenna Designs.

During the earlier stages of this project, it was discussed that a multi-copter could be used to do measurements to characterise the SuperDARN radar on-site at the SANAE IV base. Because of the regulatory licensing requirements to fly multi-copters, as well as cost and time constraints that compliance with the regulatory requirements would involve, it was decided to replace this concept with one involving modelling the radar in an EM solver such as FEKO. If the idea of using a multi-copter is investigated further, two ESA antenna designs which could be mounted onto the multi-copter can be found in Appendix D.

This section will aim to provide a basic understanding of their operations if they are ever used in future projects to characterise the SuperDARN radar on-site at SANAE IV. An ESA is used due to the SuperDARN radar's proximity to the approximate 100 m cliff drop to the ice shelf below.

An ESA is an antenna, with its largest dimensions being encompassed by a sphere with radius a, shown in figure D.1, so that [33];

$$ka \leq 0.5 \tag{D.1}$$

with the reactive near-field in terms of radian length as;

$$rl = \frac{\lambda}{2\pi} \tag{D.2}$$

rl = Radian length (m)

In figure D.1, the boundary limits are shown as a graphical representation. The largest ESA dimension a can be seen compassing the ESA by a sphere with radius its equal to a. The non-radiating energy near-field region boundary limit of the ESA can be seen as the distance equal to the radian length.

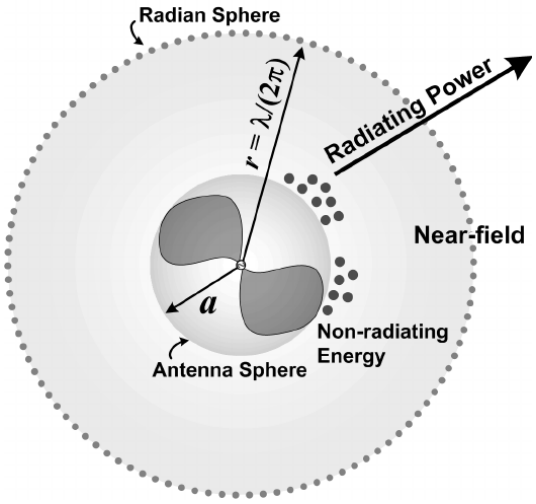

Figure D.1: Field regions of an ESA [34]. This figure shows the various field regions defined by equations D.1 and D.2.

The first design found in D.0.1 uses principles from [35] which state an ESA can be improved through inductive and dielectric loading. Put simply this means that if the dielectric constant of the material onto which the conducting part of an ESA is placed is increased, along with ensuring the physical dimensions increase in such a way that the inductance increases proportionally to the increase in dimension, the size of the ESA can be reduced.

The second design in D.0.2 uses principles from [36] which employs the use of a shallow cavity to back a well-know meandering archimedean spiral antenna design, [37] which further improves on the this antenna design by reducing the area of the antenna by adding dielectric absorber material to the cavity. This dielectric absorber makes the antenna more directional by reducing the side and back radiation levels but reduces efficiency. Finally, the parallel curves theorem was used to ensure the correct transmission (TM) line width throughout the antenna's design [38].

Below are the design for two ESA that could be used or modified to characterise the SuperDARN on-site at the SANAE IV base. The designs were done in DDS Simula CST Studio Suite as they were designed during the earlier stages of this project.

D.0.1 Stacked Double Coil ESA Design

This design makes use of CST's Planar Circular Spiral - rectangular cross section macro with the values in table D.1.

Table D.1: Variables used to design the stacked double coil ESA in CST.

Variable	Value
Height of brass	0.5 mm
Coil inner radius	15 mm
Coil width	3 mm
Number of coil turns	12
Coil gap	10 mm
Height of second coil from first	23 mm
Dielectric height	10 mm
Dielectric outer radius	176 mm
Dielectric ϵ	10 F/m

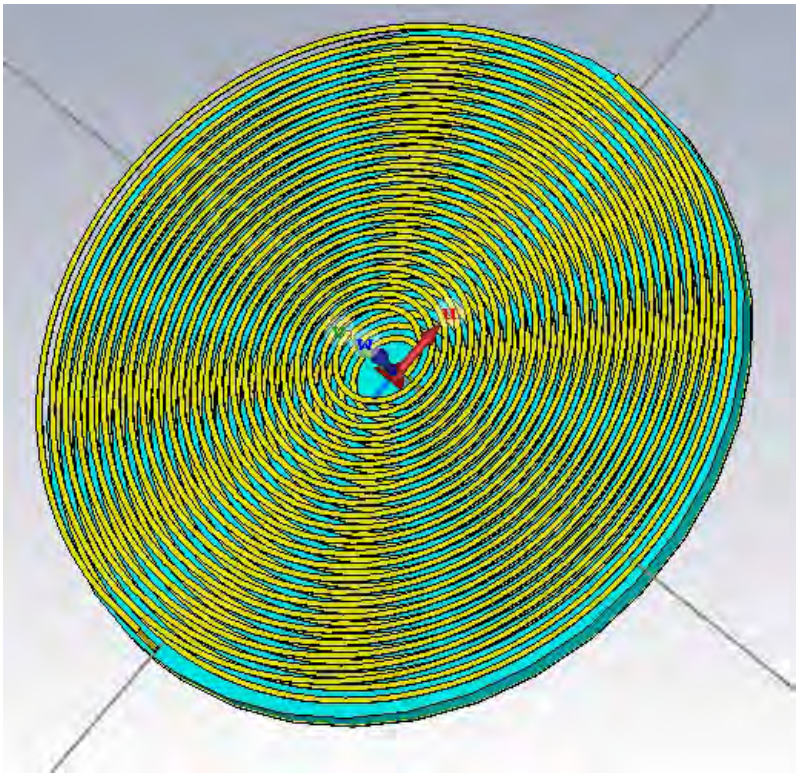

Figure D.2: ESA design using two brass coils stacked on top of each other, isometric view 1. This ESA is a stacked double coil design stacking two coils on top of each other, placed onto a dielectric material with an epsilon of 10, feed by a 50Ω SMA connector.

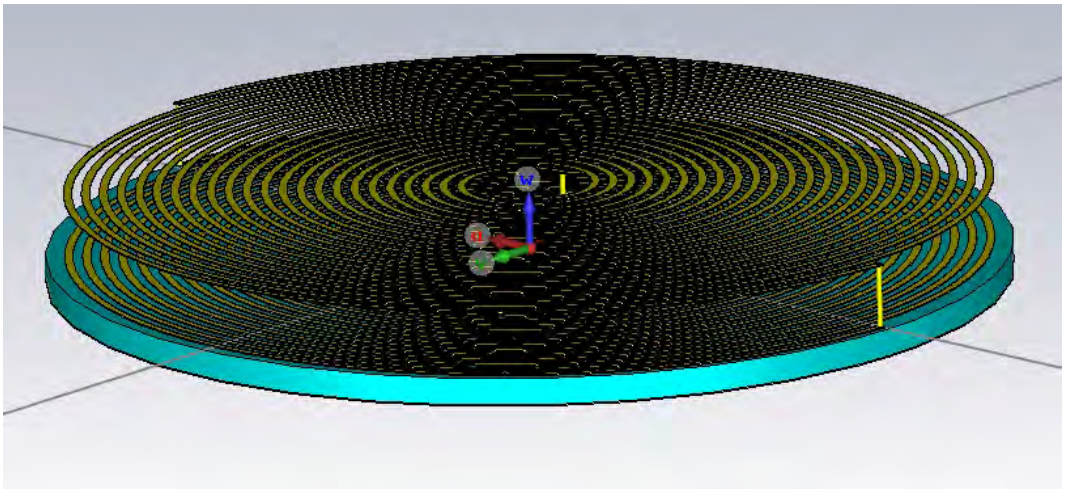

Figure D.3: ESA design using two brass coils stacked on top of each other, isometric view 2. This ESA is a stacked double coil design stacking two coils on top of each other, placed onto a dielectric material with an epsilon of 10, feed by a 50Ω SMA connector.

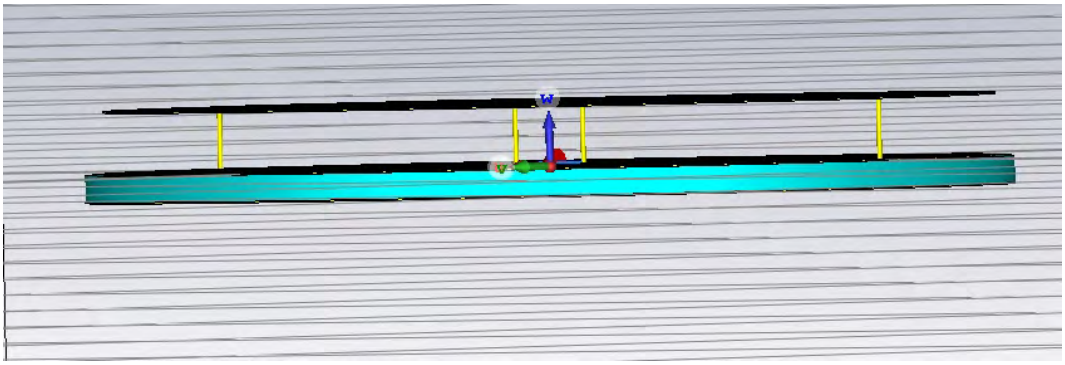

Figure D.4: ESA design using two brass coils stacked on top of each other, side view. This ESA is a stacked double coil design stacking two coils on top of each other, placed onto a dielectric material with an epsilon of 10, feed by a 50Ω SMA connector.

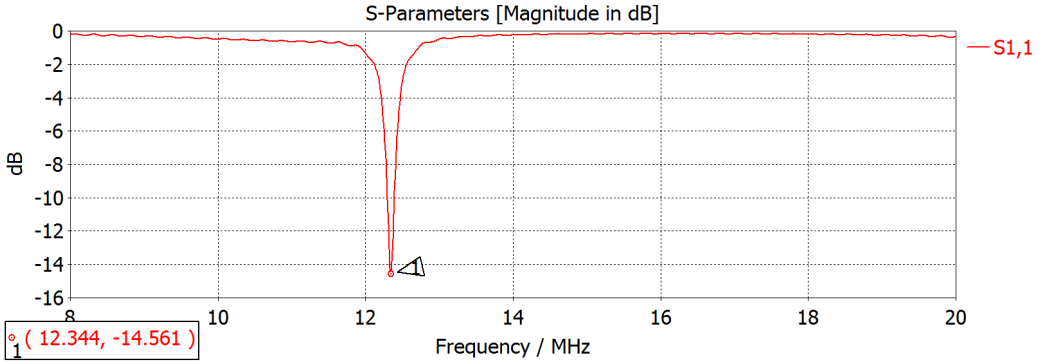

Figure D.5: S_{11} results of the stacked double coil ESA design. The results above show that the ESA has a resonant frequency of 12.344 MHz, with some adjustments it can be improved to 12.75 MHz.

D.0.2 Meandering Archimedean Spiral Backed by a Shallow Cavity ESA Design

This design makes use of CST's spline curve macro with the values in table D.2. The equation for the inner exponential spiral is as follows:

Table D.2: Variables used to design meandering archimedean spiral backed by a shallow cavity in CST.

Variable Name	Variable	Value
Initial radius	r_0	$25\ mm$
Spiral constant	α_1	$0.4\ mm/rad$
Starting angle of exponential spiral	$\varphi\varphi$	$1.5\pi\ rad$
Ending angle of exponential spiral	φ_{start}	$4\pi\ rad$
Ending angle of meandering spiral	φ_{end}	$21\pi\ rad$
Ending angle of exponential spiral tip	φ_{final}	$21.5\pi\ rad$
Meandering spiral constant	α_2	$25\pi\ mm/rad$
TM line width (half)	w	$0.5\ mm$

$$r(i) = r_0 e^{\alpha_1 \varphi(i)}$$

with its derivatives

$$\begin{aligned} x'(i) &= r_0 e^{\alpha_1 \varphi(i)} (\alpha_1 cos\varphi(i) - sin\varphi(i)) \\ y'(i) &= r_0 e^{\alpha_1 \varphi(i)} (\alpha_1 sin\varphi(i) + cos\varphi(i)) \end{aligned} \tag{D.3}$$

The equation for the middle meandering sinusoidal spiral is as follows:

$$\begin{aligned} r(\varphi) =& \alpha_2(\varphi - \varphi_1) + r_0 e^{\alpha_1 \varphi_{start}} + m(1 + sin(n\varphi)) \end{aligned}$$

with its derivatives

$$\begin{aligned} x'(i) =& cos(\varphi(i))(\alpha_2 + mncos(n\varphi(i))) - sin(\varphi(i)) \\ & (\alpha_2\varphi(i) - \alpha_2\varphi_{start} + msin(n\varphi(i))) + m + r_0 e^{\alpha_1\varphi_{start}} \\ y'(i) =& cos(\varphi(i))(5\varphi(i) - \alpha_2\varphi_{start} + msin(n\varphi(i)) + m + r_0 e^{\alpha_1\varphi_{start}}) \\ & + sin(\varphi(i))(\alpha_2 + mncos(n\varphi_i)) \end{aligned} \tag{D.4}$$

The equation for the outer tapered TM line is as follows:

$$\begin{aligned} r(\varphi) =& \alpha_2(\varphi - 6\varphi_{final}) + r_0 e^{\alpha_1\varphi_{start}} \end{aligned}$$

with its derivatives

$$\begin{aligned} x'(i) =& \alpha_2 cos(\varphi(i)) - sin(\varphi(i)) \\ & (r_0 e^{\alpha_1\varphi_{start}} + \alpha_2(\varphi(i) - 6\varphi_{final})) \\ y'(i) =& \alpha_2 cos(\varphi(i)) + cos(\varphi(i)) \\ & (r_0 e^{\alpha_1\varphi_{start}} + \alpha_2(\varphi(i) - 6\varphi_{final})) \end{aligned} \tag{D.5}$$

With the equations of the parallel curves theorem as follows:

$$x_1(i) = r(i)cos(\varphi(i)) \tag{D.6a}$$
$$y_1(i) = r(i)sin(\varphi(i)) \tag{D.6b}$$
$$x_2(i) = -r(i)cos(\varphi(i)) \tag{D.6c}$$
$$y_2(i) = -r(i)sin(\varphi(i)) \tag{D.6d}$$
and (D.6e)
$$x_{11}(i) = x_1(i) + w\frac{y'(i)}{\sqrt{x'^2(i) + y'^2(i)}} \tag{D.6f}$$
$$y_{11}(i) = y_1(i) - w\frac{x'(i)}{\sqrt{x'^2(i) + y'^2(i)}} \tag{D.6g}$$
$$x_{12}(i) = x_1(i) - w\frac{y'(i)}{\sqrt{x'^2(i) + y'^2(i)}} \tag{D.6h}$$
$$y_{12}(i) = y_1(i) + w\frac{x'(i)}{\sqrt{x'^2(i) + y'^2(i)}} \tag{D.6i}$$
(D.6j)

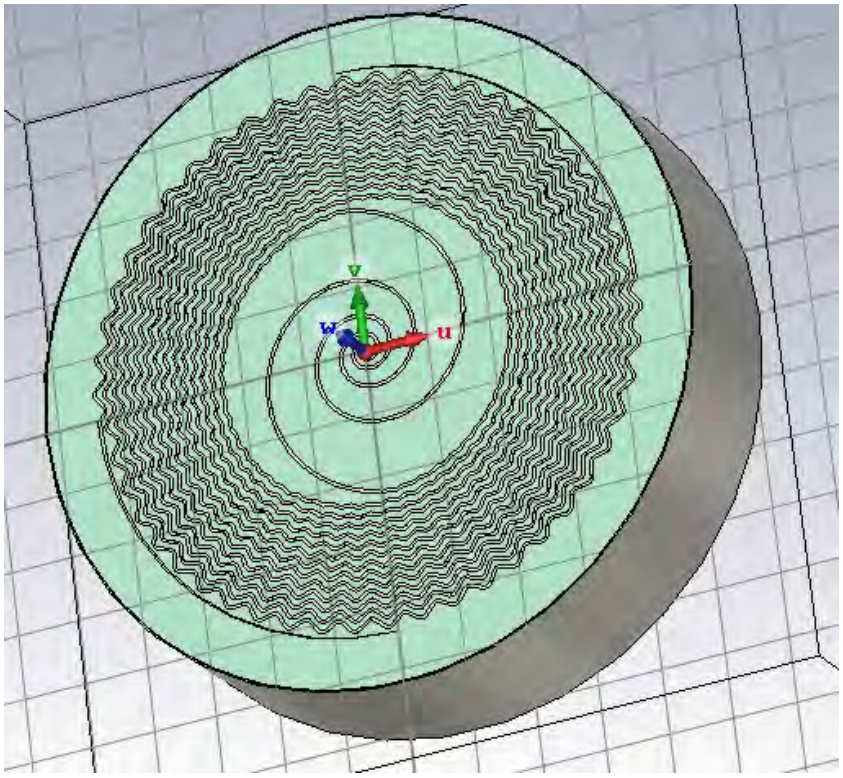

Figure D.6: ESA design of a meandering archimedean spiral backed by a shallow cavity. The design above makes use of CST's spline curve with a meandering archimedean spiral equation.

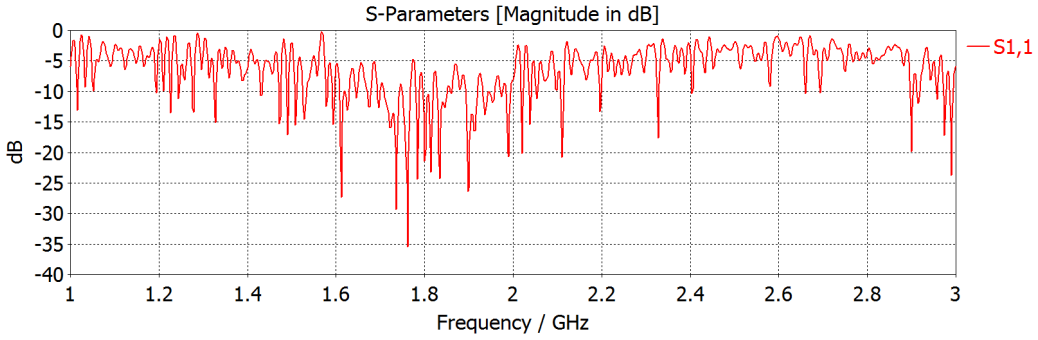

Figure D.7: S_{11} results of a meandering archimedean spiral backed by a shallow cavity. The results above show that the meandering archimedean spiral backed by a shallow cavity operates best above 1 GHz, with some modifications the design can be made to operate between 8 - 20 MHz.

References

[1] N. Nishitani, J. M. Ruohoniemi, M. Lester, J. B. H. Baker, A. V. Koustov, S. G. Shepherd, G. Chisham, T. Hori, E. G. Thomas, R. A. Makarevich, A. Marchaudon, P. Ponomarenko, J. A. Wild, S. E. Milan, W. A. Bristow, J. Devlin, E. Miller, R. A. Greenwald, T. Ogawa, and T. Kikuchi, "Review of the accomplishments of mid-latitude Super Dual Auroral Radar Network (SuperDARN) HF radars," *Progress in Earth and Planetary Science*, 2019.

[2] L. Mark, "The Super Dual Auroral Radar Network (SuperDARN): An overview of its development and science," *ADVANCES IN POLAR SCIENCE*, vol. 24, no. 1, pp. 1–11, jan 2014.

[3] S. E. Milan, T. B. Jones, T. R. Robinson, E. C. Thomas, and T. K. Yeoman, "Interferometric evidence for the observation of ground backscatter originating behind the CUTLASS coherent HF radars," *Annales Geophysicae*, vol. 15, no. 1, pp. 29–39, 1997.

[4] C. A. Balanis, *Antenna Theory : Analysis and Design*. Wiley Interscience, 2005.

[5] S. E. Milan, T. B. Jones, T. R. Robinson, E. C. Thomas, and T. K. Yeoman, "Interferometric evidence for the observation of ground backscatter originating behind the CUTLASS coherent HF radars," *Annales Geophysicae*, vol. 15, no. 1, pp. 29–39, 1997.

[6] T. Takano, K. Saegusa, and H. Hosono, "A large-scale phased array antenna: Its applications and key technologies," in *2013 International Conference on Microwave and Photonics, ICMAP 2013*, 2013, p. 6.

[7] I. Gupta and A. Ksienski, "Effect of mutual coupling on the performance of adaptive arrays," *IEEE Transactions on Antennas and Propagation*, vol. 31, no. 5, pp. 785–791, sep 1983. [Online]. Available: http://ieeexplore.ieee.org/document/1143128/

[8] H. Singh, H. L. Sneha, and R. M. Jha, "Mutual coupling in phased arrays: A review," 2013.

[9] M. Wang, W. Wu, and Z. Shen, "Bandwidth Enhancement of Antenna Arrays Utilizing Mutual Coupling between Antenna Elements," *International Journal of Antennas and Propagation*, vol. 2010, p. 9, 2010.

[10] R. C. Hanson, *Phased Array Antennas*, 2nd ed., K. Chang, Ed. John Wiley & Sons, INC., 2009.

[11] R. A. Greenwald, "Steering SuperDARN Radars," Virginia Tech, Tech. Rep.

[12] "VT SuperDARN Home : Virginia Tech SuperDARN," 2019. [Online]. Available: http://vt.superdarn.org/tiki-index.php

[13] A. B. Ford and D. L. Schmidt, "The Antarctic and Its Geology," United States Department of the Interior/Geological Survey, Tech. Rep., 1978.

[14] J. S. Ward, "Engineering for Space Science in Remote Area," in *SANAP Symposium*, 2018, p. 36.

[15] "https://www.bbc.com/news/magazine-38574003," 2017.

[16] G. Bryson, W. Bristow, and T. Parris, "An Introduction to Radar and the Super Dual Auroral Radar Network* (with an emphasis on the Kodiak SuperDARN)," University of Alaska Fairbanks, Tech. Rep., 2008.

[17] A. S. Reimer, "Improved SuperDARN Radar Signal Processing: A First Principles Statistical Approach for Reliable Measurement Uncertainties and Enhanced Data Products," Department of Physics and Engineering Physics University of Saskatchewan, Tech. Rep., 2018.

[18] "SANSDR1 Phasing Matrix - ProjectsWiki.html," 2010.

[19] E. Custovic, H. Q. Nguyen, J. C. Devlin, J. Whittington, D. Elton, A. Console, H. Ye, R. A. Greenwald, D. A. Andre, and M. J. Parsons, "Evolution of the SuperDARN antenna: Twin Terminated Folded Dipole antenna for HF systems," in *IB2COM 2011 - 6th International Conference on Broadband Communications and Biomedical Applications, Program*, 2011, pp. 24–29.

[20] K. T. Sterne, J. M. Ruohoniemi, C.-C. Joseph, B. H. Baker, C.-C. Steven, W. Ellingson, and W. A. Davis, "Testing the Re-designed SuperDARN HF Radar and Modeling of a Twin Terminated Folded Dipole Array," Virgina Tech, Tech. Rep., 2010.

[21] A. Piantini, J. M. Janiszewski, A. Borghetti, C. A. Nucci, and M. Paolone, "A Scale Model for the Study of the LEMP Response of Complex Power Distribution Networks," *IEEE Transactions on Power Delivery*, vol. 22, no. 1, pp. 710–720, jan 2007.

[22] G. Sinclair and G. Sinclair, "Theory of Models of Electromagnetic Systems," *Proceedings of the IRE*, vol. 36, no. 11, pp. 1364–1370, 1948.

[23] K. T. Sterne, R. A. Greenwald, J. B. Baker, and J. M. Ruohoniemi, "Modeling of a twin terminated folded dipole antenna for the Super Dual Auroral Radar Network (SuperDARN)," in *IEEE National Radar Conference - Proceedings*, 2011, pp. 934–938.

[24] S. Saario, J. Lu, and D. Thiel, "Full-wave analysis of choking characteristics of sleeve balun on coaxial cables," *Electronics Letters*, 2002.

[25] T. J. Phiri, "Characterising the Electromagnetic Environment of MeerKAT," Stellenbosch University Electrical and Electronic Engineering Department, Tech. Rep., 2017. [Online]. Available: https://scholar.sun.ac.za

[26] A. Hyperworks, "Altair Feko 2018.2 User Manual," p. 4604, 2018.

[27] R. F. Barrington, *Field computation by moment methods.* Wiley-IEEE Press, jan 1993.

[28] C. Phillips, D. Sicker, and D. Grunwald, "Bounding the practical error of path loss models," *International Journal of Antennas and Propagation*, vol. 2012, 2012.

[29] S. C. K. Dodson, "Design and Adaptation of a Folded Split Ring Resonator Antenna for an Animal Borne Sensor," Ph.D. dissertation, Stellenbosch University, 2017.

[30] D. M. P. Smith, D. B. Davidson, A. Bester, and J. Andriambeloson, "Modernising, Upgrading and Recommissioning the Indoor Antenna Range at Stellenbosch University," *SAIEE Africa Research Journal*, vol. 107, no. 1, pp. 4–16, mar 2016. [Online]. Available: https://ieeexplore.ieee.org/document/8532247/

[31] ITU, "ITU," 2019. [Online]. Available: https://www.itu.int/pub/R-REC

[32] CHPC, "https://www.chpc.ac.za/," 2019.

[33] G. Breed, "Basic Principles of Electrically Small Antennas," *High Frequency Electronics*, 2007.

[34] W. Davis, T. Yang, E. Caswell, and W. Stutzman, "Fundamental Limits on Antenna Size: A New Limit," *IET Microwaves Antennas & Propagation*, vol. 5, no. 11, pp. 1297 – 1302, 2011.

[35] B. A. Kramer, "Size Reduction of an UWB Low-Profile Spiral Antenna," Ph.D. dissertation, Ohio State University, 2007.

[36] H. Nakano, T. Igarashi, H. Oyanagi, Y. Iitsuka, and J. Yamauchi, "Unbalanced-mode spiral antenna backed by an extremely shallow cavity," *IEEE Transactions on Antennas and Propagation*, vol. 57, no. 6, pp. 1625–1633, 2009.

[37] Y. W. Wang, G. M. Wang, and H. Y. Zeng, "Design of a new meander Archimedean spiral antenna," *Microwave and Optical Technology Letters*, vol. 52, no. 10, pp. 2384–2387, oct 2010.

[38] H. Bukas, "The Theory of a Scroll Profile," in *International Compressor Engineering Conference*, 2006.